

**PONTIFICIA UNIVERSIDAD
CATÓLICA DEL PERÚ**

Escuela de Posgrado



Analysis of the physical properties and photoelectrochemical
behavior of c-Si/a-SiC:H(p) photocathodes for solar
water splitting

Tesis para obtener el grado académico de Doctora en Física que
presenta:

María del Carmen Mejía Chueca

Asesor:

Francisco Aurelio Rumiche Zapata

Co-asesores:

Jorge Andrés Guerra Torres

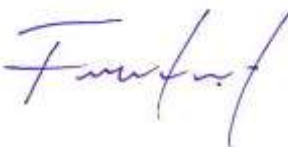
Lima, 2022

Declaración jurada de autenticidad

Yo, Francisco Aurelio Rumiche Zapata, docente de la Escuela de Posgrado de la Pontificia Universidad Católica del Perú, asesor de la tesis titulada *Analysis of the physical properties and photoelectrochemical behavior of c-Si/a-SiC:H(p) photocathodes for solar water splitting*, de la autora Maria del Carmen Mejía Chueca, dejo constancia de lo siguiente:

- El mencionado documento tiene un índice de puntuación de similitud de 48% (un 28% es de propios trabajos de la alumna) por lo que se reduciría a 20%, lo que está dentro del límite establecido. Así lo consigna el reporte de similitud emitido por el software *Turnitin* el 31/10/2022.
- He revisado con detalle dicho reporte y confirmo que cada una de las coincidencias detectadas no constituyen plagio alguno.
- Las citas a otros autores y sus respectivas referencias cumplen con las pautas académicas.

Lima, 11 de diciembre de 2022

| | |
|---|--|
| Apellidos y nombres del asesor: <u>Rumiche Zapata, Francisco Aurelio</u> | |
| DNI: 10491814 |  |
| ORCID: https://orcid.org/0000-0001-9318-8425 | |
| Firma: | |

Declaration of Authorship

I, María del Carmen MEJIA CHUECA, declare that this thesis titled, “Analysis of the physical properties and photoelectrochemical behavior of c-Si/a-SiC:H(p) photocathodes for solar water splitting” and the work presented in it are my own. I confirm that:

- This work was done wholly or mainly while in candidature for a research degree at this University.
- Where any part of this thesis has previously been submitted for a degree or any other qualification at this University or any other institution, this has been clearly stated.
- Where I have consulted the published work of others, this is always clearly attributed.
- Where I have quoted from the work of others, the source is always given. With the exception of such quotations, this thesis is entirely my own work.
- I have acknowledged all main sources of help.
- Where the thesis is based on work done by myself jointly with others, I have made clear exactly what was done by others and what I have contributed myself.

Signed:

Date:

“Let me stress this point: it is in the simplicity of your ordinary work, in the monotonous details of each day, that you have to find the secret, which is hidden from many, of something great and new: Love.”

Josemaría Escrivá de Balaguer





PONTIFICIA UNIVERSIDAD CATÓLICA DEL PERÚ

Summary

Facultad de Ciencias e Ingeniería
Sciences academic department

Doctor in Physics

**Analysis of the physical properties and photoelectrochemical behavior of
c-Si/a-SiC:H(p) photocathodes for solar water splitting**

by María del Carmen MEJIA CHUECA

Photoelectrochemical (PEC) processes have become an efficient and viable method for solar energy conversion into zero-emission fuels by harnessing and storage the power of the sun, which offers an environment-friendly approach. Hydrogen is considered as a sustainable and suitable energy alternative in comparison to energy systems based on the consumption of conventional hydrocarbon fuels. In particular, hydrogen production by PEC water splitting represents an attractive alternative to enhance the efficiency of water splitting process using sun light. Current research in this field is devoted to the fabrication and evaluation of new photoactive materials that upon sunlight absorption enable water-splitting PEC reactions with high efficiency and durability.

Silicon based compounds offer a good opportunity as photoactive material due to its high abundance and current scalable technologies. Silicon is the eighth most abundant element in the universe and constitutes up to 27.2% of the earth's crust weight [1]. Particularly, hydrogenated amorphous silicon carbide (a-SiC:H) thin films have been tested as photocathode material for photo-assisted electrolysis, exhibiting solar to hydrogen conversion efficiencies up to 7.5 %. Due to the capability to tailor the bandgap (1.8 - 3.3 eV) by the incorporation of carbon in a-Si:H, this material has turned out to be a promising candidate for PEC cells, fulfilling the optical bandgap (E_{gap}) primary requirement, i.e. $E_{\text{gap}} > 2.2$ eV. Additionally, the carbon incorporation leads to an enhancement of the corrosion resistance properties in aqueous media. It has been theoretically estimated that a PEC device with an a-Si_{0.9}C_{0.1}:H absorption layer exhibiting 2.0 eV of energy bandgap, can generate a photocurrent density J_{ph} of 15 mA/cm² (solar-to-hydrogen conversion efficiency ~18 %) when submitted to an Air mass (AM) 1.5 solar spectrum [2]. The specific value of 1.5 for the Air mass is selected for standardization purposes, based on the analysis of solar irradiance data in the United States, and corresponds to a power of 1000 W/cm² [3]. In the present work, a similar material a-Si_{0.5}C_{0.5}:H exhibiting 2.76 eV of energy bandgap generates a J_{ph} of 17 mA/cm² when submitted to the same light spectrum. This reflects an improvement in the use of a-SiC:H in PEC water splitting. Research on single thin film photoactive materials does not typically consider the role of the silicon substrate in the photoelectrochemical performance. In this sense, the photoelectrode is a system formed by a p-p, n-n or n-p structure, which depending on the depth of the space charge region may have an important impact on the photoelectrode performance. In this work, this substrate effect has been considered and studied.

PEC performance of a-SiC:H is often limited by its non-ideal energy band-edge alignment to the H₂O/O₂ redox potential, thus limiting the oxygen evolution reaction (OER) and the whole water splitting process [4]. To overcome this downside, an external bias needs to be applied, contributing to counteract the overpotential required to trigger the direct water splitting reaction. The external bias also contributes to reduce overpotentials due to the presence of a surface SiO₂ barrier layer and compensates interface charge carriers recombination as well.

Previous studies have demonstrated that by removing the SiO₂ native layer

from a-SiC:H(i) surface, J_{ph} values over 6 mA/cm^2 can be achieved at a potential of -1.4 V vs. Ag/AgCl in contrast to values lower than $< 4 \text{ mA/cm}^2$ obtained without the oxide removal. In fact, the existence of surface states (SS) originated from the hydroxyl group termination on the oxide surface, form an electronic state that is typically located within the semiconductor bandgap. The theory that such states act as recombination centers for minority photo carriers, fits quite well with the assumption that surface recombination competes with charge transfer from the semiconductor band towards the electrolyte. Additionally, it has been reported that depending on the density and energetic position of SS, these can provide another favorable pathway for indirect charge transfer to the solution, competing with the undesirable recombination mechanism. Knowledge in this field is limited to full-drift diffusion simulations in steady-state and dynamic regimes for photo-anodic currents in crystalline materials. In the current work, an experimental study has been carried out over an amorphous material (a-SiC:H) acting as photocathode for PEC water splitting. Thus, adding knowledge in this field.

Attempts to understand the role of a-SiC defects in PEC water splitting performance have been carried out in 2009 by Simonds et al. [5]. As a result of these, defects density in the bulk of the a-SiC increases with carbon concentration, from $\sim 9 \times 10^{16} \text{ cm}^{-3}$ (6%C) to $\sim 8 \times 10^{17} \text{ cm}^{-3}$ (11%C), leading to a reduction of the PEC performance. On the other hand, defect densities in the SiC/SiO₂ interface (SS) were approximated by Gaussian distributions with maximums of $\sim 2 \times 10^{12} \text{ cm}^{-2} \cdot \text{eV}^{-1}$ (Ivanov et al. [6]). The latter finding was retrieved from Capacitance-Voltage (C-V) measurements over metal-oxide-semiconductor (MOS) structures, and fit quite well with the SiC SS density distributions reported in this work.

The current work consists in three parts. In the first part, Bandgap engineering of a-SiC:H thin films was carried out to assess the material light absorption without compromising its photoelectrochemical water splitting capabilities. The tailoring was performed by varying the hydrogen concentration in the semiconductor and by post-deposition isochronal annealing treatments from 200 to 700 °C. By isochronal annealing, the same sample is submitted to the different temperature steps, from low to high temperature. After this analysis, the most suitable samples for water splitting application were evaluated as photocathodes in 1 M sulfuric acid under chopped light illumination. These a-SiC:H samples were doped with aluminum and deposited on different Silicon substrate conductivity types to assess the substrate influence in the a-SiC:H(Al) photocurrent response. This constitutes the second part of the work. Finally, in the third part, the role of SS in the photocathodic current for a-SiC:H(Al) absorber layers was experimentally analyzed. This analysis was based on steady-state and dynamic electrochemical models. Results concerning a-SiC:H(Al) photocathode stability under darkness and illumination conditions are also shown and discussed in this part.

Concerning the findings and the novelty in this work, localized a-SiC:H(Al)/SiO₂ SS would take part in a desirable mechanism of indirect electron charge transfer

to the electrolyte, and thus, conduct hydrogen evolution reaction. Related to the SiO_2 native layer, the evidence suggests that the SiO_2 layer reduction during PEC tests triggers a favorable semiconductor-electrolyte interface. This interface exhibits less overpotential barriers which promotes photocurrent generation. A correlation exists between the retrieved SS density (N_{SS}) and Urbach energy (E_{U}) values. The E_{U} is associated with disorder-induced electronic tail states or Urbach tails, which are localized states near the semiconductor band-edges. This correlation, as well as other a-SiC:H(Al)/ SiO_2 interface studies, support the reliability of our N_{SS} calculations for the c-Si(p)/a-SiC:H(Al)/ SiO_2 /electrolyte system. Finally, a charge transfer mechanism assisted by photogenerated minority carriers from the c-Si substrate has been also proposed in this work.



Acknowledgements

This thesis was funded by the Concytec doctoral scholarships under the grant No. 236-2015-FONDECYT and was developed in the framework of the Concytec project under the agreement 147-2017-FONDECYT, with the support of the Materials Characterization Center (CAM-PUCP).

First and foremost, I would like to thank to Prof. Dr Jorge Andres Guerra and Prof. Dr. Francisco Rumiche who enabled me to research in such a hot issue of these days. The patience, dedication and principally the trust placed in me, are valuable treasure that I will keep as lasting memory.

Beside my advisors, I would like to thank to Prof. Dr. rer. nat. habil. Dr. h.c. Andreas Bund from the Technische Universität Ilmenau- Germany for all the trust, and willingness to support this work at all times. For accepting me in his group- Electrochemistry and Electroplating Group- during my three internship stays.

My sincere thanks also goes to M. Sc. Mario Kurniawan from TU Ilmenau, M. Sc. Luis Francisco Sánchez, Prof. Dr Amaru Palomino and Prof. Dr. Rolf Grieseler from PUCP, for transmitting all their knowledge and experiences in their respective expertise areas.

Further, I would like to express my gratitude to Dr. Henry Romanus and M.Sc. Hauke-Lars Honig, from TU Ilmenau, and to M. Sc. Luis Conde, from PUCP, for all the technical support in the electronic and SEM characterization topics.

Last but by no means least, I wish also to thank my father God, who has been my motivation and for whom have I offered all this work. My engine, along with my extended family during all this 4-year period.

Contents

| | |
|---|-------------|
| Declaration of Authorship | ii |
| Summary | v |
| Acknowledgements | viii |
| 1 Theoretical framework | 1 |
| 1.1 Photoelectrochemical (PEC) systems for hydrogen production | 1 |
| 1.1.1 The Photoelectrochemical cell | 2 |
| Space charge and band bending | 3 |
| The three-electrode setup of the PEC cell | 6 |
| 1.1.2 Semiconducting photoelectrode materials and other issues in PEC research | 7 |
| 1.2 Thermodynamic for hydrogen production by PEC water-splitting . . . | 8 |
| 1.3 Kinetic considerations for hydrogen production by PEC water splitting | 11 |
| 1.3.1 The fluctuating energy level of ions in solution | 11 |
| 1.3.2 Interfacial electron transfer: semiconductors vs metals | 13 |
| 1.4 The study of the electrolyte interface | 15 |
| 1.4.1 The steady state regime | 15 |
| 1.4.2 Current-Potential (I-V) curves | 16 |
| 1.4.3 The dynamic regime | 18 |
| 1.5 Developing photopotential harvesting the solar spectrum | 20 |
| 1.6 a-SiC:H(p) as photocathode for PEC water-splitting | 20 |
| 1.7 Amorphous SiC | 22 |
| 1.7.1 Amorphous structure of SiC | 23 |
| 1.7.2 SiC thin films: main fabrication methods | 24 |
| 1.8 Fundamental absorption theories | 26 |
| 2 Experimental details | 28 |
| 2.1 a-SiC layer deposition | 28 |
| 2.2 Structural and morphological characterization | 31 |
| 2.3 Optical and vibrational characterization | 32 |
| 2.4 Photoelectrochemical characterization | 33 |
| 2.5 Evaluation of the substrate influence in the photocurrent response . . . | 33 |

| | |
|---|-----------|
| 3 Results and discussion | 35 |
| 3.1 Bandgap engineering, structural and electrical characterization of a-SiC film-based photocathodes | 35 |
| 3.1.1 Optical characterization of a-SiC thin films | 35 |
| 3.1.2 Structural and electrical analysis of a-SiC thin films | 38 |
| 3.1.3 Summary of Section 3.1 | 44 |
| 3.2 Substrate influence in the photocurrent response of the a-SiC:H(Al) absorber layer | 45 |
| 3.2.1 Isotype and anisotype heterojunctions | 46 |
| 3.2.2 Isotype and anisotype heterojunctions: role in PEC performance | 46 |
| 3.2.3 Substrate influence by direct contact with the electrolyte | 51 |
| 3.2.4 Summary of Section 3.2 | 51 |
| 3.3 a-SiC:H(Al) surface states influence in water splitting reaction | 53 |
| 3.3.1 Structural and morphological characterization | 53 |
| 3.3.2 Photoelectrochemical characterization | 54 |
| Electrochemical Impedance Spectroscopy | 57 |
| Open Circuit Potential | 63 |
| 3.3.3 Summary of Section 3.3 | 66 |
| 4 Conclusions | 67 |
| A Seminars and publications | 69 |
| Bibliography | 70 |

List of Figures

| | | |
|-----|---|---|
| 1.1 | Schematic representation of water splitting assisted by solar energy to produce hydrogen as fuel. The oxygen evolution reaction (OER) takes place at the anode, while the hydrogen evolution reaction (HER) takes place at the cathode, acting as photoelectrode. Half-redox reactions are depicted with their respective standard potentials (E_{ox}° , E_{red}°) to yield the whole water splitting reaction (E_{redox}°). Adapted from Gimenez et al. (2016) [12]. | 1 |
| 1.2 | Band structure of a p-type photocathode water splitting device. Various processes are illustrated, such as photon absorption, electron-hole pair formation, charge carrier extraction/migration, and interfacial reactions at the electrode surfaces. Energetic requirements associated to the minimum thermodynamic energy to split water, catalytic overpotentials for the HER and OER (η_{red} and η_{ox} , respectively), and photopotential ($\Delta\mu$) are also illustrated. Maximum $\Delta\mu$ coincides with the difference in quasi-Fermi energy levels of holes (pE_{F}^*) and electrons (nE_{F}^*) at the surface. | 3 |
| 1.3 | The semiconductor-electrolyte interface before and after contact (equilibration) of the two phases, shown for a p-type semiconductor. The redox system corresponds to the standard hydrogen electrode (NHE). | 4 |
| 1.4 | Formation of space charge region (SCR) at a metal oxide or silicon based semiconductor surface when exposed to air. SS represents the surface states. While DOS, the density of states of the SS. Adapted from Krol (2012) [20]. | 5 |
| 1.5 | Band bending at the surface of a p-type semiconductor in depletion condition. The "-" markers just above the valence band represent the ionized acceptor species, whereas the "+" markers below the valence band level represent the free holes. The potential in the bulk of the semiconductor is chosen as zero. ρ represents the charge density. Parameters shown in Eqs. 1.6, 1.7 and 1.8, can be identified. Adapted from Krol (2012) [20]. | 5 |
| 1.6 | Experimental setup for measuring the performance of a photoelectrode under simulated sunlight AM 1.5. Basic components of a PEC cell are shown. Adapted from krol and Gimenez [12, 20]. | 6 |

- 1.7 Band diagram for a PEC cell based on an p-type semiconducting photocathode that is electrically connected to a metal counter electrode. In equilibrium in the dark (left) and under illumination (right). Illumination decays the Fermi level and decreases the band bending. Adapted from Krol et al. [20]. 8
- 1.8 Band diagram, density of states, Fermi-Dirac distribution and charge carrier concentration for a p-type semiconductor (a). quasi-Fermi energy levels of electrons (nE_F^*) and holes (pE_F^*) have the same value at equilibrium conditions (dark). Under Illumination, nE_F^* and pE_F^* change respect to the equilibrium case according to Eqs. 1.13 and 1.14 (b). As a result, thermodynamic requirements for water splitting is accomplished (b). Adapted from Peter et al. (2016) [23]. 9
- 1.9 Diode behaviour of the p-type semiconductor-electrolyte interface in dark conditions. The junction blocks the electron flow from left to right under reverse bias. While electrons can pass from right to the left as forward bias reduces the band bending. As bias is applied, depletion, flat band and accumulation conditions are formed at the interface. . . . 10
- 1.10 Electron energies of H^+/H_2 redox system (a) and corresponding distribution functions for $E_{red}^o (D_{red})$ and $E_{ox}^o (D_{ox})$ (b). λ is the reorganization energy for H^+ and H_2 . For equal concentration of H^+ and H_2 , λ is the same for both species. Inner and outer spheres are depicted in (b). Adapted from Peter (2016) [23]. 12
- 1.11 Electron energies in solid electrodes in contact with a redox system vs density of states of ions in solution: for metal electrode (a) and for p-type semiconductor electrode (b). Energy level model of electron transfer from a p-type semiconductor to oxidized species in solution under equilibrium condition. No overlapping is observed between the DOS in the valence band and D_{ox} (c). 13
- 1.12 Energy level model of electron transfer from the conduction band in a p-type semiconductor to a redox species in solution under illumination. A large overlap between DOS of the oxidized species D_{ox} and the energy of the electron in the conduction band gives high currents (a) compared with currents obtained with smaller overlapping (b). nE_F^* is not depicted for simplification. Adapted from Krol et al (2012) [20]. . . 14
- 1.13 The three double layers at the semiconductor-electrolyte interface on the example of aqueous solution of H_2SO_4 . SCR is the space charge layer, HL is the Helmholtz layer and GL, the Gouy layer. All of them form the semiconductor-electrolyte interface 17

| | | |
|------|---|----|
| 1.14 | Schematic J-V diagram for a p-type semiconductor-electrolyte-metal configuration. Photocurrent is observed when the potential is applied in the reverse bias condition. Application of high forward bias, may conduct to oxidation at the semiconductor surface. The flat band potential does not usually coincide with the onset potential. Adapted from Fujii (2016) [17]. | 17 |
| 1.15 | Representation of the complex impedance (a). Sinusoidal voltage \tilde{V} and current \tilde{j} from which the complex impedance is calculated (b). Adapted from [12]. | 19 |
| 1.16 | Equivalent circuits for photoelectrochemical cells. Extensive circuit containing contributions from the semiconductor/back contact interface ($R_{\text{contact}}, C_{\text{contact}}$), the semiconductor bulk resistance (R_{bulk}), the space charge region ($R_{\text{SC}}, C_{\text{SC}}$), the surface states ($R_{\text{SS}}, C_{\text{SS}}$), the Helmholtz layer ($R_{\text{HL}}, C_{\text{HL}}$) and the electrolyte resistance (R_{sol}) (a). The most simple equivalent circuit in which only the space charge region capacitance and the electrolyte resistance take place (b). The most common circuit used in practice for photoelectrodes (c). Adapted from [12]. | 19 |
| 1.17 | The AM 1.5 Global Tilt spectrum shown as solar photon flux as a function of wavelength and photon energy [ASTM]. The portion of the solar spectrum harvested by various band-gap energy semiconductors are indicated. Bandgap engineering of a-SiC:H semiconductor films varying the hydrogen concentration and upon different annealing steps was performed in this study to obtain an optimal bandgap value for PEC water splitting applications. The results of this work are summarized on the top of the solar spectrum image. | 21 |
| 1.18 | Example structure proposed for the a-Si _{1-x} C _x :H system. Si (●), C (●) and H (●) atoms are observed conforming a-SiC, a-Si and a-C networks. Rich a-Si and a-C regions are enclosed in blue and black dashed lines, respectively. | 24 |
| 1.19 | Schematic representation of a Magnetron sputtering system. Thin film deposition profile is achieved by varying the magnetron powers corresponding to the main and doping atom targets. Ar gas is ionized to create the plasma applying a voltage between cathode and anode. | 25 |
| 2.1 | Techniques used to characterize and evaluate the a-SiC layers as potential photocathodes. | 29 |
| 2.2 | Scheme of sputtering chamber used for the a-SiC:H(Al) thin films fabrication (a) Radiofrequency Co-sputtering plasma formation with SiC and Al targets (b). | 30 |
| 2.3 | Detail of the three electrode setup photoelectrochemical cell. A standard AM 1.5 solar spectrum was used to test photocathodes electrochemically. Cell design provided by TU Ilmenau (Germany). | 32 |

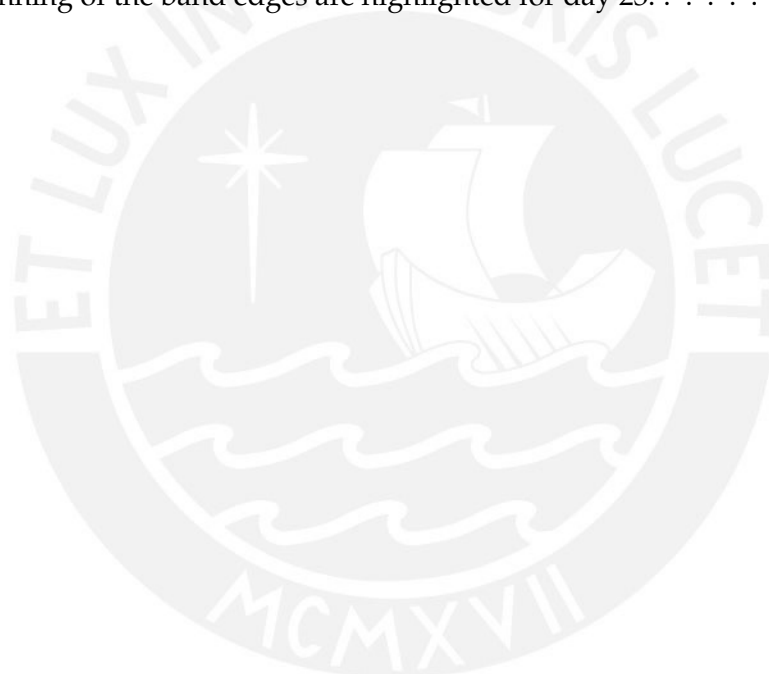
| | | |
|-----|--|----|
| 3.1 | Optical transmittance (a) and absorption coefficient in the Tauc scale (b) of the a-SiC:H layers. The solid lines in (a) correspond to the fits following the modified envelope method [90]. The red solid curves denote fits using the dilogarithm equation (Eq. 1.28) (b). The gray dashed lines correspond to linear fits (Eq. 1.26) in the Tauc region (b). The legend denotes the different hydrogen concentrations ($\times 10^{21}$ atoms/cm ³) of the as grown state. | 36 |
| 3.2 | Energy bandgaps of the a-SiC:H films extracted by means of three methods: isoabsorption (E_{04}) (a), Tauc (E_{Tauc}) (b) and band fluctuations ($E_{B,F}$) (c). The legend denotes the different hydrogen concentrations ($\times 10^{21}$ atoms/cm ³) obtained after deposition before thermal treatments. The highlighted regions in (b) and (c) denote the region of optimal E_{gap} for solar water splitting purposes. | 36 |
| 3.3 | Thickness variation of the a-SiC:H samples that takes place upon each step of isochronical annealing treatment. The legend denotes the different hydrogen concentrations ($\times 10^{21}$ atoms/cm ³) obtained in the as grown state. Values are expressed as relative thicknesses for comparison purposes. | 37 |
| 3.4 | FESEM Tilt-section images of c-Si(p)/a-SiC:H(p) as grown sample (a) and annealed sample (b). Thickness shrinking by about 55 nm is highlighted. | 38 |
| 3.5 | Current-voltage curves for the a-SiC:H(Al) sample as grown and after annealing at 600 °C. Ohmic behavior was achieved after performing the heating process. | 39 |
| 3.6 | Absorption coefficient (a), Bond density (b) and Si-H frequency shifting (c) obtained for the a-SiC:H(Al) sample grown with 1.57×10^{21} atoms/cm ³ of hydrogen, after each annealing step. Bond density values (b) according to Eq. 3.2. Differences in chemical environment of the Si-H bonds were monitored by means of Si-H frequency shifting (c). 40 | 40 |
| 3.7 | E_U (red squares) and FWHM values (gray circles) for the a-SiC:H(Al) sample with the lowest hydrogen concentration, i.e. grown with $[H] = 1.57 \times 10^{21}$ atoms/cm ³ (a). Relative density variation with annealing temperature for the hydrogenated samples (b). | 41 |
| 3.8 | Raman spectra after different annealing steps obtained for the non hydrogenated a-SiC sample. Si-Si and C-C bands are highlighted (a). Raman spectra of the a-SiC:H(Al) sample ($[H] = 1.57 \times 10^{21}$ atoms/cm ³) for the as grown and the annealed state at 600 °C. An increment in the Si-Si, Si-C and C-C modes is detected after the heating process (b). A 488 nm Ar ⁺ laser line was used as excitation source. | 42 |

- 3.9 E_U (a) and FWHM values (b) for the a-SiC samples. The legend denotes the different hydrogen concentrations ($\times 10^{21}$ atoms/cm³) obtained in the as grown state. The same trend is observed for the E_U curves and their corresponding FWHM curves for the hydrogenates samples. The E_U behavior at the 300 °C annealing step, marked with the solid gray line (a) reveals the effect of hydrogen presence over the short range localized structural ordering exhibited in the a-SiC matrices. E_U is shifted towards lower values, below the corresponding dashed trend line (a), as the hydrogen content increases in the samples. On the contrary, for the sample without hydrogen, an E_U shifts towards higher values, above the dashed trend line (a), is observed at 300 °C. 43
- 3.10 Example structures proposed for the a-Si_xC_{1-x}:H system in as grown and an annealed state at 600 °C. Si (●), C (●) and H (●) atoms are observed forming a-SiC, a-Si and a-C networks. Rich a-Si and a-C regions are enclosed in blue and black dashed lines, respectively. Disorder increases after thermally-induced hydrogen releasing. Since hydrogen atoms are depleted upon the annealing treatment, more a-C rich regions are expected. Hydrogen remanent atoms in the annealed state are preferably found bonded with carbon atoms instead of silicon atoms. 44
- 3.11 Anisotype c-Si(n)/a-SiC(Al) vs isotype c-Si(p)/a-SiC(Al) heterojunctions. Band diagrams of the Si and SiC semiconductors are shown with respect to the solid state and standard electrochemical scale. Electronic affinity values (χ) are constant, while work functions (ϕ) change with the level of impurities or dopant atoms. Presence of the native SiO₂ layer on the Si substrate adds donor-like behavior SS at the solid-solid interface. These SS play a crucial role in the formation of the space charge region on both sides of the junction. ΔE_{CB} and ΔE_{VB} represent the energy variation between the semiconductors band edges at the interface. 47
- 3.12 LSV curves: for the c-Si(n)/a-SiC:H(Al) and c-Si(p)/a-SiC:H(Al) systems in AG state (a). The c-Si(n)/a-SiC:H(Al) system after being subjected to isochronal annealing treatments at different temperatures. An in-sequence LSV tests reveal possible photocorrosion in the a-SiC thin film (b). The c-Si(n)/a-SiC:H(Al) system after annealed at 600 °C, in an in-sequence LSV test and at different times, after exposure to air (c). Tests were performed in H₂SO₄ (1 M) 48

- 3.13 Energy band diagrams of PEC components: c-Si(n)/a-SiC:H(Al) photocathode, anode (Pt) and light illumination, at reverse (a) and forward (b) bias condition. nE_F^* and pE_F^* are the quasi-Fermi energy levels of electrons and holes, respectively. E_{redox}^0 corresponds to the standard redox potential for oxygen evolution reaction taking place in the Pt counter electrode, whose fluctuation distribution of energy levels are D_{red} and D_{ox} 50
- 3.14 SEM images of c-Si/a-SiC:H(Al): Cross-section of the sample in As grown state (a) and after annealing at 800 °C (b). Cross-section of the at 800 °C annealed sample after cross-section milling by Focused Ion Beam (FIB). A columnar structure is observed (c). Top-section of the annealed sample at 800 °C (d). Carbon and platinum were deposited as protection layers for subsequent cross-section milling. The a-SiC:H(Al) film shrinking with annealing is highlighted. 52
- 3.15 XRD patterns of Al doped a-SiC:H(Al) in as grown (AG) state and after annealing at 600 °C. Inset depicts the Raman spectra for both cases. An increment in the Si-Si, Si-C and C-C modes is detected after the heating process. 53
- 3.16 AFM images taken from c-Si(p)/a-SiC:H(Al) sample in as grown state before being photoelectrochemically tested (a), in as grown state after photoelectrochemical test (b) and after annealing treatment at 600 °C and photoelectrochemical test (c). Root-mean-squared roughness values R_q are shown below each image. 54
- 3.17 J-V polarization curves of c-Si(p)/a-SiC:H(Al) for the as grown (AG) and annealed sample. Inset depicts a magnification of current at low reverse bias. -0.3 V is the potential from which appreciable photocurrent is observed, whilst -1.7 V is the potential at which photocurrent saturation is observed (a). Steady-state polarization curves were obtained by taken logarithm of the photocurrents. The Tafel regions identified are indicated by the triangular features (b). Recombination processes are appreciated for the sample AG as an unstable current, at low and high bias. For the annealed sample: -0.5 V is the potential at which photocurrent starts to saturate, -0.9 V sets the potential at which a change in Tafel slope is detected. At -1.7 V, photocurrent reaches saturation (b). Tests were performed in H₂SO₄ (1 M). 55
- 3.18 J-V current density for the 600 °C annealed c-Si(p)/a-SiC:H(Al) photocathode in the darkness (gray curve) and under illumination (red curve). There is a noticeable an abrupt increase of the J_{ph} at the potential in which the dark current density starts to raise, at -0.25 V. Tests were performed in H₂SO₄ (1 M) 56

- 3.19 Energy band diagrams of PEC components: c-Si(p)/a-SiC:H(Al) photocathode, anode (Pt) and light illumination, at condition from which appreciable photocurrent is observed (a) and in the ideal band edge pinned situation (b). pE_F^* is the quasi-Fermi energy level of holes, represented in each layer. E_{redox}^o corresponds to the standard redox potential for oxygen evolution reaction taking place in the Pt counter electrode, whose fluctuation distribution of energy levels are D_{red} and D_{ox} . pE_F^* of the a-SiC:H(Al) layer is connected to the external Fermi level of the metal contact since the ohmic contact for this sample was only achieved at the top of the a-SiC:H(Al) layer. 57
- 3.20 Mott-Schottky plots for the c-Si(p)/a-SiC:H(Al) heterojunction annealed at 600 °C at frequencies of 30, 40, 50 and 60 kHz. The inset table shows the flat band potential and carrier concentration values obtained from the linear fits performed for each frequency data. Tests were performed in H₂SO₄ (1 M) 58
- 3.21 Simulated capacitance variation of the space charge and surface states upon applied potential for the annealed sample (a). Potential drop across the space charge, the double layer and surface states is shown. Negligible potential changing is observed across the double layer ($C_{\text{dl}} \gg C_{\text{SC}}$), whose potential values are scaled 20 times up for viewing purposes (b). Nyquist plot curves and fits (dash lines) obtained from EIS measurements at negative (c) and positive (d) potentials. Each cycle represents the impedance response of the c-Si(p)/a-SiC:H(Al)/1 M H₂SO₄ system at a certain applied voltage. 60
- 3.22 Energy band diagram and schematic of the c-Si(p)/a-SiC:H(Al)/SS/H₂SO₄ 1 M electrolyte junction in a state of depletion under donor-like surface states (D_S) charging (a), neutrality condition (b) and surface states discharging (c). Where E_C is the conduction band energy, E_V the valence band energy, E_F the Fermi level and A_b the bulk acceptors energy level. Thermodynamic redox potentials for hydrogen and oxygen evolution reactions, HER and OER respectively, are shown following the same energy scale. Note that thermodynamic requirement for HER is achieved as hydrogen redox potential is fixed below D_S 61
- 3.23 Energy band diagram and schematic of the c-Si(p)/a-SiC:H(Al)/SS/H₂SO₄ 1 M electrolyte junction in a state of accumulation. The presence of an accumulation layer in p-type semiconductors requires partially filled acceptor-like surface states (A_S). 61
- 3.24 Mott-Schottky plot at frequency of 50 kHz and potential-dependent charge in surface states. Surface states charge distributions centered at -0.5 V and 0.25 V are correlated to the variation in the SCR electronic capacitance behavior observed in the Mott-Schottky plot. 62

- 3.25 OCP in-sequence tests for the a-SiC:H(Al) layer. Measurements were performed in different times using the same 1 M H₂SO₄ electrolyte. For comparison purposes, V_{ph} values for a-SiC:H(Al) and the c-Si(p) substrate are shown. Temperature was recorded during the whole test, inside the electrolyte and at the back contact zone. No similar trend is observed between the temperature variation and the OCP signal. Then, instability in the OCP is associated to semiconductor conditions which are depicted in the band diagrams. 64
- 3.26 The band diagrams that illustrate the electrode surface conditions proposed according to the OCP in-sequence tests for the a-SiC:H(Al) layer. OCP measurements were performed in different times using the same 1 M H₂SO₄ electrolyte. The conditions depicted are for day 1 and day 23. Recombination processes prone to take place due to the unpinning of the band edges are highlighted for day 23. 66



List of Tables

| | | |
|-----|--|----|
| 1.1 | SiC relevant bonds and bond lengths [75]. | 23 |
| 1.2 | Covalent radio and electronegativity of the atoms in the SiC network [75]. | 24 |
| 2.1 | Parameters of the a-SiC layers with 0 (a), 1.57 (b), 3.10 (c) and 4.45 (d) $\times 10^{21}$ atoms/cm ³ of hydrogen in AG state, respectively. Energy bandgap values were retrieved following the models described in Sec. 1.8. | 31 |
| 2.2 | Annealing treatment parameters of the a-SiC layers with 0 (a), 1.57 (b), 3.10 (c) and 4.45 (d) $\times 10^{21}$ atoms/cm ³ of hydrogen in AG state, respectively. | 31 |
| 2.3 | a-SiC:H(Al) thin films parameters used to evaluate the substrate influence in the photocurrent response of the c-Si(p)/a-SiC:H(Al) and c-Si(n)/a-SiC:H(Al) photocathodes. Energy bandgap values were retrieved following the models described in Sec. 1.8. | 33 |
| 3.1 | Vibrational states and inverse absorption cross sections (k') for the different bonds presented in a-SiC:H thin films. | 39 |
| 3.2 | a-SiC:H(Al) thickness variation (nm) with annealing treatment for the c-Si(n)/a-SiC:H(Al) system. | 49 |

List of Symbols

| Symbol | Description | Units |
|---|--|-----------------------|
| E_{red}° | standard potential for hydrogen evolution reaction | V |
| E_{ox}° | standard potential for oxygen evolution reaction | V |
| \hbar | Planck constant | J Hz |
| ω | frequency | Hz |
| $\hbar\omega$ | photon energy | eV |
| E_{gap} | optical bandgap energy | eV |
| η_{red} | catalytic overpotential for the hydrogen evolution reaction | V |
| η_{ox} | catalytic overpotential for the oxygen evolution reaction | V |
| $\Delta\mu$ | internal photopotential | V |
| nE_{F}^* | quasi-Fermi energy level of electrons | eV |
| pE_{F}^* | quasi-Fermi energy level of holes | eV |
| E_{C} | conduction band energy | eV |
| E_{V} | valence band energy | eV |
| E_{F} | Fermi energy level | eV |
| ΔG | Gibbs free energy change | eV |
| n' | number of electrons transferred in the half redox reaction | - |
| F | Faraday constant | C |
| ΔE | electrochemical cell voltage | V |
| $E_{\text{redox}}^{\circ} / E_{\text{NHE}}^{\circ}$ | standard redox potential | V |
| $E_{\text{F,redox}} / E_{\text{F,equil}}$ | standard redox potential in vacuum scale | eV |
| N_{A}^{-} | density of ionized acceptors | atoms/cm ³ |
| V_{SC} | built-in voltage | V |
| W | space charge region width | nm |
| N_{A} | density of shallow acceptors or doping concentration for p-type semiconductor | atoms/cm ³ |
| SCR | Semiconductor Space Charge Region | - |
| Q_{SS} | charge stored in surface states | C |
| Q_{SC} | charge stored in the space charge region | C |
| ϵ_0 | vacuum permittivity | F/ m |
| ϵ_r | relative permittivity | - |
| e | electronic charge | C |
| A | area of the surface electrode in contact with the electrolyte | cm ² |

| | | |
|------------------|--|-------------------------------------|
| ϕ_{SC} | potential distribution of the space charge region | eV |
| κ | Boltzmann constant | $\text{kg m}^2/\text{s}^2 \text{K}$ |
| T | temperature | K |
| ϕ_S | potential at the semiconductor surface | eV |
| n | electron density | cm^{-3} |
| h | hole density | cm^{-3} |
| $N(E)$ | total density of energy states | $\text{eV}^{-1} \text{cm}^{-3}$ |
| $f(E)$ | Fermi-dirac distribution function | eV vs P(f) |
| N_C | density of states around the bottom of the conduction band | $\text{eV}^{-1} \text{cm}^{-3}$ |
| N_V | density of states around the bottom of the valence band | $\text{eV}^{-1} \text{cm}^{-3}$ |
| V_{ph} | internal photovoltage | V |
| n_0 | electron density in equilibrium and dark conditions | cm^{-3} |
| p_0 | hole density in equilibrium and dark conditions | cm^{-3} |
| m^* | effective mass | kg |
| λ | reorganization energy | eV |
| I^0 | ionization energy | kJ mol^{-1} |
| A^0 / χ | electron affinity | kJ mol^{-1} |
| DOS | density of states | $\text{eV}^{-1} \text{cm}^{-3}$ |
| D_{red} | DOS of reduced species in solution | $\text{eV}^{-1} \text{cm}^{-3}$ |
| D_{ox} | DOS of oxidized species in solution | $\text{eV}^{-1} \text{cm}^{-3}$ |
| FWHM | full width half maximum | cm^{-1} |
| $W_{red}(E)$ | fluctuation of the energy level of the reduced species | eV vs P(W) |
| $W_{ox}(E)$ | fluctuation of the energy level of the oxidized species | eV vs P(W) |
| c_{red} | concentration of reduced species in solution | cm^{-3} |
| c_{ox} | concentration of oxidized species in solution | cm^{-3} |
| E_C^S | energy at the bottom of the conduction band | eV |
| E_V^S | energy at the top of the valence band | eV |
| j_C^- | cathodic conduction band current | A |
| j_C^+ | anodic conduction band current | A |
| j_V^- | cathodic valence band current | A |
| j_V^+ | anodic valence band current | A |
| K_C^- | quantum-mechanical tunneling coefficient for j_C^- | - |
| K_C^+ | quantum-mechanical tunneling coefficient for j_C^+ | - |
| K_V^- | quantum-mechanical tunneling coefficient for j_V^- | - |
| K_V^+ | quantum-mechanical tunneling coefficient for j_V^+ | - |
| n_S | surface concentration of free electrons | cm^{-3} |
| p_S | surface concentration of free holes | cm^{-3} |
| E_{Eq} | equilibrium potential | V |
| E | potential applied | V |
| R | universal gas constant | $\text{J mol}^{-1} \text{K}^{-1}$ |
| $a_{Ox_{elec}}$ | activity of the oxidized species in solution | - |
| $a_{Red_{elec}}$ | activity of the reduced species in solution | - |

| | | |
|--------------------------------|--|-------------------------------------|
| a | activity coefficient | - |
| v_{trans} | transport velocity of the electrolyzed species in solution | m s^{-1} |
| v_{elec} | electrolysis velocity | m s^{-1} |
| ϕ_{CB} | potential in the conduction band | V |
| ϕ_{VB} | potential in the valence band | V |
| V_{onset} | onset potential | V |
| V_{fb} | flatband potential | V |
| \tilde{V} | amplitude AC potential perturbation | V |
| \tilde{j} | oscillating current | A |
| $Z(\omega)$ | impedance | Ω |
| Z', Z_{re} | real part of the complex impedance | Ω |
| Z'', Z_{im} | imaginary part of the complex impedance | Ω |
| N_{SS} | density of surface states | cm^{-3} |
| C_{μ}^{SS} | surface state chemical capacitance | F |
| $C_{\mu\text{eq}}^{\text{SS}}$ | surface state chemical capacitance at equilibrium | F |
| V_0 | voltage amplitude of the complex impedance | V |
| j_0 | current amplitude of the complex impedance | A |
| $\Delta\theta$ | phase of the complex impedance | Ω |
| θ_V | voltage phase of the complex impedance | V |
| θ_j | current phase of the complex impedance | A |
| R_{contact} | semiconductor back contact resistance | Ω |
| C_{contact} | semiconductor back contact capacitance | F |
| R_{bulk} | semiconductor bulk resistance | Ω |
| R_{SCR} | semiconductor space charge region resistance | Ω |
| C_{SCR} | semiconductor space charge region capacitance | F |
| R_{SS} | surface states resistance | Ω |
| C_{SS} | surface states capacitance | F |
| $R_{\text{HL}}, R_{\text{dl}}$ | Helmholtz layer resistance | Ω |
| $C_{\text{HL}}, C_{\text{dl}}$ | Helmholtz layer capacitance | F |
| R_{sol} | electrolyte resistance | Ω |
| U_{loss} | entropic energy loss | eV |
| $\Delta\mu_{\text{ex}}$ | external available free energy to conduct water splitting reaction | eV |
| E_{photon} | energy of absorbed photon | eV |
| J_{ph} | photocurrent density | mA cm^{-2} |
| α | absorption coefficient | cm^{-1} |
| M_{Tauc} | Tauc slope | $\text{cm}^{-1/2} \text{eV}^{-1/2}$ |
| E_{Tauc} | Tauc bandgap | eV |
| E_{U} | Urbach energy | eV |
| E_{04} | isoabsorption bandgap | eV |
| $E_{\text{B.F}}$ | band fluctuations bandgap | eV |
| z | argument of the dilogarithm function | - |
| α_0 | coefficient related to the transition matrix element | cm^{-1} |

| | | |
|-------------------------|---|------------------------------|
| $\text{Li}_2(z)$ | dilogarithm function of z in band fluctuations model | - |
| T_A | annealing temperature | $^{\circ}\text{C}$ |
| n_{in} | refractive index | - |
| A_0 | Avogadro's number | mol^{-1} |
| α' | molecular electronic polarizability | $\text{C m}^2 \text{V}^{-1}$ |
| ρ | mass density | g cm^{-3} |
| p^+ | highly doped area in p-type | - |
| k' | inverse absorption cross section | cm^{-2} |
| ν | wavenumber | cm^{-1} |
| N | bond density | cm^{-3} |
| ΔE_{CB1} | potential barrier between Si(n) and SiC(p) conduction bands | eV |
| ΔE_{VB1} | potential barrier between Si(n) and SiC(p) valence bands | eV |
| ΔE_{CB2} | potential barrier between Si(p) and SiC(p) conduction bands | eV |
| ΔE_{VB2} | potential barrier between Si(p) and SiC(p) valence bands | eV |
| \emptyset | work function | eV |
| j_n | electron diffusion current | A |
| j_p | hole diffusion current | A |
| D_n, D_p | diffusion coefficient of electrons (n) and holes (p) | $\text{cm}^2 \text{s}^{-1}$ |
| n_i | intrinsic carrier density | cm^{-3} |
| N_D | doping concentration for n-type semiconductor | atoms/cm^{-3} |
| L_n, L_p | diffusion length of electrons (n) and holes (p) | μm |
| LSV | Linear Sweep Voltammetry | - |
| OCP | Open Circuit Potential | V |
| EIS | Electrochemical Impedance Spectroscopy | - |

Chapter 1

Theoretical framework

1.1 Photoelectrochemical (PEC) systems for hydrogen production

Photoelectrochemical (PEC) processes have become an efficient and viable method for solar energy conversion into zero-emission fuels by harnessing and storage the power of the sun, which offers an environment-friendly approach [7]. Hydrogen is considered as a sustainable and suitable energy alternative in comparison to energy systems based on the consumption of conventional hydrocarbon fuels. In particular, hydrogen production by PEC water splitting represents an attractive alternative to enhance the efficiency of water splitting process using sun light. Current research in this field is devoted to the fabrication and evaluation of new photoactive materials that upon sunlight absorption enable water-splitting PEC reactions with high efficiency and durability [8–11].

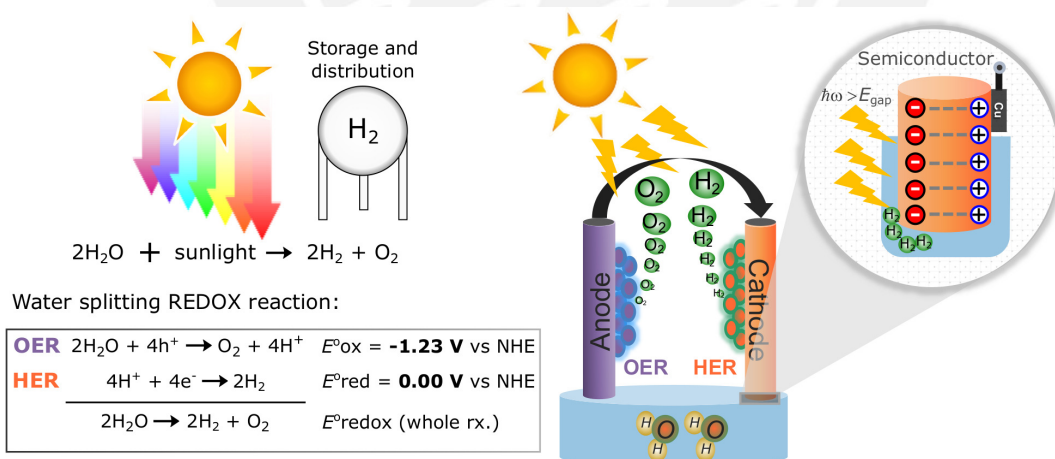
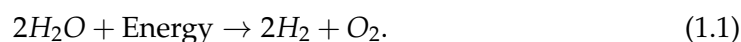


FIGURE 1.1: Schematic representation of water splitting assisted by solar energy to produce hydrogen as fuel. The oxygen evolution reaction (OER) takes place at the anode, while the hydrogen evolution reaction (HER) takes place at the cathode, acting as photoelectrode. Half-redox reactions are depicted with their respective standard potentials (E°_{ox} , E°_{red}) to yield the whole water splitting reaction (E°_{redox}). Adapted from Gimenez et al. (2016) [12].

Fig. 1.1 shows the PEC water splitting phenomenon. The phenomenon can be described as a water electrolysis process, assisted by a photocatalytic material acting

as photoanode or as photocathode. Fig. 1.1 depicts the case for a photocathode semiconductor material, where the reduction reaction; i.e. the hydrogen evolution reaction (HER), takes place. On the other hand, the oxidation reaction; i.e. the oxygen evolution reaction (OER), takes place at the another electrode, called anode. Nevertheless, more complicated configurations involving more than one photoelectrode; e.g. a photocathode for HER and a photoanode for OER, are also found in PEC cells [12]. In general, water splitting reaction can be represented as follows:

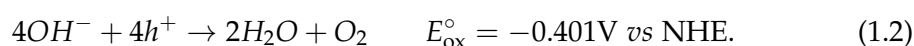


The energy required to conduct water splitting can proceed from any of the energy sources making it a highly flexible energy conversion technology. Renewable energy sources such as, hydro, solar and wind, have turned out to be promising candidates for that purpose [13]. Specially, the use of solar energy source offers variety of methods to conduct the Rx. 1.1: **thermochemically**, using high temperatures, between 500-2000 °C, for heating and driving a series of chemical reactions to produce H₂; **photosynthetically**, coupled to oxygenic and anoxygenic photosynthesis; **photocatalytically**, using heterogeneous photocatalysis; and **photoelectrochemically**, using absorber photoelectrodes. The implementation of these intermittent energy sources on a global scale lead to local energy storage and distribution via water splitting [14].

1.1.1 The Photoelectrochemical cell

Fig. 1.2 shows a simplified energy diagram of a photoelectrochemical (PEC) cell based on a single photocathode and an inert metal (Pt) counter electrode. The main component in PEC cells is the semiconductor, which upon sunlight absorption converts incident photons to electron-hole pairs. The absorption occurs when the energy of the photon $h\nu$ is equal or higher than the semiconductor optical energy bandgap (E_{gap}). Photogenerated electrons and holes are spatially separated from each other due to the existence of an electric field inside the semiconductor. The photogenerated electrons drift towards the electrolyte, driving the HER. While the photogenerated holes are swept towards the back contact until they reach the metal counter electrode by means of an external wire. Thus, OER takes place in the metal electrode acting as anode.

In the present work, for an acidic environment, rich in protons H⁺, the reduction and oxidation reactions for water splitting can be found in Fig. 1.1 [15]. The way the reactions are expressed is based on the dissociation of water into protons and hydroxyl ions OH⁻. The latter are found in higher concentrations in basic electrolytes. In that case, the reactions depicted in Fig. 1.1 can be expressed in terms of equilibrium of OH⁻ ions as follows [16]:



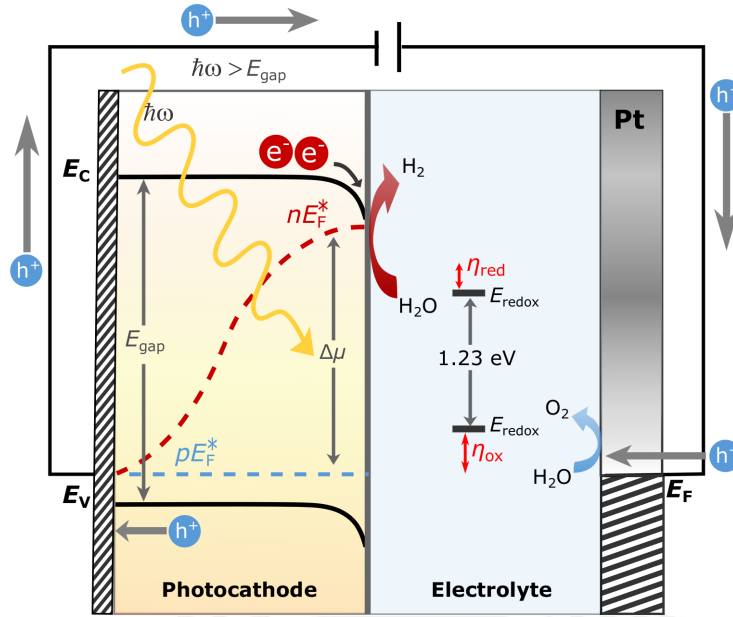


FIGURE 1.2: Band structure of a p-type photocathode water splitting device. Various processes are illustrated, such as photon absorption, electron-hole pair formation, charge carrier extraction/migration, and interfacial reactions at the electrode surfaces. Energetic requirements associated to the minimum thermodynamic energy to split water, catalytic overpotentials for the HER and OER (η_{red} and η_{ox} , respectively), and photopotential ($\Delta\mu$) are also illustrated. Maximum $\Delta\mu$ coincides with the difference in quasi-Fermi energy levels of holes (pE_{F}^*) and electrons (nE_{F}^*) at the surface.



The Gibbs free energy change for the overall water splitting reaction is given by 1.4:

$$\Delta G = -n' F \Delta E. \quad (1.4)$$

In Eq. 1.4, ΔG is the Gibbs free energy change, n' is the stoichiometry ratio between one molecule of the produced H_2 and the number of electrons needed to produce it electrochemically. For the case of hydrogen reduction reaction, $n' = 2$. F is the Faraday constant, 96500 C/mol and ΔE is the electrochemical cell voltage. At standard room temperature (298 K) and with a proton concentration of 1 mol/L (at 1 bar), the ΔE of -1.229 V corresponds to a ΔG of +237 kJ/mol H_2 [17].

Space charge and band bending

When a semiconductor is immersed into an electrolyte, equilibration of the semiconductor-electrolyte interface takes place. This implies the flow of charge from one phase to the other, as a result of which, a band bending arises within the semiconductor layer. After contact, the net consequence of equilibration is that $E_{\text{F}} = E_{\text{redox}}^\circ$ and a

built-in voltage V_{SC} is developed inside the semiconductor. The standard E_{redox}° in vacuum scale is stated as $E_{F,redox}$. Taking into account the traditionally used standard hydrogen electrode (NHE) scale in electrochemistry, NHE appears to lie at -4.5 eV with respect to the vacuum level. Then, for any redox species with its respective E_{redox}° (vs NHE), it is possible to define the corresponding $E_{F,redox}$ by the relation [18]:

$$E_{F,redox} = -4.5 \text{ eV} - eE_{redox}. \quad (1.5)$$

The interface equilibration phenomenon is illustrated in Fig. 1.3

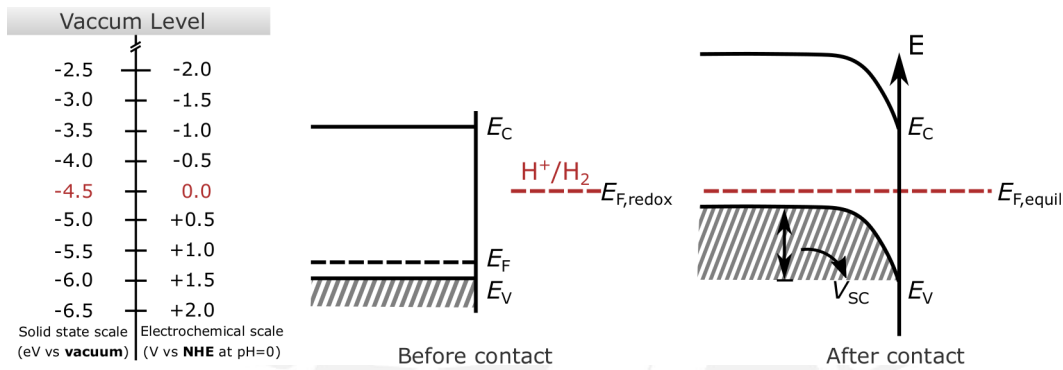


FIGURE 1.3: The semiconductor-electrolyte interface before and after contact (equilibration) of the two phases, shown for a p-type semiconductor. The redox system corresponds to the standard hydrogen electrode (NHE).

In metal oxide and silicon based semiconductors, as is the case of the current study, a built-in electric field can even be formed at the surface without making contact with the electrolyte phase. When exposed to air, silicon based semiconductors dissociatively adsorb water molecules, leading to OH^- surface termination. Due to the symmetry broken at the surface, the OH^- groups form localized states whose energy lies within the semiconductor bandgap [19]. Fig. 1.4 shows the energy level for these surface states (SS), which are above the valence band maximum in a p-type semiconductor. Free holes from the bulk of the semiconductor will occupy this level giving way to ionized acceptors (N_A^-). The negatively charged acceptors form a negative space charge. This is what is called depletion condition in a p-type semiconductor. The charge transfer takes place until equilibration is reached. At this point, a dynamic equilibrium is accomplished, where no net electron/hole transport occurs. The Fermi level at the surface is then located somewhere halfway the Density of states (DOS) of the surface state [20].

The potential distribution and width (W) of the SCR depends on several parameters such as, the density of shallow acceptors N_A , the amount of charge transfer to the surface, the ionic concentration in the electrolyte, the presence of surface states and the amount of external potential applied to the photocathode. Several of these relevant parameters are shown in Fig. 1.5.

Quantitative expressions for the relationship of some of the parameters depicted in Fig. 1.5 are crucial in PEC research and are stated in Eqs. 1.6, 1.7 and 1.8 [20].

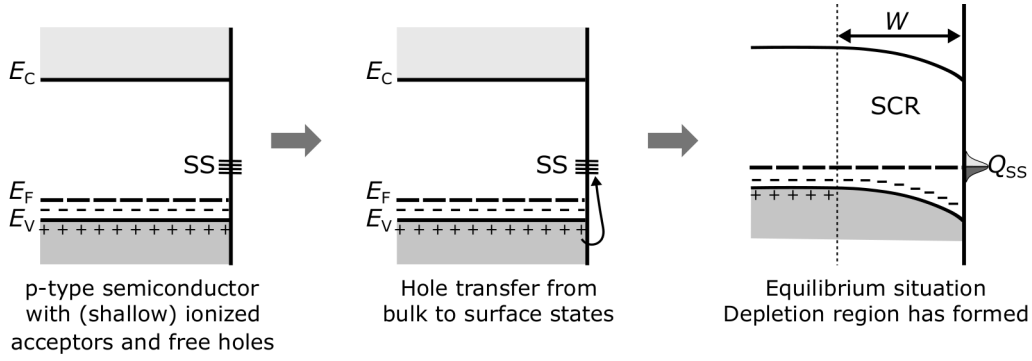


FIGURE 1.4: Formation of space charge region (SCR) at a metal oxide or silicon based semiconductor surface when exposed to air. SS represents the surface states. While DOS, the density of states of the SS. Adapted from Krol (2012) [20].

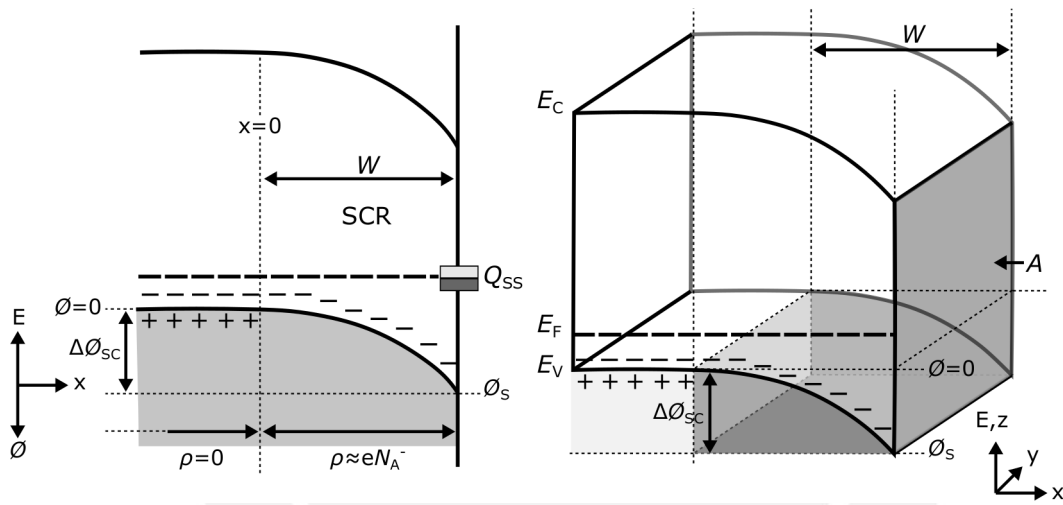


FIGURE 1.5: Band bending at the surface of a p-type semiconductor in depletion condition. The "-" markers just above the valence band represent the ionized acceptor species, whereas the "+" markers below the valence band level represent the free holes. The potential in the bulk of the semiconductor is chosen as zero. ρ represents the charge density. Parameters shown in Eqs. 1.6, 1.7 and 1.8, can be identified. Adapted from Krol (2012) [20].

$$Q_{SC} = \sqrt{2\epsilon_0\epsilon_r e N_A A^2 \left(\phi_{SC} - \frac{\kappa T}{e} \right)}. \quad (1.6)$$

$$W = \sqrt{\frac{2\epsilon_0\epsilon_r}{e N_A} \left(\phi_{SC} - \frac{\kappa T}{e} \right)}. \quad (1.7)$$

$$Q_{SC} = e N_A A W. \quad (1.8)$$

In equations 1.6, 1.7 and 1.8, Q_{SC} represents the amount of charge in the SCR, ϵ_0 and ϵ_r are the vacuum and relative permittivity, respectively. e is the electronic charge, A is the surface area of the semiconductor in contact with the electrolyte, ϕ_{SC} is the potential drop within the SCR, κ is the Boltzmann constant and T the temperature of the system.

The three-electrode setup of the PEC cell

Practical PEC devices need to manage optical, electronic, and catalytic functionalities, all at the same time. Fig. 1.6 depicts a simple PEC cell based on a three-electrode setup: the working electrode (WE), which is the light-absorbing material immersed in the liquid, can be a photocathode or a photoanode. The counter electrode (CE), driving the opposite half-reaction that is not light-activated, and the reference electrode (RE), used to accurately examine the potential of the WE during PEC test.

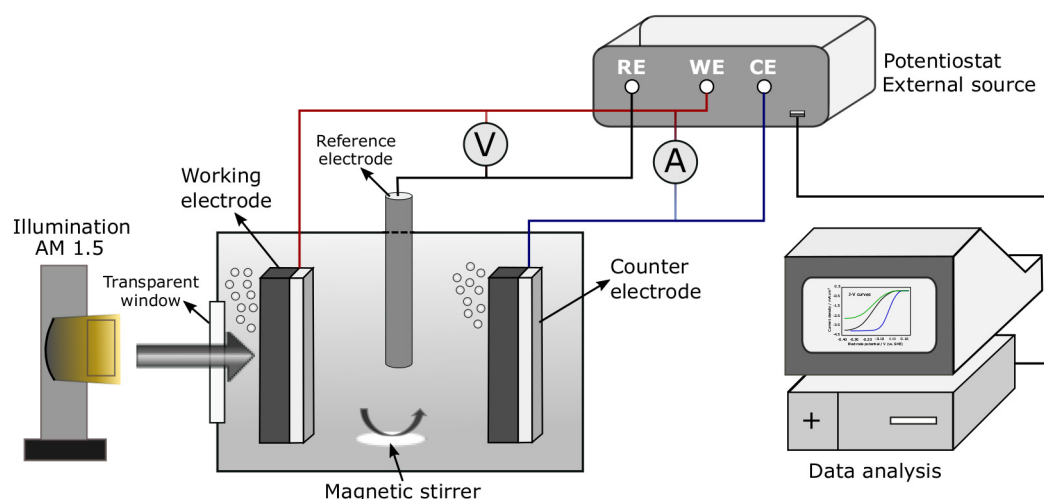


FIGURE 1.6: Experimental setup for measuring the performance of a photoelectrode under simulated sunlight AM 1.5. Basic components of a PEC cell are shown. Adapted from krol and Gimenez [12, 20].

In direct solar water splitting, i.e. bias-free water splitting, only the WE and CE form the PEC cell. However, in most of the cases, application of an external potential is necessary to drive water splitting. Thus, the RE becomes crucial to study the potential-dependent WE behavior. Additionally, to maintain the electrolyte concentration, minimize pH gradients, aid reactant/product mobility, and extract hydrogen and oxygen gases; electrolyte circulation, ionic exchange membranes and magnetic stirring are necessary.

As shown in Fig. 1.6, the WE and CE must be in electrical contact, then a conductive wire is connecting the two electrodes. The ionic species in the electrolyte must ensure the ionic conductivity between electrodes to close the electric circuit. The external source is represented by the potentiostat, which is used to control the sample's potential and to measure the current passing through the WE/CE connection. The WE study is performed under solar irradiation. Since places in the world have variable access to sunlight of different intensities, most PEC research laboratories are equipped with a solar simulator. Conventionally, an intensity of 1000 W/m^2 corresponding to 1 sun at air mass (AM) 1.5 is simulated.

1.1.2 Semiconducting photoelectrode materials and other issues in PEC research

In the last 40 years, many types of photo-semiconductors have been reported to act as efficient photocatalyst for hydrogen production via water splitting. The semiconductor's composition includes more than 130 materials, e.g. oxides, nitrides, carbides, sulfides and phosphides [21]. As key requirements for a semiconductor photoelectrode, efficient absorption of light, i.e. harvesting a wide range of the solar spectrum, and good charge transport, are found. Nevertheless, from the point of view of commercially viable devices, several determinants must be taken into account for the material choice. According to Keable and Holcroft [20], these include:

- High photocurrent leading to high efficiency
- High photon capture
- High photon-to-electron conversion efficiency
- Low electron-hole loss
- $1.6 \text{ eV} < \text{band gap} < 2.2 \text{ eV}$ matching hydrogen and oxygen evolution potentials to minimize bias
- Low cost of source material
- Abundant supply
- Durability in aqueous environment
- Resistance to high solar irradiance
- Resistance to high temperature
- Electrode structures supporting high current flows
- Avoidance of poisonous or contaminating materials

Other issues of relatively direct impact on PEC research are the hydrogen storage and the system costs. The problem of how to store and distribute hydrogen gas remains unsolved. Heavy steel cylinders are still used to contain the gas at a range of pressures which ensure that the volume is acceptably small. This fact generates constraints in the automotive industry for the transport of the overall weight of gas plus the containers. The relevant bench mark for competing with other energy sources is the Steam methane reforming (SMR), which is currently the cheapest source of hydrogen (\$1-5/kg). However, based on several assumptions, PEC hydrogen could cost less than \$3/kg, efficiently competing with SMR processes. The assumptions can be found elsewhere [22].

1.2 Thermodynamic for hydrogen production by PEC water-splitting

Fig. 1.7 depicts the energy diagram of a PEC cell in the dark and under illumination. In this example, an acidic electrolyte has been assumed to state the $\text{H}_2\text{O}/\text{H}_2$ redox couple the most active species and therefore, dominant of the electrochemical potential of the solution in the dark. The Fermi levels of the p-type semiconductor (WE) and the metal (CE) are electrically connected and adjust to a value close to E_{red} . The Fermi level maintains constant throughout the whole semiconductor sample. Under illumination, the equilibrium is disturbed by light excitation and the electron and hole densities increase to above their equilibrium value in the dark (n_0 and p_0 , respectively).

In general, electron and hole density (n and p) can be calculated from Eqs. 1.9 - 1.12 [23]:

$$n = \int_{E_C}^{\infty} N(E)f(E)dE. \quad (1.9) \quad n = N_C \exp\left(-\frac{E_C - E_F}{\kappa T}\right). \quad (1.10)$$

$$p = \int_{-\infty}^{E_V} N(E)(1 - f(E))dE. \quad (1.11) \quad p = N_V \exp\left(\frac{E_V - E_F}{\kappa T}\right). \quad (1.12)$$

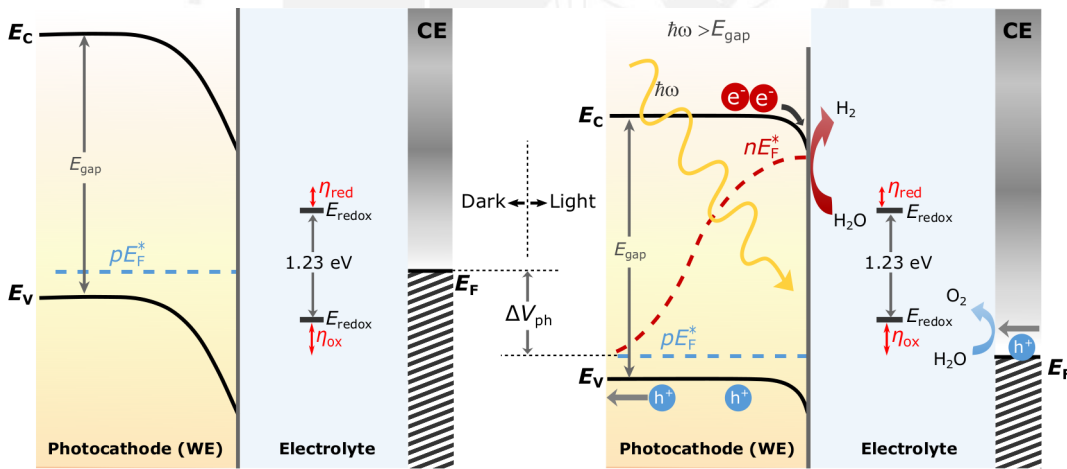


FIGURE 1.7: Band diagram for a PEC cell based on an p-type semiconducting photocathode that is electrically connected to a metal counter electrode. In equilibrium in the dark (left) and under illumination (right). Illumination decays the Fermi level and decreases the band bending. Adapted from Krol et al. [20].

In Eqs. 1.9 and 1.11, E_C is the energy at the bottom of the conduction band, E_V is the energy at the top of the valence band, $N(E)$ is the total density of energy states up to a certain energy level and $f(E)$ is the Fermi-dirac distribution which represents the probability of particles to occupy the available energy levels in the system. Expressions for $N(E)$ and $f(E)$ are shown in Fig. 1.8. Since the integral in Eqs. 1.9 and 1.11 cannot be solved analytically, the equations can only be solved assuming that $(E - E_F) \gg \kappa T$ and thus, Eqs. 1.10 and 1.12 are obtained. The last

assumption reflects the high probability of electrons to remain in the valence band due to the large gap in energy ($E_{\text{gap}} \approx 2 \text{ eV}$) between the valence and conduction bands. In Eqs. 1.10 and 1.12, N_C and N_V are the density of states around the bottom of the conduction band and the top of the valence band, respectively. n and p are represented in Fig. 1.8.

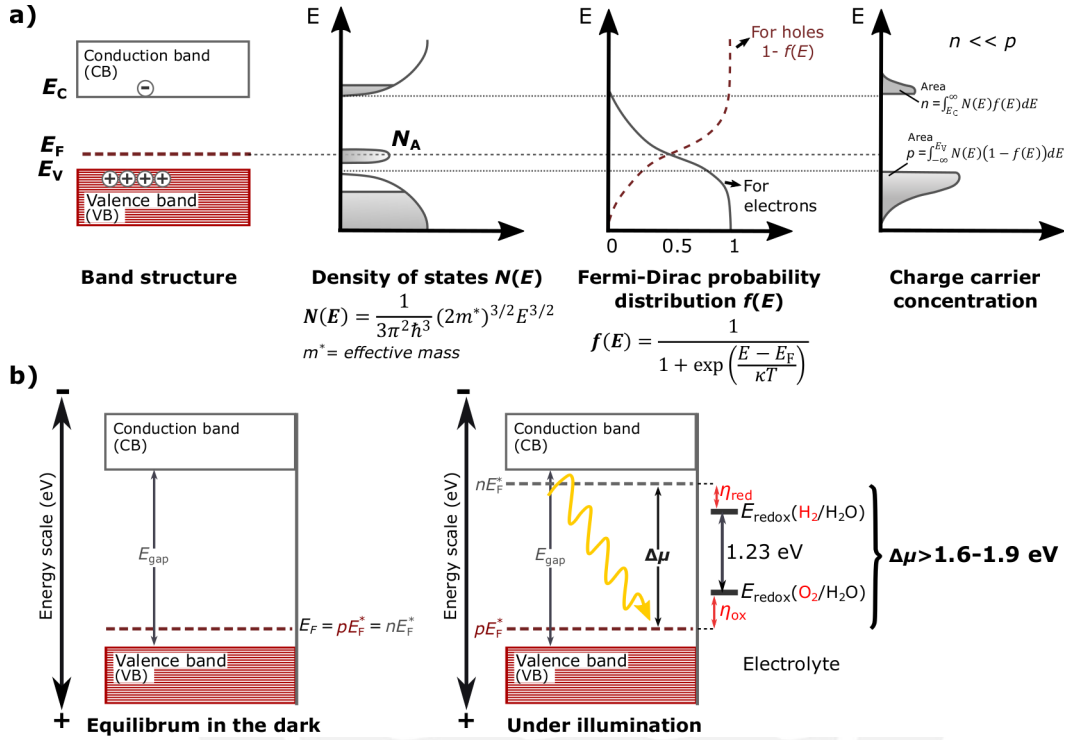


FIGURE 1.8: Band diagram, density of states, Fermi-Dirac distribution and charge carrier concentration for a p-type semiconductor (a). quasi-Fermi energy levels of electrons (nE_F^*) and holes (pE_F^*) have the same value at equilibrium conditions (dark). Under illumination, nE_F^* and pE_F^* change respect to the equilibrium case according to Eqs. 1.13 and 1.14 (b). As a result, thermodynamic requirements for water splitting is accomplished (b). Adapted from Peter et al. (2016) [23].

Upon light absorption, electron-hole pairs are created and the Fermi level decreases with the increment of the internal photovoltage (V_{ph}). The system is no longer in equilibrium, particularly in the SCR where the electrons and holes are efficiently separated. Therefore, a single Fermi level no longer determines the electron and hole density. Here, it is useful to introduce the concept of quasi-Fermi energy levels, one for electrons (nE_F^*) and another for holes (pE_F^*), both depicted in Fig. 1.8. These are a direct measure of the concentration of electrons and holes at a certain point x in the semiconductor, and are defined as [20]:

$$n = n_0 + \Delta n = N_C \exp - \left(\frac{E_C - nE_F^*}{\kappa T} \right). \quad (1.13)$$

$$p = p_0 + \Delta p = N_V \exp - \left(\frac{pE_F^* - E_V}{\kappa T} \right). \quad (1.14)$$

In Eqs. 1.13 and 1.14, Δn and Δp are the additional carriers created by illumination. For a p-type semiconductor, $n = n_0 + \Delta n \approx \Delta n$ and $p = p_0 + \Delta p \approx p_0$. So that, pE_F^* remains horizontal, whereas nE_F^* departs from the bulk Fermi level in the active SCR, as shown in Fig. 1.7.

The quasi-Fermi levels play an important role in processes at the semiconductor-electrolyte interface. Thermodynamic requirements to perform the whole water splitting redox reaction are stated as following: the nE_F^* needs to be located above the reduction potential of water ($\text{H}_2\text{O}/\text{H}_2$) to allow electron transfer to the solution and drive the HER. While the pE_F^* needs to be located below the oxidation potential of water ($\text{H}_2\text{O}/\text{O}_2$) to allow hole transfer to the solution and conducts the OER. Thus, the relative position of the quasi-Fermi levels with respect to the redox couples in solution yields the thermodynamic force which drives the electrochemical reaction.

The thermodynamic force generated upon sunlight absorption must overcome the thermodynamic energy difference between $\text{H}_2\text{O}/\text{H}_2$ and $\text{H}_2\text{O}/\text{O}_2$ redox couples, i.e. 1.23 eV, plus the kinetic electrochemical overpotentials for the reduction and oxidation reactions, η_{red} and η_{ox} , respectively. For the classic PEC water splitting situation, this amounts to around 1.6–1.9 eV depending on the photocatalytic materials employed and the operating current density, as will be discussed in the next section [12]. This thermodynamic condition is depicted in Fig. 1.8.

So far, attention has been focused on the p-type semiconductor-electrolyte interface under depletion condition. However, upon application of a certain bias, flat band, accumulation and inversion condition can occur in the immersed WE during PEC test. Some of these conditions are shown in Fig. 1.9.

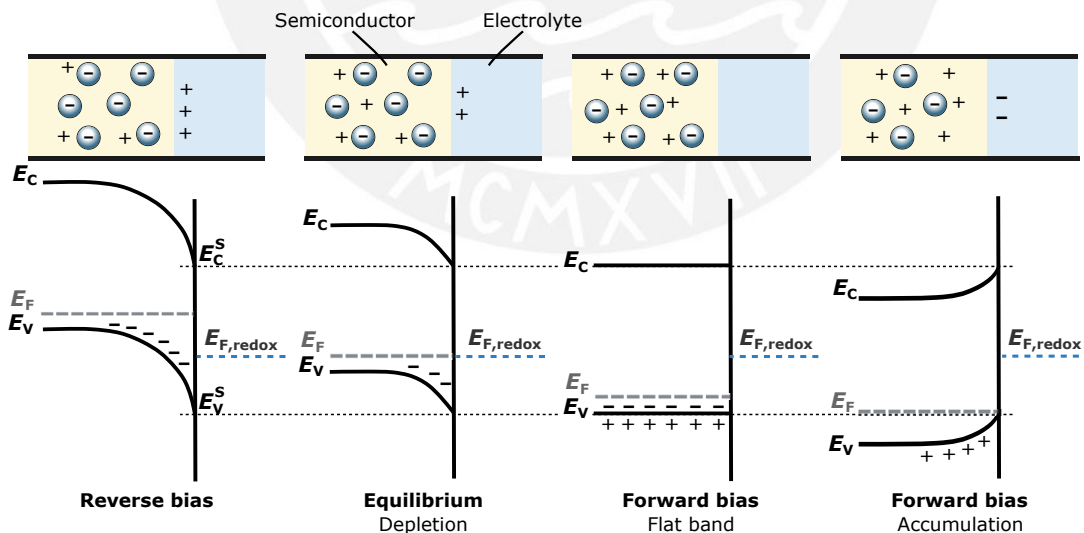


FIGURE 1.9: Diode behaviour of the p-type semiconductor-electrolyte interface in dark conditions. The junction blocks the electron flow from left to right under reverse bias. While electrons can pass from right to the left as forward bias reduces the band bending. As bias is applied, depletion, flat band and accumulation conditions are formed at the interface.

In Fig. 1.9, when negative potential is applied, i.e. at reverse bias, the Fermi level in the semiconductor moves upward, relative to the electrolyte redox level. Thus, a

electron flow from the semiconductor to the redox system becomes thermodynamically possible [12]. The rate of electron injection depends on the difference between $E_{F,\text{redox}}$ and E_V^S . This energy barrier is similar to the Schottky-barrier formed at metal-semiconductor junctions and limits the current to a small constant value known as the reverse saturation current. In fact, negligible values of saturation currents are found flowing at semiconductor photoelectrodes in the dark, often around 10 nA/cm^2 . This dark current is mainly carried by minority carriers at reverse bias condition, i.e. electrons in a p-type semiconductor. On the other hand, when positive bias is applied to the WE, i.e. at forward bias condition, the E_F in the semiconductor moves downward, relative to the electrolyte redox level. Thus, holes flow from the semiconductor to the redox system becomes thermodynamically possible. The application of positive potential drives hole accumulation at the semiconductor surface and the current will increase as the potential in the SCR is made more positive. Now, the electrode behaves more like a metal. This metal behavior is achieved beyond the flat band potential condition, at which potential at the surface is zero.

1.3 Kinetic considerations for hydrogen production by PEC water splitting

So far, it has been assumed that the electron transfer from the semiconductor to the electrolyte occurred if the the electron in the solid exceeds the reduction energy of species in solution plus the respective overpotential [20]. The same as for the hole transfer, holes in the solid must exceed the oxidation energy of species in solution plus the overpotential to conduct an oxidation reaction. Unfortunately, this simple scheme does not hold for large energy differences. Furthermore, no information is given for the kinetic of charge transfer in the process [20]. Several theories of electron transfer taking place at the semiconductor-electrolyte interface have been developed since the late 1950s. For example, Marcus [24, 25] and Gerischer [26] models are based on classical physics; while Levich, Dogonadze and Kuznetsov [23], are based on Quantum-chemical extensions of Marcus theory.

1.3.1 The fluctuating energy level of ions in solution

A common element in all versions of electron charge transfer theories is the existence of a fluctuating energy level of ions in the electrolyte. In polar solvents, such as water, each ion is surrounded by a cloud of solvent molecules forming the so-called *inner sphere*. The solvent molecules are oriented with their dipole moment to compensate the ion neat charge. Additionally, the ion also exhibits Coulomb interactions with further away polar solvent molecules, extended beyond the inner sphere. These molecules form what is called the *outer sphere*. The energy level of the central ion will fluctuate due to thermal motions of ions in the solution. Moreover, after reduction or oxidation of the ion, the surrounding molecules of the inner and outer spheres

will rearrange to compensate the different charge of the ion. The electrostatic energy required for this reorganization is given by 2λ , where λ is called reorganization energy [20]. The energy diagram of a redox system is depicted in Fig. 1.10. This results to be similar to that of a solid- the electronic energy E°_{red} is a ionization energy I^0 , whereas E°_{ox} corresponds to the electron affinity A^0 . The E°_{redox} is the standard redox potential of the species involved, as for example 0 V vs NHE for the H^+/H_2 redox couple. D_{red} represents the density of states of the reduced species (H_2), while D_{ox} , the density of states of the oxidized species (H^+). Expressions for D_{red} and D_{ox} are found in Eqs. 1.15 and 1.16 [23].

$$D_{\text{red}} = c_{\text{red}} \times W_{\text{red}}(E). \quad (1.15) \quad D_{\text{ox}} = c_{\text{ox}} \times W_{\text{ox}}(E). \quad (1.16)$$

In Eqs. 1.15 and 1.16, c_{red} and c_{ox} are the concentration of the reduced and oxidized species of the redox system, respectively. W_{red} and W_{ox} describes the fluctuation of the energy level of the reduced and oxidized species. These fluctuations reflect the chance for the reduced or oxidized species to have a certain energy E and are described by Eqs. 1.17 and 1.18 [20]:

$$W_{\text{red}}(E) = \frac{1}{\sqrt{4\pi\kappa T}} \text{Exp} \left(\frac{-(E - E^\circ_{\text{redox}} - \lambda)^2}{4\pi\kappa T} \right). \quad (1.17)$$

$$W_{\text{ox}}(E) = \frac{1}{\sqrt{4\pi\kappa T}} \text{Exp} \left(\frac{-(E - E^\circ_{\text{redox}} + \lambda)^2}{4\pi\kappa T} \right). \quad (1.18)$$

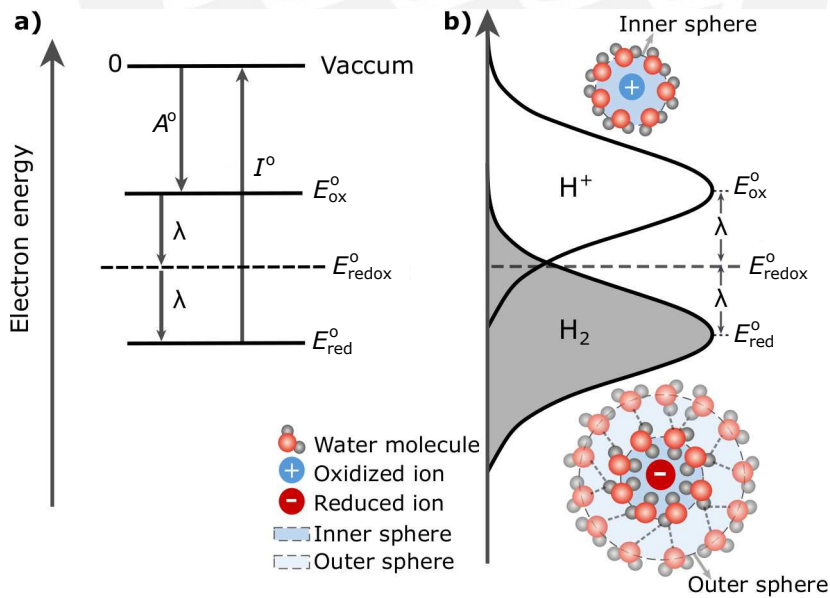


FIGURE 1.10: Electron energies of H^+/H_2 redox system (a) and corresponding distribution functions for E°_{red} (D_{red}) and E°_{ox} (D_{ox}) (b). λ is the reorganization energy for H^+ and H_2 . For equal concentration of H^+ and H_2 , λ is the same for both species. Inner and outer spheres are depicted in (b). Adapted from Peter (2016) [23].

1.3.2 Interfacial electron transfer: semiconductors vs metals

For semiconductors, charge transfer takes place via three different pathways: the bottom of the conduction band (E_C^S), the top of the valence band (E_V^S), and in certain cases, via surface states (SS). Whether the corresponding current is possible depends on several factors, such as the position of the energy band edges relative to the redox species in solution, the occupation of the energy states by electrons, and the density of energy states (DOS) on both sides of the interface. The overlap between energy states is usually limited to a small range of energy levels, as it is shown in Fig. 1.11 for the case of p-type semiconductor. So the charge transfer mainly takes part within $1 \kappa T$ at the edge of the conduction or valence band. Greater overlapping of energy states occurs for the case of metal electrodes, which exhibit high density of states near their Fermi levels. Actually, density of states in metals can be 3–4 orders of magnitude higher than N_C and N_V in semiconductors. The last phenomenon is reflected in higher current densities obtained from metal electrodes at equilibrium conditions, compared with those obtained from semiconductors [20].

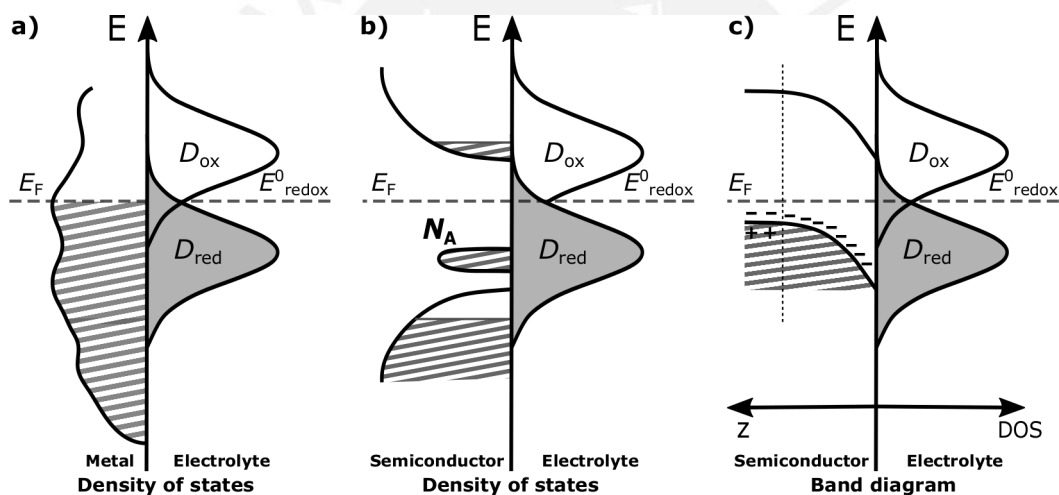


FIGURE 1.11: Electron energies in solid electrodes in contact with a redox system vs density of states of ions in solution: for metal electrode (a) and for p-type semiconductor electrode (b). Energy level model of electron transfer from a p-type semiconductor to oxidized species in solution under equilibrium condition. No overlapping is observed between the DOS in the valence band and D_{ox} (c).

Fig. 1.12 depicts the case of photogenerated electrons being transferred from the conduction band to the oxidized redox species in solution, i.e. $E_C \rightarrow D_{ox}$. This case is only significant in p-type semiconductors where electrons, acting as minority carriers, significantly increase under illumination. Nevertheless, similar pictures of electron transfer can be made for other pathways: $D_{red} \rightarrow E_C$, $E_V \rightarrow D_{ox}$ and $D_{red} \rightarrow E_V$ [27].

As shown in Fig. 1.12, the probability of electron transfer decreases as E_C^S is too far away from the E_{ox}^0 . This behavior is notably different for the case of metal electrodes, which exhibit a continuous increase in current as potential is applied. In fact, the charge transfer process in semiconductors takes place iso-energetically, via a tunneling mechanism. This means that the energetic level of the electron or hole in the

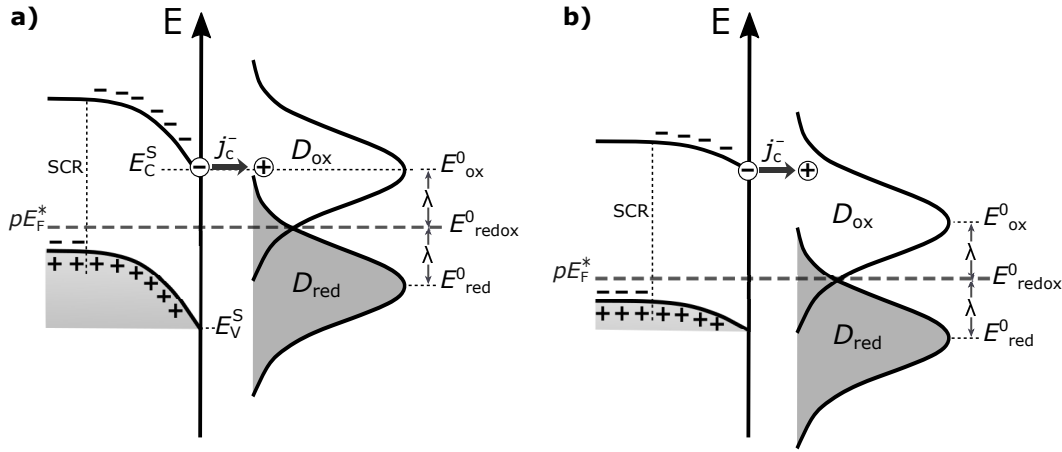


FIGURE 1.12: Energy level model of electron transfer from the conduction band in a p-type semiconductor to a redox species in solution under illumination. A large overlap between DOS of the oxidized species D_{ox} and the energy of the electron in the conduction band gives high currents (a) compared with currents obtained with smaller overlapping (b). nE_F^* is not depicted for simplification. Adapted from Krol et al (2012) [20].

solid must be, at certain moment in time, equal to the fluctuating energy level of the ion species in the electrolyte. This implies that the charge transfer occurs horizontally, and the charge does not lose any energy during the process. Moreover, the energy of the ion in solution remains constant during the transfer. The latter phenomenon is assumed since electron transfer processes occur on a much faster time scale than the ionic reorganization around the central ion, what is stated as Frank–Condon principle. The transfer rate is then proportional to the density of the species in the electrolyte (D_{red} , D_{ox}), the ion concentration (c_{red} , c_{ox}), and the quantum-mechanical tunneling coefficient- i.e. K_C^- , K_C^+ , K_V^- and K_V^+ . Eqs. 1.19 - 1.22 show the cathodic (-) and anodic (+) conduction and valence band currents related to the four possible pathways defined for charge transfer [27].

$$E_C \rightarrow D_{ox} \quad (1.19) \quad E_V \rightarrow D_{ox} \quad (1.20)$$

$$j_C^- = eK_C^- n_S c_{ox} W_{ox} (E_C^S) \quad j_V^- = eK_V^- N_V c_{ox} W_{ox} (E_V^S)$$

$$D_{red} \rightarrow E_C \quad (1.21) \quad D_{red} \rightarrow E_V \quad (1.22)$$

$$j_C^+ = eK_C^+ N_C c_{red} W_{red} (E_C^S) \quad j_V^+ = eK_V^+ p_S c_{red} W_{red} (E_V^S)$$

In Eqs. 1.19 - 1.22, N_C and N_V are the effective density of states in the semiconductor, and n_S and p_S are the surface concentration of free electrons and holes in the conduction and valence band, respectively. Expressions for N_C , N_V , n_S and p_S are shown in Fig. 1.8. Depending on the standard potential of a redox couple, if this is rather negative or positive, the E_F of the redox system- i.e. $E_{F, redox}$ - will occur fairly close to the conduction E_C^S or valence band E_V^S , respectively. In that sense, the major part of the current will come from the band that is closer to the $E_{F, redox}$. As seen in

Fig. 1.11, since the overlapping of energy states in both sides of the semiconductor-electrolyte interface spreads over a small interval of energies, the electron transfer occurs mainly in the vicinity of the E_C^S . And Eq. 1.19 can be re-written by using Eq. 1.18, replacing E by E_C^S as 1.23:

$$j_C^- = eK_C^- n_{Sc_{ox}} \frac{1}{\sqrt{4\pi\kappa T}} \text{Exp} \left(\frac{-(E_C^S - E_{\text{redox}}^o + \lambda)^2}{4\pi\kappa T} \right). \quad (1.23)$$

Eq. 1.23 shows the case of a charge transfer taking place via the lower edge of the E_C . As the position of the energy bands remains unchanged upon varying the semiconductor electrode potential, the energy difference $E_C^S - E_{\text{redox}}^o$, related to the reaction rate constant, remains at the same value. This means that the rate constant for reactions at semiconductor electrodes is constant. In this case, the equilibrium is reached by changing the carrier density at the surface until the E_F of the system becomes equal to E_{redox}^o . On the other hand, in the case of metal electrodes, the electron transfer occurs around the E_F , so that, E_F replaces the E_C^S in Eq. 1.23. Thus, by applying an overvoltage ($\eta = (E_F - E_{\text{redox}}^o)/e$), E_F moves and the rate constant of the reaction varies several orders of magnitude. This analysis supports the continuous increase in current with applied potential observed in metal electrodes [23].

1.4 The study of the electrolyte interface

1.4.1 The steady state regime

The study of the water splitting process involves electrochemical redox reactions taking place in a three-electrode setup (Fig. 1.6). For a particular photoactive material, acting as WE, application of certain potential range is necessary to analyze changes at its surface. These changes are related to the development of the water splitting reactions at the WE and CE interfaces with the electrolyte. During PEC tests, when the WE is immersed in aqueous solution, an equilibrium potential (E_{eq}) is measured with respect to a RE, which is usually the NHE (0 V for the H^+/H_2 redox couple). The Nernst equation (Eq. 1.24) establishes how the equilibrium potential of the electrode is changing in dependence of environmental parameters like concentration, partial pressure and temperature. Upon application of a potential E , different from E_{eq} , an electrochemical reaction can occur at the WE surface. This reaction consumes the ions located on the electrode surface, which have to be replenish before further reaction can occur. If the mass transport of ions towards the surface is slow, only a small current can be expected, while for a fast mass transport, a higher current occurs.

$$E_{\text{eq}} = E_{\text{NHE}}^o + \frac{RT}{n'F} \ln \frac{aOx_{\text{elec}}}{aRed_{\text{elec}}}. \quad (1.24)$$

In Eq. 1.24, R is the universal gas constant (8.314 J/mol·K), T is the temperature of the system in K, n' is the number of electrons transferred, F is the Faraday constant (96500 C). aOx_{elec} and $aRed_{\text{elec}}$ are the activities of the oxidized and reduced species,

respectively, where a stands for the activity coefficient. Activities describe the effective concentration of the species considering the solvent-solvent, solvent-solute, and solute-solute interactions. As solution gets more diluted, the activity coefficients are close to unity. Thus, activities can be approximated to concentrations, simplifying calculations.

In the general case, electrochemical reaction occurs at finite velocity. The same as for the mass transport, from the bulk of the electrolyte towards the electrode. Considering both velocities finite, two phenomena are developed in the following order upon application of an external potential E :

1. The WE and CE surface concentrations change slowly up to reach a new equilibrium state, which corresponds to the potential applied, according to Eq. 1.24.
2. The transport velocity (v_{trans}) of the ionic species in solution changes up to reach a constant value, equal to the electrolysis velocity (v_{elec}) at the electrode surface. This condition can be written as $v_{\text{elec}}=v_{\text{trans}}$.

After these processes, an stationary regime is observed in the electrolysis. By this regime, the formation or disappearance of the substances in the electrode is exactly compensated by diffusion. Therefore, the concentration of the electrolyzed species at the electrode surface is constant for each applied voltage during the electrochemical test. Experimental analysis demonstrate that such stationary state can be achieved in a fairly short time, by making the concentration of electrolyzed species time-independent. This is accomplished using an excess of the electrolyte concentration, which makes the amount of the electrolyzed substance negligible at the WE surface, compared with the total amount of this substance contained in the whole cell during the test time. Values of 1 M concentration are usually used for the electroactive species to accomplish the stationary state regime. In addition, the requirement of high conductivity for the solution is fulfilled with electrolyte concentrations around 1 M, that is equivalent to 10^{20} ions/cm³ (1 mol/L).

1.4.2 Current-Potential (I-V) curves

To provide that PEC operation is stable during electrochemical tests, a truly stationary value of current for each applied potential must be recorded. In that sense, the study of the electron transfer at the semiconductor photoelectrode is exclusively determined by the particular properties of the semiconductor-electrolyte interface, without having influence of diffusion limitations by mass transport. This interface would compromise the SCR from the side of the semiconductor, until the diffuse layer (see Fig. 1.13) from the side of the electrolyte. The diffuse layer becomes constant under stationary state conditions in the presence of high concentration of electrolytes.

The PEC reaction occurred under illumination is observed in Fig. 1.14, when the energy of the exposed radiation $\hbar\omega$ is larger than the E_{gap} of the semiconductor. The main point in this reaction is generation of minority carriers by light absorption, that

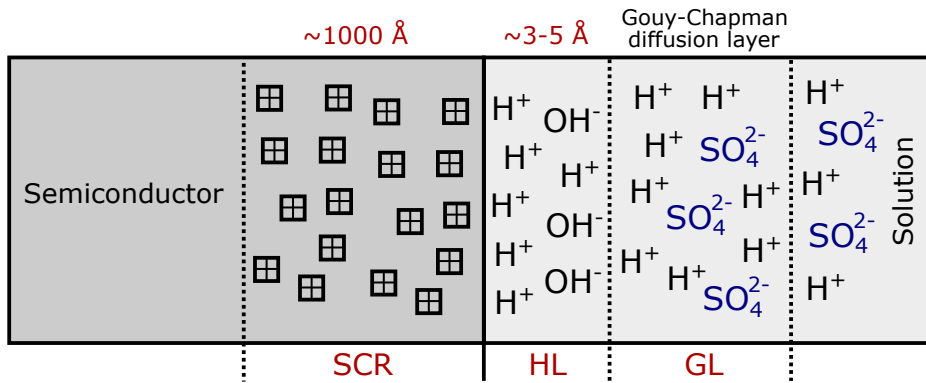


FIGURE 1.13: The three double layers at the semiconductor-electrolyte interface on the example of aqueous solution of H_2SO_4 . SCR is the space charge layer, HL is the Helmholtz layer and GL, the Gouy layer. All of them form the semiconductor-electrolyte interface

is, electrons in a p-type semiconductor, and holes in an n-type semiconductor. In this case, the current density-potential (J-V) curve is depicted for a p-type semiconductor. Due to the electric field in the SCR, minority carriers are drifting from the bulk of the semiconductor towards the electrolyte. This phenomenon takes place under depletion condition, promoting PEC reaction at the surface of the semiconductor.

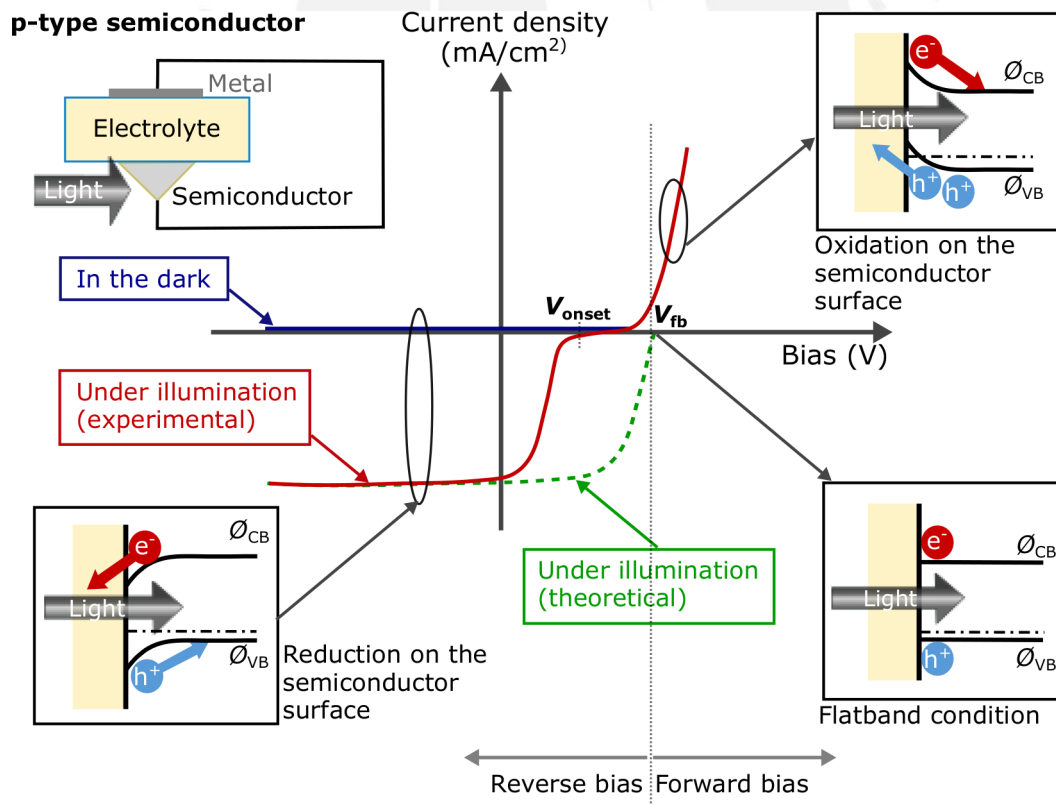


FIGURE 1.14: Schematic J-V diagram for a p-type semiconductor-electrolyte-metal configuration. Photocurrent is observed when the potential is applied in the reverse bias condition. Application of high forward bias, may conduct to oxidation at the semiconductor surface. The flat band potential does not usually coincide with the onset potential. Adapted from Fujii (2016) [17].

Without illumination, current is not observed at the reverse bias region. Nevertheless, photocurrent is observed in this region when illumination is applied and the energy of the photons exceed the semiconductor E_{gap} . Band diagrams corresponding to the applied bias are also illustrated in Fig. 1.14. Upon bias application, practically all the potential drop takes place inside the SCR of the semiconductor, and very little in the Helmholtz layer, i.e. on the solution side. This means that the band bending inside the semiconductor changes with the potential applied, while the energy of the conduction and valence band edges remains the same at the solid surface. The last effect is generally observed in aqueous electrolytes, where intermolecular forces between the adsorbed dipole molecules and the electrode surface are strong enough and do not change with the applied bias. As a consequence, band bending in the depletion layer changes with the applied bias, and thus, the current density becomes also dependant of the potential applied.

The flat band condition, where the band edges are flat, corresponds to the potential at which the current density is zero. The flat band potential (V_{fb}) expresses the relative position of the conduction/valence band edges with respect to the redox potential of the electrolyte, and denotes the position of the Fermi level of the semiconductor respect to the potential of the RE. It is expected that the V_{fb} value lies at the potential at which photocurrent is observed, known as the onset potential (V_{onset}). However, the potential applied until photocurrent appears is usually tenths of volts more negative than the real V_{fb} , for the case of p-type semiconductors. This might be due to electron-hole recombination in the SCR, electron trapping at surface states, or electron accumulation at the surface due to poor transfer kinetics. The most often used method to determine the V_{fb} , is the Mott-Schottky analysis as will be discussed in following sections.

1.4.3 The dynamic regime

So far, the discussion has been centered on the steady state conditions of the semiconductor electrolyte interface respect to carrier generation and collection. Nevertheless, a wealth of information can be obtained from the steady-state system perturbation-response, what is known as dynamic regime [18]. With Electrochemical Impedance Spectroscopy (IS), the analysis of electrical properties of interfaces is achieved by applying a small amplitude AC potential perturbation (\tilde{V}) around a constant bias potential. The resulting oscillating current (\tilde{j}) is then measured, from which an impedance value can be calculated by $Z(\omega) = \tilde{V}/\tilde{j}$. Since the system response is not instantaneous, a time delay exists between the application of the voltage and the current response. So that the $Z(\omega)$ value includes an imaginary component. This condition can be observed in Fig. 1.15. Typically, the frequency of the AC signal is swept from MHz to mHz to obtain the impedance spectra Z'' vs. Z' , termed "Nyquist plot". Therefore, different processes occurring in the samples, like transport or recombination, can be analyzed independently according to their different characteristic

times, i.e. frequencies, by using the appropriate equivalent circuit [28]. Example of more common equivalent circuits are shown in Fig. 1.16.

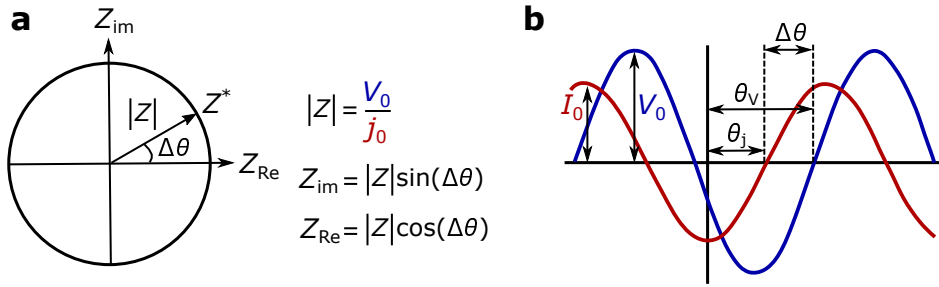


FIGURE 1.15: Representation of the complex impedance (a). Sinusoidal voltage \tilde{V} and current \tilde{j} from which the complex impedance is calculated (b). Adapted from [12].

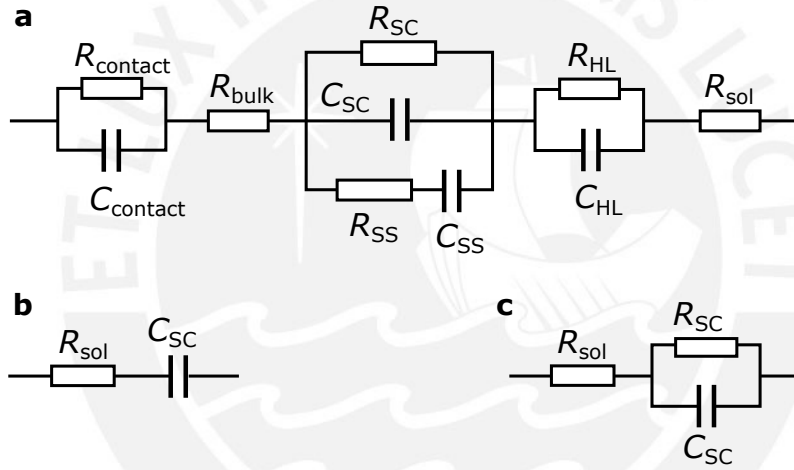


FIGURE 1.16: Equivalent circuits for photoelectrochemical cells. Extensive circuit containing contributions from the semiconductor/back contact interface (R_{contact} , C_{contact}), the semiconductor bulk resistance (R_{bulk}), the space charge region (R_{SC} , C_{SC}), the surface states (R_{SS} , C_{SS}), the Helmholtz layer (R_{HL} , C_{HL}) and the electrolyte resistance (R_{sol}) (a). The most simple equivalent circuit in which only the space charge region capacitance and the electrolyte resistance take place (b). The most common circuit used in practice for photoelectrodes (c). Adapted from [12].

IS constitutes a reliable tool to analyze indirect charge transfer mechanisms taking place via SS, that was mentioned in Sec. 1.3.2. Determination of SS density can be achieved by monitoring the surface state chemical capacitance C_{μ}^{SS} as a function of the applied bias, i.e. Fermi level (E_{F}). In dark condition, majority carriers are in equilibrium with the transport band (valence band for a p-type semiconductor) and this capacitance is called the equilibrium chemical capacitance of surface states $C_{\mu\text{eq}}^{\text{SS}}$ [12]. The density of SS (N_{SS}) can be obtained by measuring an impedance Nyquist plot spectrum and extracting the value of $C_{\mu\text{eq}}^{\text{SS}}$ using a suitable equivalent circuit. Thus, $C_{\mu\text{eq}}^{\text{SS}}$ is defined according to Eq. 1.25, where A is the surface area of the electrode in contact with the electrolyte, and e is the electronic charge.

$$C_{\mu_{\text{eq}}}^{\text{SS}} = AeN_{\text{SS}}(E_{\text{F}}). \quad (1.25)$$

1.5 Developing photopotential harvesting the solar spectrum

Many semiconductor materials have been proposed as potential candidates to split water by photocatalysis. Limitations of these photocatalytic materials include chemical stability in aqueous solutions, corrosion resistance and suitable capability to absorb light from the solar spectrum to achieve a self-sustained PEC reaction [20, 29]. Large bandgap materials only absorb a portion of the visible spectrum and ultraviolet light, covering merely $\sim 5\%$ of photons of the solar spectrum [30]. Additionally, the optical bandgap energy (E_{gap}) of the material must be significantly larger than the thermodynamically required 1.23 eV to split water, i.e. approximately 1.9 eV [31], to overcome the necessary overpotential to drive the reaction. Furthermore, an amount of work must be done to extract the photogenerated charge carriers from the semiconductor to conduct the full water splitting reaction. This extra work represents an entropic energy loss (U_{loss}) in the whole system reaction [12]. Therefore, for a single semiconductor material, the external available free energy $\Delta\mu_{\text{ex}}$ to conduct water splitting is considerably lower than the E_{gap} . There are some approximations about U_{loss} values based on terrestrial solar intensities and the assumption that every single absorbed photon generates one excited electron-hole pair. In that sense, an U_{loss} of about $0.25 E_{\text{gap}}$ is considered a reasonable assumption [32]. Thus, $\Delta\mu_{\text{ex}} \approx 0.75 E_{\text{gap}}$ implies a minimum E_{gap} of 2.2 eV to accomplish unassisted water splitting with a single semiconductor junction [33]. The ideal single junction configuration would harvest the portion of the solar spectrum with photon energies $E_{\text{photon}} > 2.2 \text{ eV}$, as depicted in Fig. 1.17. Nevertheless, using an integrated tandem approach, in which two or more semiconductor layers are placed one on top of another in a monolithic single device, the U_{loss} has been estimated to be around 1.4 eV, for two semiconductor junctions [34–37]. Consequently, a minimum E_{gap} of around 2.7 eV would be required to achieve the unassisted water splitting process. The sun spectrum for $E_{\text{photon}} > 2.7 \text{ eV}$ is also highlighted in Fig. 1.17. Due to the shorter usable spectral region, the photocurrent is limited, compromising the solar-to-hydrogen conversion (STH) efficiency, i.e. in a tandem device the photocurrent of the system is determined by the lowest photocurrent absorber layer. Thus, developing enough external available free energy for PEC hydrogen production, while harvesting a significant amount of energy from the solar spectrum, is one of the main challenges in the field of materials for solar light absorption based hydrogen production.

1.6 a-SiC:H(p) as photocathode for PEC water-splitting

Amorphous silicon carbide is a promising material for photoassisted electrolysis applications due to its chemical stability, high corrosion resistance, earth-abundant

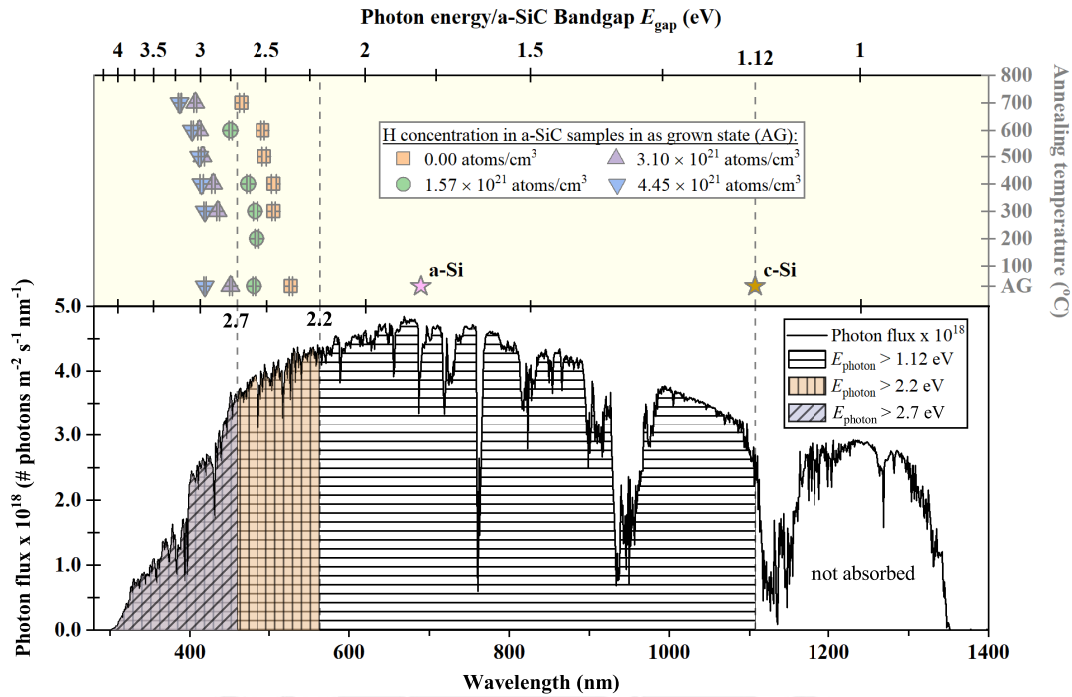


FIGURE 1.17: The AM 1.5 Global Tilt spectrum shown as solar photon flux as a function of wavelength and photon energy [ASTM]. The portion of the solar spectrum harvested by various band-gap energy semiconductors are indicated. Bandgap engineering of a-SiC:H semiconductor films varying the hydrogen concentration and upon different annealing steps was performed in this study to obtain an optimal bandgap value for PEC water splitting applications. The results of this work are summarized on the top of the solar spectrum image.

composition, and production technology scalability [38–40]. Doping and bandgap engineering work has resulted in an energy bandgap range between 1.8 and 3.0 eV for a-SiC:H thin films [41–43]. This is achieved by varying the carbon content in a-Si_{1-x}C_x:H systems. The incorporation of carbon in a-Si:H films to obtain a-Si_{1-x}C_x:H enables to overcome the inability of Si narrow bandgaps (e.g. c-Si $E_{\text{gap}} = 1.1$ eV and a-Si:H $E_{\text{gap}} = 1.8$ eV) [44–48] to fulfill the minimum 2.2 eV of E_{gap} required for water splitting. Although a suitable E_{gap} for solar water splitting, between 2.2 and 2.6 eV, can be achieved with this material, an increment of carbon concentration in these systems leads to the enhancement of disorder related localized states near the semiconductor band-edge [49], whilst for low carbon concentrations the chemical stability is compromised. Typically the dilution of hydrogen in amorphous Si and amorphous SiC largely increases the bandgap making it difficult to tune it for PEC applications. Additionally, there is no consensus on how to determine the optical bandgap of amorphous materials. This is mainly due to the disorder related localized states near band-edges known as Urbach tails, which are more pronounced in amorphous semiconductors than in their crystalline counterparts, biasing the bandgap determination [49].

Additionally, the carbon incorporation leads to an enhancement of the corrosion resistance properties in aqueous media. It has been theoretically estimated that a PEC

device with an a-Si_{0.9}C_{0.1}:H absorption layer exhibiting 2.0 eV of energy bandgap, can generate a photocurrent density J_{ph} of 15 mA/cm² (solar-to-hydrogen conversion efficiency ~18 %) when submitted to an Air mass (AM) 1.5 solar spectrum [50]. Research on single thin film photoactive materials does not typically consider the role of the silicon substrate in the photoelectrochemical performance [51]. In this sense, the photoelectrode is a system formed by a p-p, n-n or n-p structure, which depending on the depth of the space charge region may have an important impact on the photoelectrode performance.

PEC performance of a-SiC:H is often limited by its non-ideal energy valence band-edge alignment to the H₂O/O₂ redox potential, thus limiting the oxygen evolution reaction (OER) and the whole water splitting process [29]. To overcome this downside, an external bias needs to be applied, contributing to counteract the overpotential required to trigger the direct water splitting reaction. The external bias also contributes to reduce overpotentials due to the presence of a surface SiO₂ barrier layer and compensates interface charge carriers recombination as well.

Previous studies have demonstrated that by removing the SiO₂ native layer from a-SiC:H(i) surface, J_{ph} values over 6 mA/cm² can be achieved at a potential of -1.4 V vs. Ag/AgCl in contrast to values lower than < 4 mA/cm² obtained without the oxide removal [39]. In fact, the existence of SS originated from the hydroxyl group termination on the oxide surface, form an electronic state that is located within the semiconductor bandgap [52]. The theory that such states act as recombination centers for minority photo carriers, fits quite well with the assumption that surface recombination competes with charge transfer from the semiconductor band towards the electrolyte. Moreover, as was mentioned in previous section, the density and energetic position of SS, can trigger another favorable pathway for indirect charge transfer to the solution, competing with the undesirable recombination mechanism. Knowledge in this field is limited to full-drift diffusion simulations in steady-state and dynamic regimes for photo-anodic currents in crystalline materials [53, 54].

1.7 Amorphous SiC

Among the compounds found in the Si-C system at equilibrium conditions, Silicon carbide is the only one that possess stability at atmospheric pressure [55]. Since the possibility of doping hydrogenated amorphous silicon carbide was discovered in 1975 [56], new technological perspectives have arisen around this material, supported by fundamental studies. The worldwide efforts to understand the properties of hydrogenated SiC and its alloys have led to discover its excellent mechanical, electrical, optical and chemical properties to be used in technological fields requiring extreme conditions [57]. Silicon carbide as semiconductor has gained an enormous demand in p-i-n (P-type-intrinsic-N-type semiconductor) solar cells, and the optimization of its optoelectronic properties continues being studied for this application [58–60]. Furthermore, a-SiC can be found as anti-reflection coating [61], in microelectronics

[62, 63], as protective coating against corrosion [64, 65], moisture [66, 67], abrasion [68, 69] and etching [70, 71]. Moreover, a-SiC is also used in bio-molecular [72] and medical applications [73]. One of the major issues in the study of amorphous silicon carbide alloys is the non-well-defined bulk properties they exhibit, compare with those for crystalline SiC alloys [57]. a-SiC bulk properties, such as mechanical, structural, optical and electrical properties, are strongly dependent on the methods and preparation conditions used during fabrication. This causes difficulties to compare findings related to a-SiC between different research groups.

1.7.1 Amorphous structure of SiC

The amorphous silicon carbide network remains a matter of discussion concerning the physical basic understandings. Unlike amorphous silicon networks exhibiting a fully tetrahedral coordination [74], amorphous silicon carbide networks exhibit pseudo-coordination geometries coming from two different atoms [75]. The understanding of pseudo-coordination phenomenon lies in the increasing difference in bond lengths that leads to a chemical disorder where pseudo-hybridization states are found. Therefore, a-SiC network becomes a more complex system than the one for a-Si. Table 1.1 summarizes the SiC relevant bonds and their respective bond lengths that can be found in a-SiC matrix.

TABLE 1.1: SiC relevant bonds and bond lengths [75].

| Bond | Length (10^{-1} nm) | Bond | Length (10^{-1} nm) |
|-------------------|---------------------------|--------------------|---------------------------|
| C-C | 1.54 | C-Si | 1.87 |
| C=C | 1.33 | Si-Si (in c-Si) | 2.35 |
| C=C (graphite) | 1.42 | C-H (sp^3) | 1.09 |
| C \equiv C | 1.21 | Si-H | 1.48 |

The study of a-SiC structure turns to be more complex since the deposition methods, the precursor gases, the hydrogen concentration and the C/Si fraction strongly affect the final a-SiC microstructure and properties [76]. Therefore, the present work is focused on the stoichiometry ($x \approx 0.5$) a-Si_{1-x}C_x:H thin films, synthesized by Radiofrequency sputtering technique. Fig. 1.18 depicts an amorphous structure proposed in this study for the a-Si_xC_{1-x}:H system.

Based on statistical distribution, a-SiC structure can be model as a random network where there is a probability to find homonuclear C-C and/or Si-Si bonds. Furthermore, carbon atoms in a-SiC structures can form homo or heteronuclear p - π bonds in the alloy, i.e. isolated double, triple or resonant π bonding systems. On the other hand, silicon atoms in a-Si networks do not form p - π bonds due to the shielding

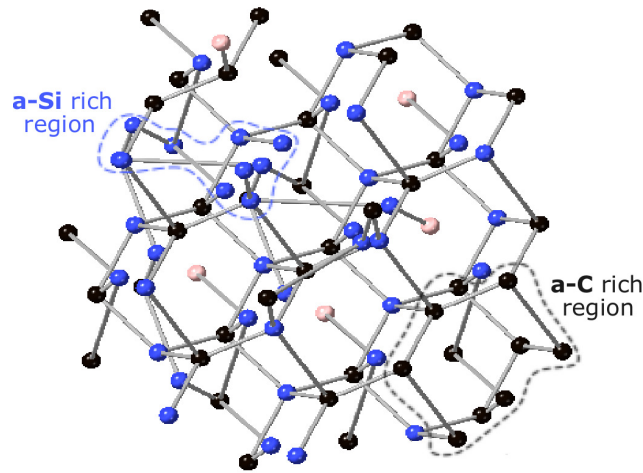


FIGURE 1.18: Example structure proposed for the $a\text{-Si}_{1-x}\text{C}_x\text{:H}$ system. Si (●), C (●) and H (●) atoms are observed conforming $a\text{-SiC}$, $a\text{-Si}$ and $a\text{-C}$ networks. Rich $a\text{-Si}$ and $a\text{-C}$ regions are enclosed in blue and black dashed lines, respectively.

effects the electrons exert between Si atoms [77]. The last feature has as landmark that Si atom exhibits a bigger radius than the C one (see Table 1.2), making Si-Si bonding not as strong as C-C bonding. This is also reflected in the thermodynamically more stable C-C bonds vs Si-Si and Si-C bonds [57]. The existence of $p\text{-}\pi$ bonds in the $a\text{-SiC}$ network makes the structural disorder considerably increases.

TABLE 1.2: Covalent radius and electronegativity of the atoms in the SiC network [75].

| Atom | Radius (10^{-1} nm) | Electronegativity |
|------|---------------------------|-------------------|
| C | 0.77 | 2.50 |
| Si | 1.17 | 1.74 |
| H | 0.28 | 2.20 |

Hydrogen incorporation in the $a\text{-SiC}$ matrix leads to a dramatic change in structural, optical and electrical properties. Concerning the different electronegativities of silicon, carbon and hydrogen atoms (see Table 1.2), C-H bonds exhibit higher stability than Si-H bonds. Consequently, carbon atoms are expected to be more hydrogenated than silicon atoms. These last structural features related to the thermodynamic stability of the $a\text{-SiC}$ matrix, would dominate the mechanism of hydrogen effusion upon post-deposition annealing treatments [57]. Details about heating treatments influence on the $a\text{-SiC:H}$ network structure will be given in the next chapters.

1.7.2 SiC thin films: main fabrication methods

The first attempts reported for growing $a\text{-SiC}$ thin films involved chemical vapor pyrolysis, sputtering and glow discharge techniques. By chemical vapor pyrolysis, a

fine mist of droplets containing reactant elements are directed onto a heated substrate. The substrate temperatures are around 300 and 500 °C and some impurities can be introduced into the droplet solution for doping purposes [78]. Due to the absence of hydrogen in the obtained a-SiC films, this technique has marginal importance in the field of a-SiC production [79, 80].

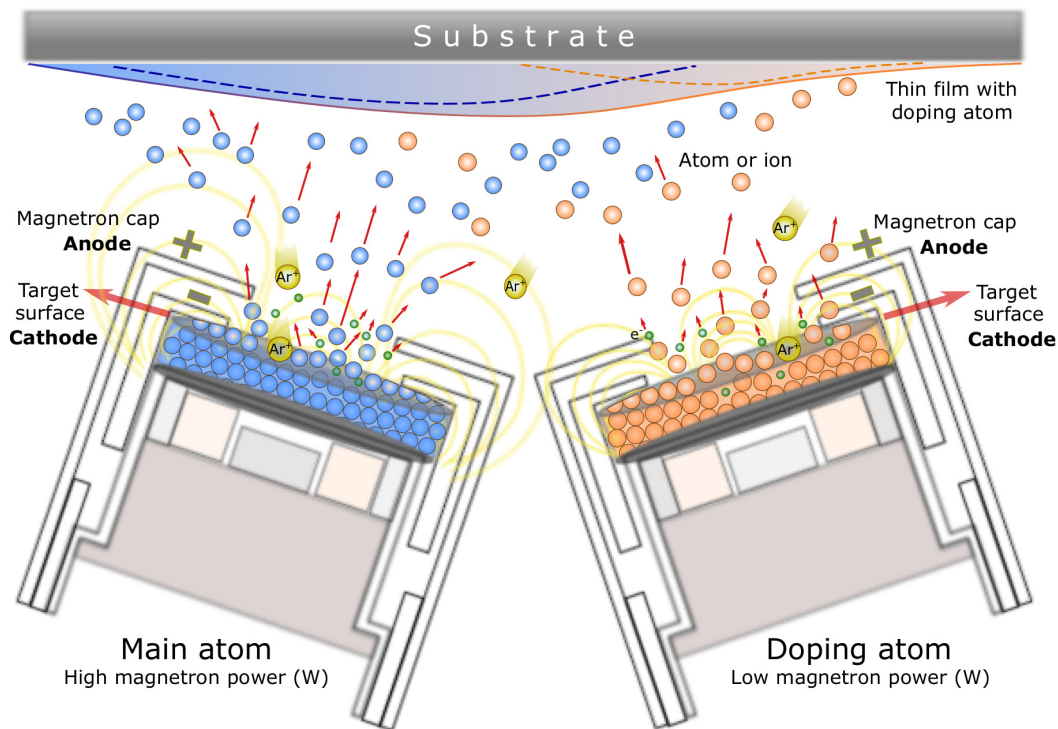


FIGURE 1.19: Schematic representation of a Magnetron sputtering system. Thin film deposition profile is achieved by varying the magnetron powers corresponding to the main and doping atom targets. Ar gas is ionized to create the plasma applying a voltage between cathode and anode.

On the other hand, by chemical vapor deposition (CVD), volatile compounds containing the target atoms are first decomposed and then mixed into a gas which is directed towards a heated substrate [78]. Nowadays, CVD is a widely used technique to produce single crystalline and polycrystalline SiC based materials. Literature for SiC film growth by CVD suggests precursors gases such as SiCl_4 , CH_4 , H_2 , toluene and $\text{H}_3\text{C-SiCl}_3$ to obtain crystalline, polycrystalline and amorphous SiC structures. Very high temperatures are required principally to obtain the gas phases, leading to several problems and peculiarities during operation processes [81]. Thus, temperatures above 1400 and 2200 °C are required to obtain crystalline phases, whereas temperatures above 900 and 1000 °C are even necessary to achieve the amorphous phase. Setting the Si/C ratio from the gas phase and the partial pressure of the hydrogen carrier gas, it is possible to control the a-Si_{1-x}C_x stoichiometry [82]. It is widely reported that the hydrogen content in a-SiC films prepared by chemical vapor pyrolysis and CVD methods, is considerably lower compared to the hydrogen found in films prepared by other deposition methods [83].

Sputtering technique seems to be a relatively more straightforward method to

produce hydrogenated a-SiC thin films at low temperatures. By this technique, a plasma is formed between the target material and the substrate. Target and substrate are placed inside a vacuum chamber containing sufficient pressure to maintain the plasma. Plasma is created by ionization of an inert gas, e.g. Ar or Xe, applying a voltage between the target, which is the cathode, and the substrate attached to the anode. The sputtering process takes place when the target is bombarded with the plasma, so that target atoms gain the sufficient energy to be ejected from the target, travel and reach the substrate [84].

1.8 Fundamental absorption theories

Light absorption measurements are a commonly used approach to obtain semiconductor energy bandgap values. Fitting the fundamental absorption region of the absorption coefficient vs the photon energy $\hbar\omega$ spectrum with a suitable model is the main challenge in this approach. The use of conventional models results in a straightforward procedure to fit the absorption coefficient region. However, these models do not consider the disorder-induced tail states in the material and do not allow for fitting in the whole spectral region. This situation affects the reliability of the extracted bandgap values, specially in amorphous materials, where the disorder-induced tail states are considerably high and overlaps with the region where traditional models, such as Tauc, are used. In amorphous materials, due to the relaxation of the wave vector conservation, the Tauc model for the fundamental absorption can be derived. This model is depicted in Eq. 1.26 [85], whilst the universally observed exponential tail is typically modeled by the empirical Urbach rule, Eq. 1.27 [86].

$$\alpha(\hbar\omega) = M_{\text{Tauc}} \frac{(\hbar\omega - E_{\text{Tauc}})^{1/2}}{\hbar\omega}. \quad (1.26)$$

$$\alpha(\hbar\omega) \propto \exp(\hbar\omega/E_U). \quad (1.27)$$

Here M_{Tauc} is known as Tauc slope, E_{Tauc} the Tauc-gap and E_U the Urbach energy. To extract the optical bandgap value by this model, a plot in the scale $(\alpha\hbar\omega)^{1/2}$ vs $\hbar\omega$ is constructed and a linear fit on the fundamental absorption region is made. The intercept of the linear fit with the energy axis results in the E_{Tauc} . Although the Tauc-gap might not match the real bandgap of the material, it is often used due to its simplicity and for comparison purposes in order to track the variation of the bandgap. The same is applied to the isoabsorption E_{04} bandgap. In this method, the bandgap of amorphous semiconductors is defined by taking the photon energy at which α reaches 10^{-4} cm^{-1} . As the isoabsorption E_{04} bandgap is considered more a convention than a model itself, this will be used in some cases only for comparison purposes along this work, without further discussion. More details on the E_{04} method can be found elsewhere [87]. On the other hand, the Urbach energy contains information of the depth of disorder-induced tail states, meaning that, higher Urbach energies

are associated to higher disorder in the material. It has been demonstrated that structural disorder can be introduced to model the fundamental absorption region by means of band fluctuations for a-Si [88] and for other crystalline and amorphous semiconductors [89]. Here, the used band fluctuations model is shown in Eq. 1.28, where α_0 , $E_{B,F}$ and E_U are the coefficient related to the transition matrix element, the optical bandgap and the Urbach energy, respectively. $\text{Li}_2(z)$ is the dilogarithm function of z . This model merges both Urbach tail and Tauc regions in a single equation. A detailed description of the model can be found elsewhere [89].

$$\alpha(\hbar\omega) = -\frac{\pi}{4} \frac{\alpha_0 E_U^2}{\hbar\omega} \text{Li}_2 \left(-e^{E_U^{-1}(\hbar\omega - E_{B,F})} \right). \quad (1.28)$$



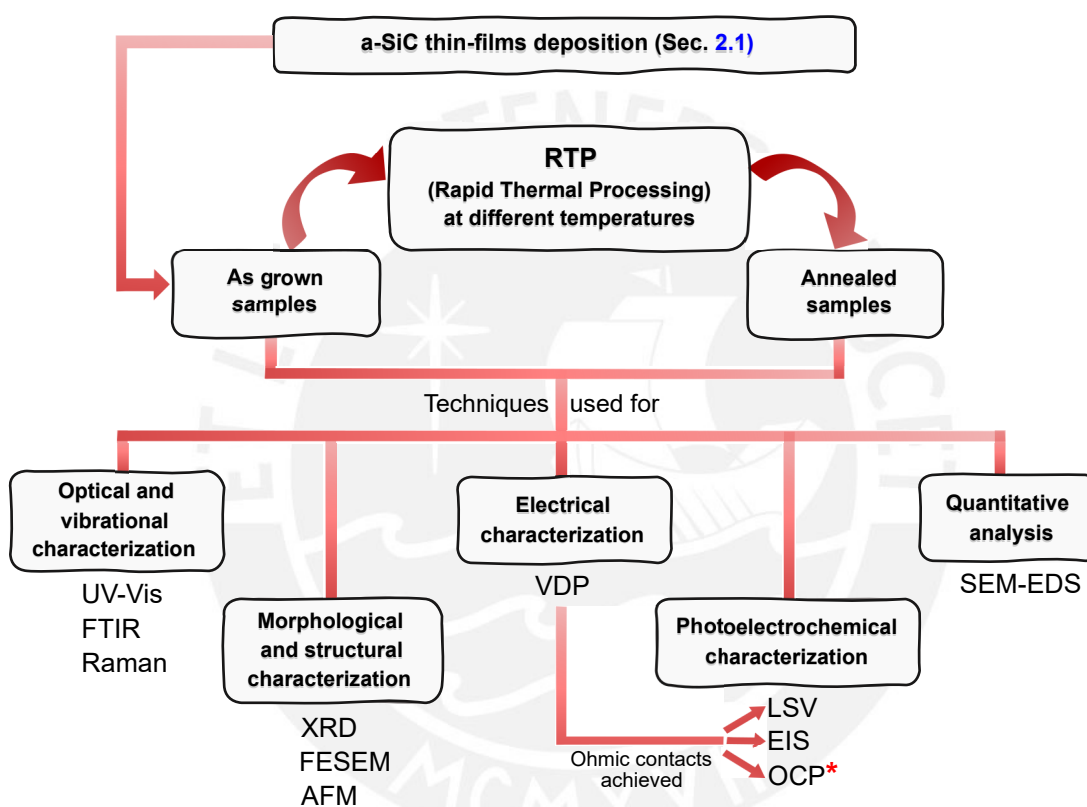
Chapter 2

Experimental details

This chapter contains details about the sample preparation, the photocathodes fabrication, composition measurements, and the structural, morphological, optical, vibrational and photoelectrochemical characterization of the a-SiC:H(Al) film-based photocathodes. Two sets of samples were fabricated for different purposes. The first one, to perform bandgap engineering and assess the surface states role in the photocatalytic performance of the a-SiC:H(Al) photocathodes. Bandgap engineering was performed over a-SiC:H samples and the results are summarized in Fig. 1.17. While the second set of samples was used to evaluate a possible influence of the p and n-type Si substrates in the a-SiC:H(Al) photocurrent response. Different techniques were used to evaluate the a-SiC layers as potential photocatalytic materials. These are summarized in Fig. 2.1.

2.1 a-SiC layer deposition

The a-SiC layers were grown on c-Si and fused silica substrates by reactive Radio frequency magnetron sputtering using a high purity SiC (5N) target under Ar-H₂ atmosphere. The c-Si and fused silica substrates were acquired from Siegert wafer and Microchemicals company, respectively. The sputtering used was made in the laboratory of material science in the Pontificia Universidad Católica del Perú (PUCP)-Physics section. a-SiC films on Si substrates were chosen to perform structural characterization, whereas samples grown on fused silica substrates, were used to perform optical characterization. Three different hydrogen flows were used during the deposition processes, 3, 5 and 15 sccm corresponding to hydrogen dilution concentrations, in the as grown (AG) state, of 1.57 , 3.10 and 4.45×10^{21} atoms/cm³, respectively, as determined by FTIR analysis. A sample without hydrogen (0 sccm) was deposited to be used as blank. Thicknesses of the layers for AG state were around 650 nm, 320 nm, 400 nm and 650 nm, respectively. In order to induce the amorphous state of the layers, the substrate holder was cooled down with a constant flow of water at 12 °C during the deposition processes. Samples were subjected to post-deposition annealing treatments in a Jipelec Jetstar 100 furnace with a constant Ar flux. Different annealing temperatures were chosen in the range from 200 °C to 700 °C to achieve an optimal bandgap value for water splitting as well as good electrical contacts required



* OCP was evaluated in a different set of samples (see Sec. 2.5)

FIGURE 2.1: Techniques used to characterize and evaluate the a-SiC layers as potential photocathodes.

to test the samples in PEC cells. The same sample was used for every heating step and thus, to evaluate the effect of isochronal annealing.

a-SiC:H films with a hydrogen concentration of 1.57×10^{21} atoms/cm³ were chosen to assess the ohmic behavior of electric contacts. This is due to desirable bandgaps for PEC water splitting were obtained for the samples with this hydrogen concentration. For that purpose, additional a-SiC:H samples with Al dopant atoms were grown on p-type c-Si (100) substrates with a resistivity of 2.6 Ω·cm. The deposition process used was Radio frequency magnetron co-sputtering using high purity SiC (5N) and Al (5N) targets. Fig. 2.2 shows a schematic representation of this process.

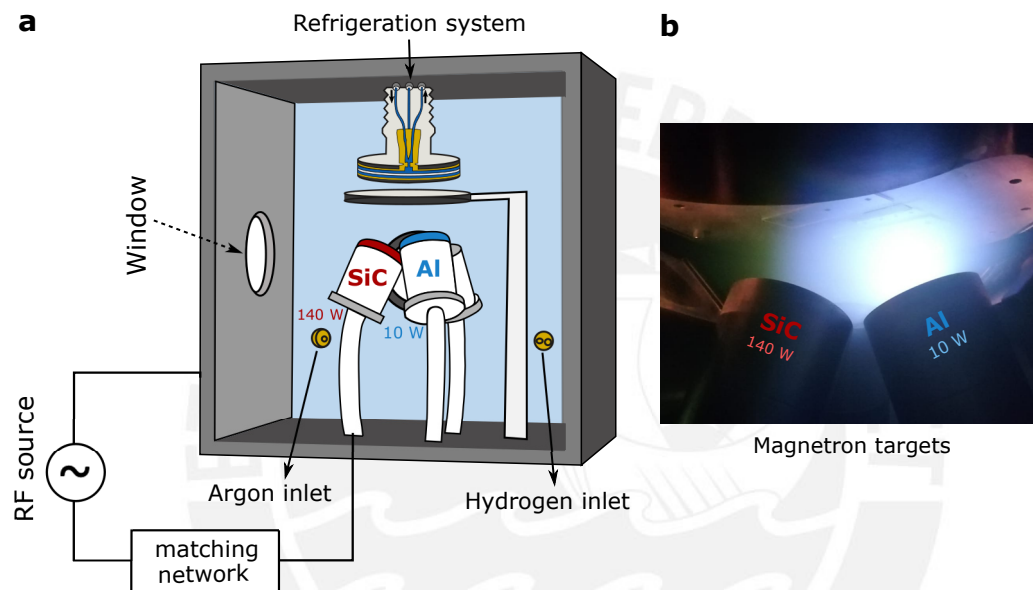


FIGURE 2.2: Scheme of sputtering chamber used for the a-SiC:H(Al) thin films fabrication (a) Radiofrequency Co-sputtering plasma formation with SiC and Al targets (b).

The main parameters of the a-SiC layers are shown in Table 2.1. After doping the a-SiC:H samples with Al, metal contacts, aluminum (20 nm) and titanium (200 nm), were deposited on the samples corners by Radio frequency magnetron sputtering applying pre-designed masks. Al was used to achieved the ohmic contacts by diffusion after performing the annealing treatments, whereas Ti was deposited on the top of the Al contacts for mechanical resistance purposes. For these samples, the annealing step time of 10 minutes was chosen since this is the maximum acceptable time of the process to be considered rapid thermal process. Van der Pauw (VDP) technique was used to confirm the ohmic behavior of the samples.

Table 2.2 summarizes the parameters used in the annealing procedures for each a-SiC sample over Si and fused silica substrates. A further fine-tuning of the bandgap was performed for the sample with 1.57×10^{21} atoms/cm³ of hydrogen concentration, in the range of 200 °C - 600 °C. At 600 °C, an improvement in the electric behavior of the whole system was clearly observed. Therefore, the current study has been focused

TABLE 2.1: Parameters of the a-SiC layers with 0 (a), 1.57 (b), 3.10 (c) and 4.45 (d) $\times 10^{21}$ atoms/cm³ of hydrogen in AG state, respectively. Energy bandgap values were retrieved following the models described in Sec. 1.8.

| $[H] \times 10^{21}$ atoms/cm ³ | Thickness (nm) | Al* (at. %) | E_{Tauc} (eV) | $E_{B,F}$ (eV) | E_U (meV) |
|---|-------------------|----------------|--------------------|-------------------|----------------|
| (a) 0.00 | 650 | - | 1.89 | 2.35 | 395 |
| (b) 1.57 | 320 | 0.32 | 2.33 | 2.59 | 305 |
| (c) 3.10 | 400 | - | 2.39 | 2.85 | 385 |
| (d) 4.45 | 650 | - | 2.96 | 2.96 | 381 |

* Extracted by SEM-EDS

in evaluating the photoelectrochemical performance of sample (b) after annealed at 600 °C.

TABLE 2.2: Annealing treatment parameters of the a-SiC layers with 0 (a), 1.57 (b), 3.10 (c) and 4.45 (d) $\times 10^{21}$ atoms/cm³ of hydrogen in AG state, respectively.

| $[H] \times 10^{21}$ atoms/cm ³ | Annealing temperatures (°C) | Annealing time per step (min) |
|---|--------------------------------|----------------------------------|
| (a) 0.00 | 300, 400, 500, 600, 700 | 15 |
| (b) 1.57 | 200, 300, 400, 600 | 10 |
| (c) 3.10 | 300, 400, 500, 600, 700 | 15 |
| (d) 4.45 | 300, 400, 500, 600, 700 | 15 |

a-SiC:H(Al) films used as photocathodes:

Once the ohmic contacts were obtained, samples were tested as photocathodes in a photoelectrochemical cell. For that purpose, the circuit was closed using silver paste connecting the top a-SiC layer with a copper back contact, which was connected to the external source (potentiostat). The connection between the top of the a-SiC:H(Al) layer with the Cu back contact was done to isolate the system from any influence of the c-Si substrate. Detail of the cell setup is shown in Fig. 2.3.

2.2 Structural and morphological characterization

The a-SiC:H(Al) layer (sample (b) in Table 2.1) was morphologically analyzed using Zeiss Merlin Scanning Electron Microscope with a Schottky field emission source (FESEM). X-ray diffraction patterns were recorded in the 2θ range from 15° to 70° in Grazing Incidence (GI) mode, with a glancing angle of 2°, a scan speed of 1.2°/min and step width of 0.02°, using a Bruker D8 Discover diffractometer with Cu K_α wavelength ($\lambda = 1.54 \text{ \AA}$; 40 kV, 40 mA). Finally, samples surface roughness was evaluated by Atomic Force Microscopy (AFM) before and after thermal treatments as well as before and after the exposure to 1 M sulfuric acid solution. AFM measurements were carried out in an Ar-filled glovebox (M. Braun Inertgas-Systeme GmbH) using a Dimension Icon AFM device from Bruker Co.

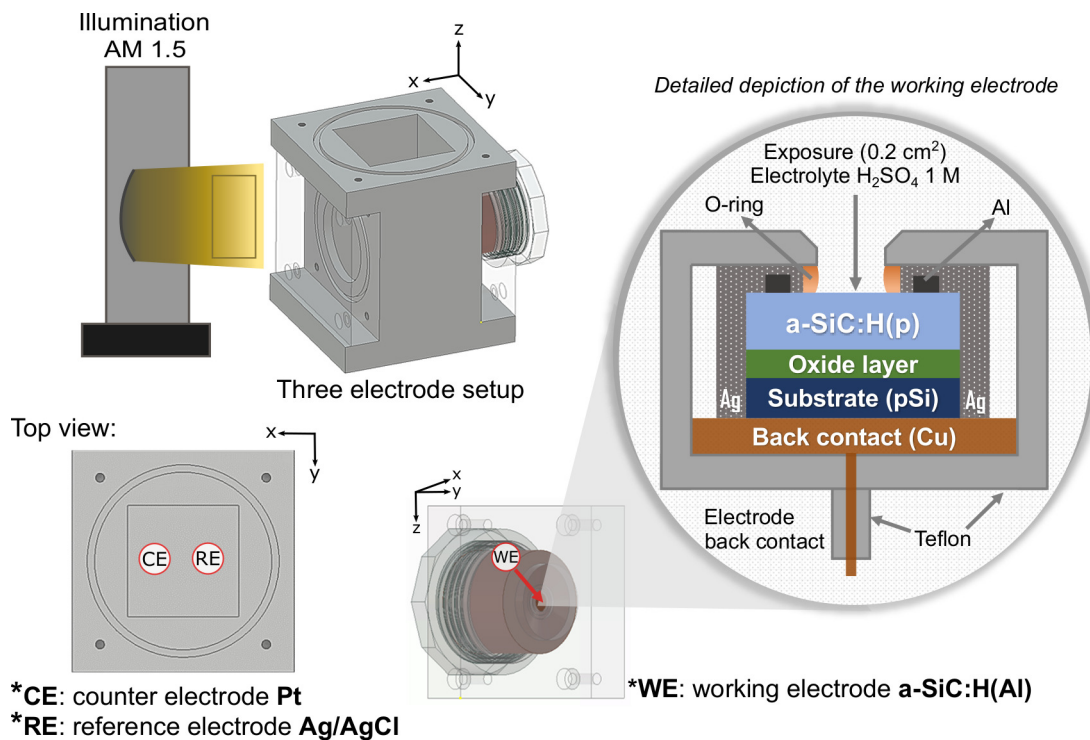


FIGURE 2.3: Detail of the three electrode setup photoelectrochemical cell. A standard AM 1.5 solar spectrum was used to test photocathodes electrochemically. Cell design provided by TU Ilmenau (Germany).

2.3 Optical and vibrational characterization

Optical characterization was performed by transmittance measurements using a Perkin Elmer UV-Vis spectrophotometer Lambda 2-950 in the spectral range from 180 nm to 1500 nm. Thickness (d), refractive index (n_{in}) and absorption coefficient (α) were retrieved from transmittance spectra by a modified envelope method suitable for the determination of the fundamental absorption [90], while the optical bandgap and Urbach energy were determined using the band-fluctuations model for amorphous materials [89].

Hydrogen content and molecular bond-densities were tracked for the distinct annealing temperatures by Fourier Transform Infrared Spectroscopy (FTIR) within the range from 400 cm⁻¹ to 4000 cm⁻¹ using a Bruker FTIR spectrometer Tensor 27. Owing to the baseline calibration with the Si substrate, necessary for this technique, and the fact that Si refractive index is higher than the SiC one, an additional baseline correction was performed. Details about this procedure can be found here [49]. On the other hand, Raman measurements were carried out to track the evolution of Si-Si, C-C and C=C bonds upon the different annealing steps. These measurements were performed using a Renishaw in-Via Reflex spectrometer in the spectral region from 102 cm⁻¹ to 3200 cm⁻¹, with a 488 nm Ar⁺ laser line as excitation source.

2.4 Photoelectrochemical characterization

The photocathodes were photoelectrochemically tested using a VSP-300 potentiostat from Bio-logic Science Instruments in a three-electrode configuration setup, where the c-Si(p)/a-SiC:H(Al) heterojunction with an exposed surface area of 0.2 cm² acts as the working electrode (WE), a platinum foil as the counter electrode (CE) and a Ag/AgCl electrode (in saturated 3.5 M KCl) as a reference electrode (RE). The electrolyte was an aqueous 1 M sulfuric acid (ChemSolute 95%) solution (pH = 0). Current density-voltage (J-V) curves of the photocathodes were measured at a scan rate of 5 mV/s under chopped light illumination (0.1 Hz) from simulated AM 1.5 Solar Irradiation (1000 W/m²) using a solar simulator LOT-QuantumDesign LS0108/15G.

Electrochemical impedance spectroscopy (EIS) was performed in the same solution. The frequency measurement range was 100 mHz-500 kHz with a sinusoidal potential amplitude of 15 mV. Mott-Schottky measurements were performed at fixed frequencies of 30, 40, 50 and 60 kHz. The EIS measurements were carried out for different potential values. For this purpose, the WE potential was scanned anodically from -1.0 to 1.5 V vs. Ag/AgCl (3.5 M KCl), recording data every 35 mV. Alternating current (AC) impedance spectroscopy characterization in dark was performed by EC-LAB Analysis and Data Process software.

2.5 Evaluation of the substrate influence in the photocurrent response

a-SiC:H(Al) layers were grown onto p-type and n-type c-Si $\langle 100 \rangle$ substrates by Radiofrequency magnetron co-sputtering. The substrates were provided by Sievert wafer company. The sputtering used was made in the laboratory of material science in the Pontificia Universidad Católica del Perú (PUCP)-Physics section. The Si substrates exhibited a resistivity of 2.7 Ω -cm. The SiC and Al targets were the same used for previous deposition (Sec. 2.1), as well as the Ar-H₂ atmosphere. With the purpose of evaluating the substrate influence in the kinetic of water splitting reaction, thinner films were deposited using lower magnetron powers, i.e. 120 W and 5 W for SiC and Al targets, respectively. Table 2.3 summarizes the main parameters of the a-SiC:H(Al) thin films in as grown state for this process.

TABLE 2.3: a-SiC:H(Al) thin films parameters used to evaluate the substrate influence in the photocurrent response of the c-Si(p)/a-SiC:H(Al) and c-Si(n)/a-SiC:H(Al) photocathodes. Energy bandgap values were retrieved following the models described in Sec. 1.8.

| Thickness (nm) | Al* (at. %) | E _{Tauc} (eV) | E _{B,F} (eV) | E _U (meV) |
|-------------------|----------------|---------------------------|--------------------------|-------------------------|
| 230 | 0.40 | 2.80 | 3.00 | 430 |

* Extracted by SEM-EDS

Thermal annealing processes were carried out over the AG samples, at 600, 700 and 800 °C, to obtain the ohmic contacts. Heating time periods ranged between 10 to 18 min. The films were photoelectrochemically tested in the PEC cell depicted in Fig. 2.3.



Chapter 3

Results and discussion

In-depth analysis of the physical and photoelectrochemical properties of a-SiC film-based photocathodes were performed. The former, based on bandgap engineering, and the latter, on the steady-state and dynamic electrochemical models described in Sec. 1.4. The analysis were performed by varying the hydrogen concentration in the a-SiC:H layers and by post-deposition isochronal annealing treatments (see Fig. 1.17). The improvements in opto-electronic properties and photocatalytic efficiency, related to the photocurrent generation during water splitting reaction, are explained in detail in this chapter. The chapter is divided in three main sections. In the first section, results concerning the bandgap engineering, the structural, and the electrical characterization are shown for a-SiC, a-SiC:H and a-SiC:H(Al) samples, grown on p-type Si and fused silica substrates. In the second section, influence of the Si substrate conductivity type in the photocurrent response is assessed for the c-Si(p)/a-SiC:H(Al) and c-Si(n)/a-SiC:H(Al) systems described in Sec. 2.5. Finally, in the third section, results concerning the surface states influence in the photocurrent response, as well as in the photocathode stability under darkness and illumination conditions are shown.

3.1 Bandgap engineering, structural and electrical characterization of a-SiC film-based photocathodes

3.1.1 Optical characterization of a-SiC thin films

Fig. 3.1 depicts the optical transmittance and absorption coefficient in Tauc scale of the four a-SiC samples (Table 2.1) in as grown state. Tauc-plots reveal a linear region, from which the Tauc-gap can be retrieved from Eq. 1.26. Additionally, the fits using Eq. 1.28 are also shown. Note that the shift in the fundamental absorption region observed in the Tauc plots is also reflected in the transmittance measurements. As the transmittance is proportional to $e^{-\alpha \cdot d}$, we notice that the lower the E_{Tauc} , the transmittance starts at lower photon energy (higher wavelength).

Fig. 3.2 depicts E_{04} , E_{Tauc} and $E_{\text{B,F}}$ vs the annealing temperature (T_{A}). The existence of a critical temperature between 400 and 500 °C for the hydrogenated a-SiC samples at which E_{04} and E_{Tauc} reach maximum values is observed. For samples

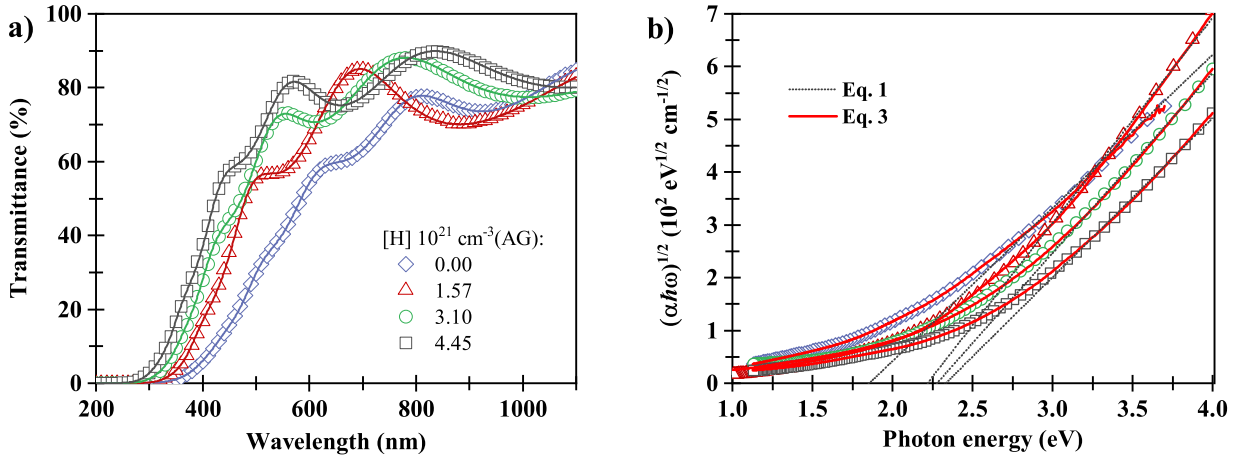


FIGURE 3.1: Optical transmittance (a) and absorption coefficient in the Tauc scale (b) of the a-SiC:H layers. The solid lines in (a) correspond to the fits following the modified envelope method [90]. The red solid curves denote fits using the dilogarithm equation (Eq. 1.28) (b). The gray dashed lines correspond to linear fits (Eq. 1.26) in the Tauc region (b). The legend denotes the different hydrogen concentrations ($\times 10^{21}$ atoms/cm³) of the as grown state.

without hydrogen this temperature lies at 500 °C. This is not the case for the $E_{B,F}$ values which are always higher than E_{Tauc} in agreement with the bias induced by the overlap of the Urbach tails on the fundamental absorption region [89].

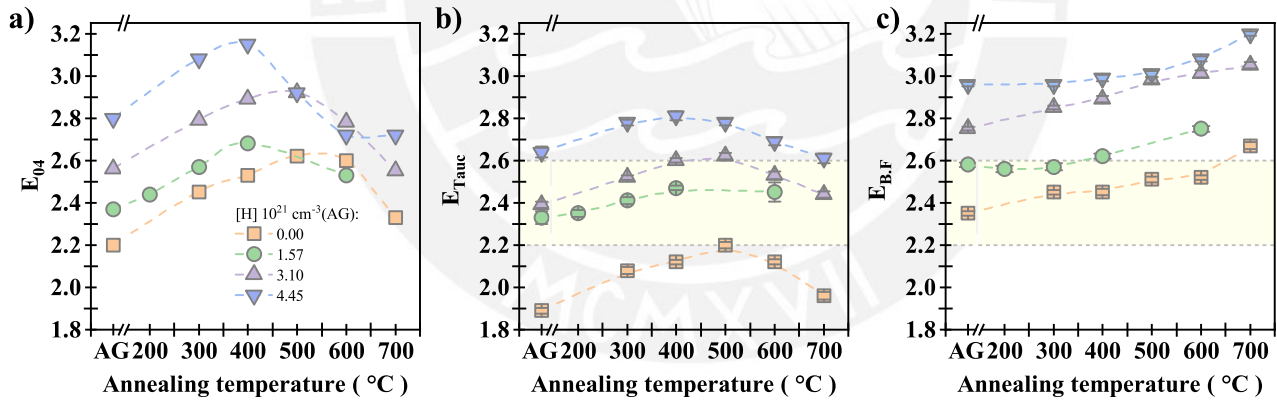


FIGURE 3.2: Energy bandgaps of the a-SiC:H films extracted by means of three methods: isoabsorption (E_{04}) (a), Tauc (E_{Tauc}) (b) and band fluctuations ($E_{B,F}$) (c). The legend denotes the different hydrogen concentrations ($\times 10^{21}$ atoms/cm³) obtained after deposition before thermal treatments. The highlighted regions in (b) and (c) denote the region of optimal E_{gap} for solar water splitting purposes.

Thickness variation vs T_A plots were registered, as observed in Fig. 3.3. A critical temperature at 400 °C is found for the samples diluted with hydrogen, at which the material shrinks. This implies a mean-bond length shrinking of the a-SiC:H layers. The effect can be directly associated to the optical bandgap widening observed in Fig. 3.2 only for the $E_{B,F}$ values. The decrease of the E_{04} and E_{Tauc} with annealing temperatures above 400 °C can be traced back to the enhancement of Urbach tails. Since the overlapping effect is only considered in the band fluctuations model, this

would suggest that the $E_{B,F}$ values are more accurate in contrast to E_{Tauc} and E_{04} . A correlation between thickness and $E_{B,F}$ is not clearly observed for the samples without hydrogen.

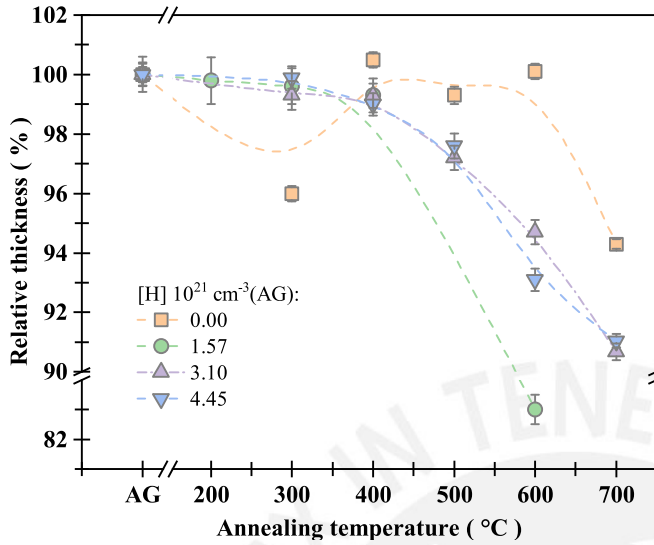


FIGURE 3.3: Thickness variation of the a-SiC:H samples that takes place upon each step of isochronal annealing treatment. The legend denotes the different hydrogen concentrations ($\times 10^{21}$ atoms/cm³) obtained in the as grown state. Values are expressed as relative thicknesses for comparison purposes.

An slight increment in thickness was observed for the sample without hydrogen upon the 400 and 600 °C annealing steps. This effect is also reflected in the density, which decreases at these temperatures, from 2.89 to 2.57 g/cm³ upon the annealing at 400 °C, and from 2.66 to 2.40 g/cm³ upon the 600 °C heating step. The phenomenon could be linked to the formation of voids inside the films, possibly originating from the oxidation of the air exposed a-SiC layers occurring after the heating processes [91, 92]. Mass density values were estimated using refractive indices following the Lorentz-Lorentz (L-L) relation shown in Eq. 3.1. Here, n_{in} is the refractive index, ρ is the mass density, A_0 is the Avogadro's number, M is the molecular weight and α' is the molecular electronic polarizability, which is around 1.4 Å³ [93]. Refractive indices were obtained from transmittance measurements using a modified envelope method at 800 nm wavelength [90].

$$\frac{n_{in}^2 - 1}{n_{in}^2 + 2} = \left(\frac{\rho A_0}{M} \right) \frac{4\pi\alpha'}{3}. \quad (3.1)$$

The range of optimal bandgap energies for PEC water splitting has been highlighted in Fig. 3.2 for the E_{Tauc} and $E_{B,F}$ values. As is noticed for the $E_{B,F}$ values, only a-SiC samples with no hydrogen and low hydrogen dilution conditions lie in this range. However, samples without hydrogen possess a higher density of localized states on the neighborhood of the Fermi level compared with those samples presenting hydrogen in its composition. Typically, hydrogen dilution reduces the density of localized states in the vicinity of band-edges. It is well known that localized states in the bulk of the semiconductor can act as recombination centers of photogenerated charge carriers [94–96], decreasing the efficiency of the semiconductor to conduct PEC water splitting. Since the last effect must be avoided or reduced, and considering a desirable bandgap, the following discussion about structural and opto-electronic

properties is principally focused on the samples with the lowest hydrogen dilution conditions, i.e. the 1.57×10^{21} atoms/cm³ sample (see Table 2.1).

Fig. 3.2 depicts that a sufficiently high energy bandgap, able to generate the power to split water, is achieved after performing the annealing at 200 °C, i.e. 2.55 eV ($E_{B,F}$) [12]. Higher bandgaps, obtained after exposing the samples to higher temperatures, would avoid harvesting a significant amount of the sun-delivered energy, in the region of maximum photon flux of the AM 1.5 solar spectrum (Fig. 1.17). In addition to this fact, both, hydrogen concentration and thickness remain almost constant upon performing the 200 °C heating step. Nevertheless, after this annealing step no ohmic behavior of the contacts is observed, which is a key requirement for the PEC to work properly.

3.1.2 Structural and electrical analysis of a-SiC thin films

Fig. 3.4 highlights the thermal-induced thickness shrinking and densification that takes place on the a-SiC:H(Al) film after annealing at 600 °C. The thickness shrinking is approximately 55 nm, i.e. from 320 to 265 nm, and the densification occurs from 3.04 to 3.12 g/cm³. SEM images are shown for the a-SiC:H(Al) layers in the as grown (a) and annealed at 600 °C (b) states. Similar results were obtained after fitting the corresponding UV-Vis transmittance spectra and assessing the thickness variation with T_A .

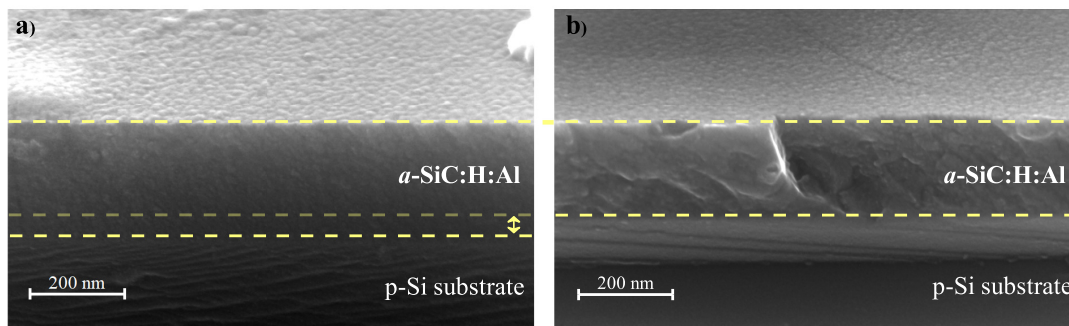


FIGURE 3.4: FESEM Tilt-section images of c-Si(p)/a-SiC:H(p) as grown sample (a) and annealed sample (b). Thickness shrinking by about 55 nm is highlighted.

As mentioned in experimental details, metal contacts, Al and Ti, were deposited on the sample corners to perform four-point electrical measurements and assess the samples electrical behavior. Additionally, Al atoms were incorporated into the a-SiC:H ([H] = 1.57×10^{21} atoms/cm³) layers in a very low concentration to improve its conductivity. The thermally-induced Al diffusion into the a-SiC:H(Al) layers creates a highly doped area, i.e. p⁺, just below the p-type semiconductor surface [23]. This effect takes place at around 300 °C, when the Al diffusion becomes significant. A very thin p⁺ region facilitating hole tunneling from the semiconductor to the Al metal contact and vice versa, was achieved after performing the annealing step at

600 °C. Thus, Fig. 3.5 depicts the ohmic behavior of the sample after being subjected at 600 °C.

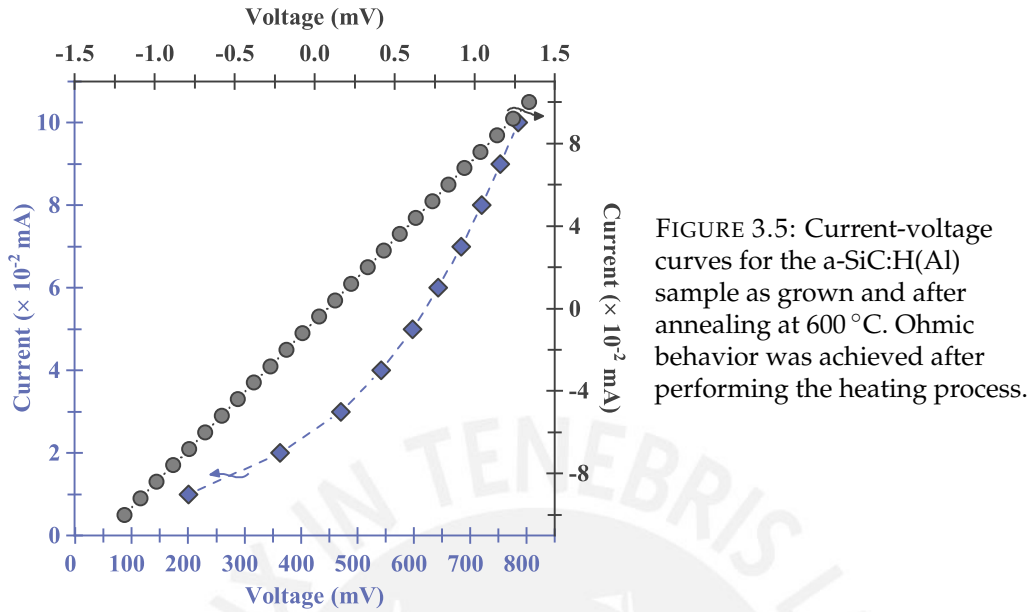


FIGURE 3.5: Current-voltage curves for the a-SiC:H(Al) sample as grown and after annealing at 600 °C. Ohmic behavior was achieved after performing the heating process.

To correlate the optical and structural information, Gaussian fits of the IR absorption peaks observed in Fig. 3.6 were performed. Vibrational states and inverse absorption cross section values (k') for the different bonds presented in a-SiC:H are shown in Table 3.1. k' values were used to calculate the bond density (N), according to Eq. 3.2, where ν is the wavenumber.

TABLE 3.1: Vibrational states and inverse absorption cross sections (k') for the different bonds presented in a-SiC:H thin films.

| Vibrational mode | Wavenumber (cm ⁻¹) | Inverse absorption cross section (cm ⁻²) |
|---------------------------------------|--------------------------------|--|
| Si-C Asym. stretching | ~790 | 2.13×10^{19} |
| Si-CH _n Wagging/rocking | ~1000 | 2.13×10^{19} |
| Si-H Stretching | ~2100 | 1.40×10^{20} |
| C-H Stretching | ~2890 | 1.35×10^{21} |

$$N = \kappa' \int \left(\frac{\alpha(\nu)}{\nu} \right) \delta\nu. \quad (3.2)$$

In Fig. 3.6, the FTIR analysis reveals a thermally-induced hydrogen out-diffusion. Previous studies have proved that hydrogen release from an a-SiC:H bulk takes place in two steps. First, the breaking of the thermodynamically less stable Si-H bonds (70.4 Kcal/mol), and subsequently, the breaking of the C-H bonds (98.9 Kcal/mol). During the first dehydrogenation step, hydrogen atoms from the

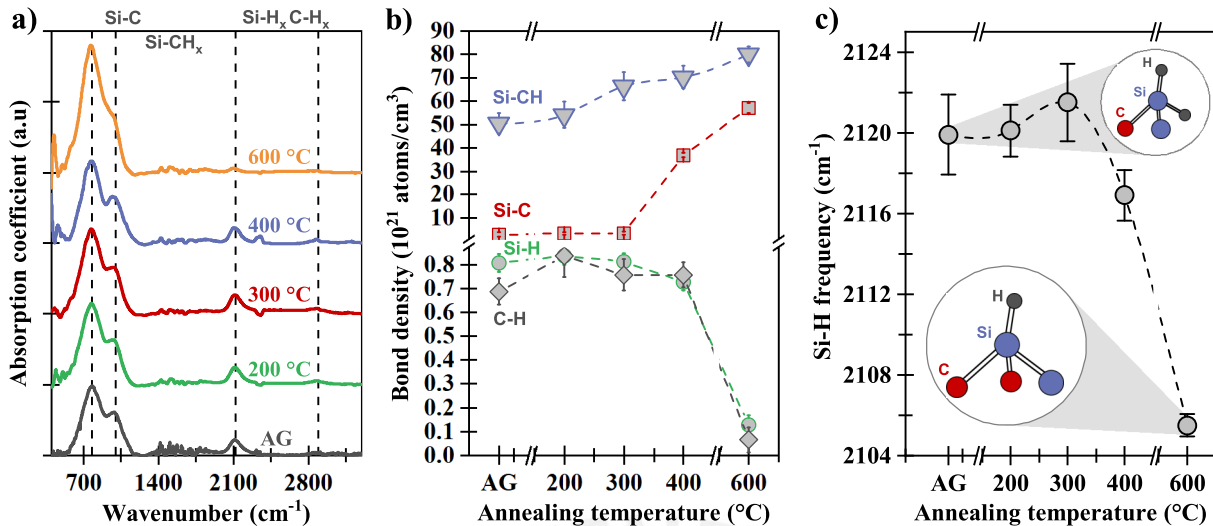


FIGURE 3.6: Absorption coefficient (a), Bond density (b) and Si-H frequency shifting (c) obtained for the a-SiC:H(Al) sample grown with 1.57×10^{21} atoms/cm³ of hydrogen, after each annealing step. Bond density values (b) according to Eq. 3.2. Differences in chemical environment of the Si-H bonds were monitored by means of Si-H frequency shifting (c).

Si-H bonds might saturate carbon dangling bonds, giving rise to new C-H oscillators at temperatures below 600 °C [97]. This behavior could explain the slight increase of C-H bonds observed in the initial heating stage, at 200 °C heating step. For higher annealing temperatures, both Si-H and C-H bonds deplete, exhibiting an abrupt depletion after 600 °C annealing. Therefore, Si-H and C-H bonds dissociate to conduct the formation of new Si-C bonds, as a significant increment in Si-C bond density is observed after annealing treatments at temperatures in the range of 300 - 600 °C, this increment is also affected by the thermally-induced densification. The almost linear increment of Si-CH_n bonds along all the heating temperatures is probably due to the breaking of C-H₃ bonds to yield new C-H₂ bonds. Both kind of bonds belong to the Si-CH_n band and were also considered when performing the fittings. Another important feature to analyze is related to the vibrational frequency of the Si-H bonds that shifts with each annealing step. Shifting of the bond frequency is attributed to an induced effect by nearest neighboring atoms. Thus, differences in chemical environment of the Si-H bonds were monitored during the heating treatments. Presence of hydride structures, i.e. Si-H₂, are detected [57, 98]. As a general trend, the replacement of one hydrogen atom by a carbon atom is observed, taking place around a Si-H₂. This trend is reflected in a vibrational frequency shifting of the absorption band associated to Si-H bonds, from 2120 to 2105 cm⁻¹.

Annealing treatments have an impact in the disorder related band-tail states. These can be tracked by the E_U and the FWHM of the absorption bands from FTIR measurements. Fig. 3.7 shows the Urbach energy vs T_A plot for the a-SiC:H(Al) samples with $[H] = 1.57 \times 10^{21}$ atoms/cm³. A critical temperature at 400 °C is observed where E_U reaches its minimum value. The shrinking of the E_U taking place from the as grown state to 400 °C annealing, is attributed to the thermally-induced

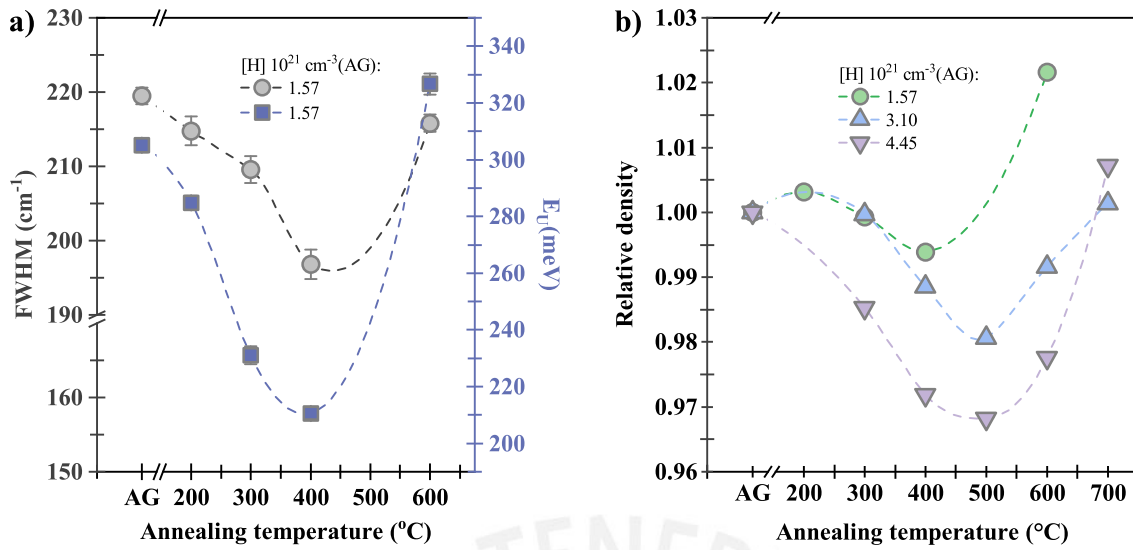


FIGURE 3.7: E_U (red squares) and FWHM values (gray circles) for the a-SiC:H(AI) sample with the lowest hydrogen concentration, i.e. grown with $[H] = 1.57 \times 10^{21}$ atoms/cm³ (a). Relative density variation with annealing temperature for the hydrogenated samples (b).

structural relaxation. This relaxation is corroborated by the FWHM extracted from the absorption peaks in the FTIR spectra of the same sample, depicted in Fig. 3.6. For comparison purposes, FWHM vs T_A plots are shown in the same Urbach energy plot. FWHM values were retrieved from the Si-CH_n absorption band. An identical trend is observed for the FWHM and the E_U behavior. The same behavior is observed for the mass density versus the annealing temperature, shown in the same figure. This indicates that the increment in the disorder related band-tails states would not be only associated to the thermally-induced hydrogen out-diffusion, but also to the structural changes observed by FTIR and Raman measurements.

Raman spectroscopy measurements (Fig. 3.8) for the a-SiC samples without hydrogen were performed after subjecting the samples to isochronal annealing at 300, 400 and 600°C. These show a broad band centered at $\sim 1450 \text{ cm}^{-1}$. This band is associated to the presence of amorphous carbon clusters, dominated by sp^2 -bonded carbons, embedded in an a-SiC matrix [99]. Consequently, it is suggested that the thermally-induced disorder relaxation promoting a decrease of the E_U competes with the formation of carbon rich regions promoting the increase of E_U . On the other hand, it is known that hydrogen prevents the formation of sp^2 -bonded carbons in the a-SiC films [100]. Overall, hydrogen presence seems to induce a short range localized structural ordering in the a-SiC matrix. This evidence explains why as the hydrogen content increases in the a-SiC samples, there is greater E_U shifting towards lower values, as it is observed in Fig. 3.9.

Figure 3.9 shows an E_U minimum for all the samples. For the hydrogenated ones, this E_U critical temperature corresponds to the T_A from which an abrupt a-SiC thickness shrinking takes place (see Fig. 3.3). The corresponding FWHM vs T_A plots are shown in the same figure. FWHM values were retrieved from the main absorption

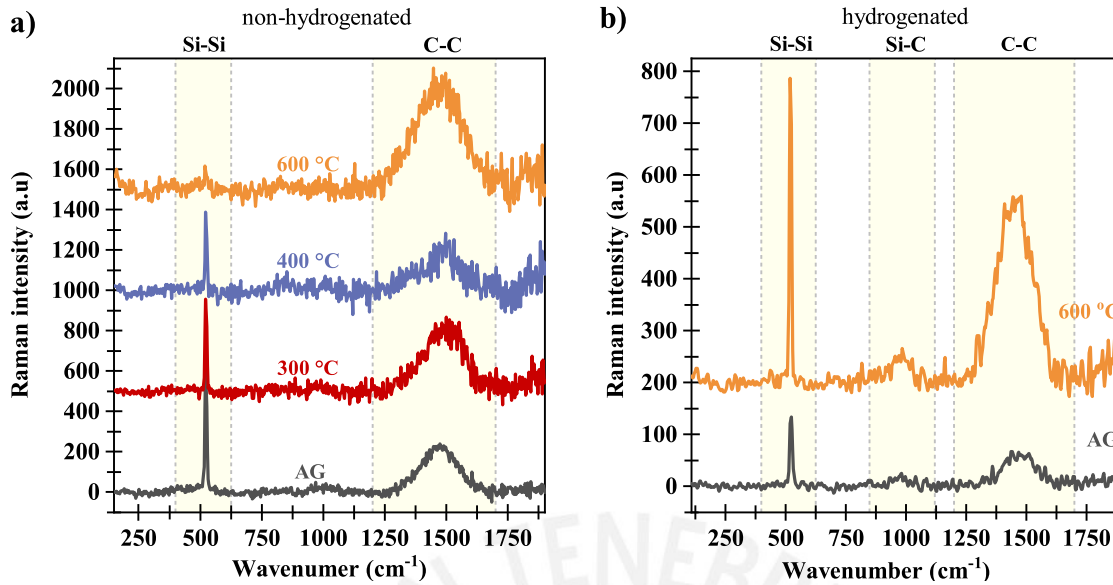


FIGURE 3.8: Raman spectra after different annealing steps obtained for the non hydrogenated a-SiC sample. Si-Si and C-C bands are highlighted (a). Raman spectra of the a-SiC:H(Al) sample ($[H] = 1.57 \times 10^{21}$ atoms/cm³) for the as grown and the annealed state at 600 °C. An increment in the Si-Si, Si-C and C-C modes is detected after the heating process (b). A 488 nm Ar⁺ laser line was used as excitation source.

bands, i.e. the Si-C band for the a-SiC samples without hydrogen and the Si-CH_n band for the hydrogenated ones. Certainly, E_U and FWHM keep the same behavior vs T_A , supporting that the thermally-induced disorder relaxation is responsible for the E_U shrinking in a first heating stage, at relatively low temperatures, for all the a-SiC samples, with and without hydrogen. This effect remains until a significant film thickness shrinking occurs at the critical temperature. Moreover, an interesting E_U behavior to analyze is the one that takes place at 300 °C. Thus, it seems that the lower the hydrogen concentration is in the a-SiC matrix, the more the E_U is shifted towards higher energy values above the expected trend line (dash lines). This behavior has been highlighted in Fig. 3.9 and it suggests that another amorphous phase might be promoted with the annealing process at 300 °C, specially in samples with low hydrogen concentration.

Figure 3.8 also depicts the Raman spectra of the a-SiC:H(Al) sample with the lowest hydrogen concentration ($[H] = 1.57 \times 10^{21}$ atoms/cm³) in its as grown state and after an annealing treatment at 600 °C. The broad peak centered at ~ 1450 cm⁻¹ is observed in both spectra, although with a significantly higher intensity after the annealing treatment. It was not possible to perform band deconvolution of this band in order to obtain D (1350 cm⁻¹) and G (1580 cm⁻¹) graphitic characteristic bands. This suggests that the carbon atoms inside the a-SiC:H(Al) bulk continue being amorphous, without any appreciable formation of graphite crystals after being subjected to the 600 °C heating step. This feature would be in part responsible for the abrupt increase detected in E_U and $E_{B,F}$ in the range of 400 - 600 °C annealing step, as well as the structural changes (see Fig. 3.7).

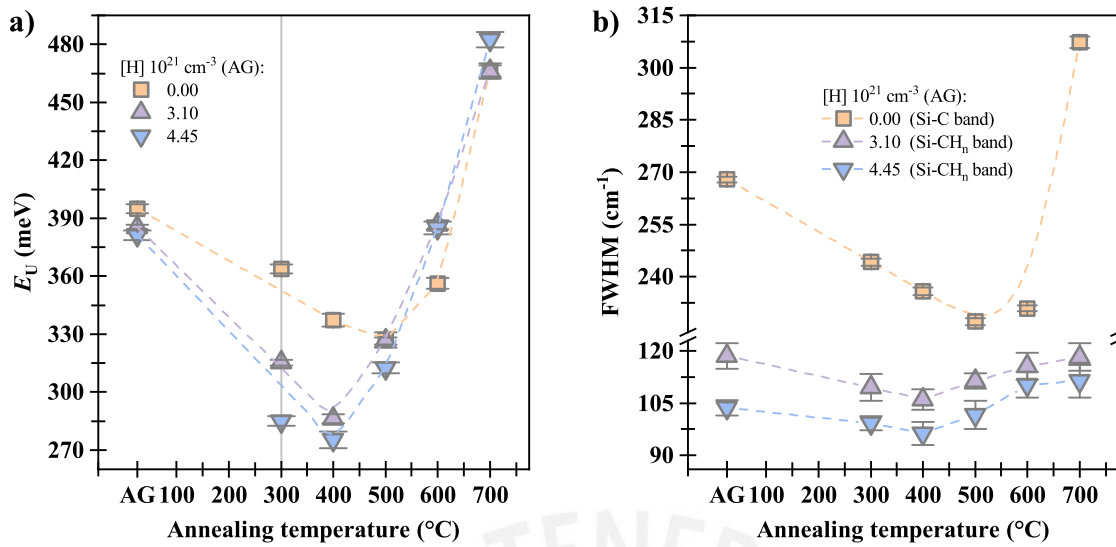


FIGURE 3.9: E_U (a) and FWHM values (b) for the a-SiC samples. The legend denotes the different hydrogen concentrations ($\times 10^{21}$ atoms/cm³) obtained in the as grown state. The same trend is observed for the E_U curves and their corresponding FWHM curves for the hydrogenates samples. The E_U behavior at the 300 °C annealing step, marked with the solid gray line (a) reveals the effect of hydrogen presence over the short range localized structural ordering exhibited in the a-SiC matrices. E_U is shifted towards lower values, below the corresponding dashed trend line (a), as the hydrogen content increases in the samples. On the contrary, for the sample without hydrogen, an E_U shifts towards higher values, above the dashed trend line (a), is observed at 300 °C.

Fig. 3.10 depicts a continuous random network model for the a-SiC:H structures, for a sample composition of a-Si_xC_{1-x} with a maximum level of disorder expected in the range between $x = 1$ and $x = 0$ [41]. The former case corresponds to a pure amorphous silicon network, while the latter, to a pure amorphous carbon network. Since the stability of C-C bonds is higher compared with the one of Si-Si bonds, i.e. 356 kJ/mol and 226 kJ/mol, respectively [75], it is quite likely to find more regions showing a pure a-C network rather than a pure a-Si one. This feature becomes more accentuated at $x \leq 0.5$.

The a-Si_xC_{1-x}:H structures proposed contemplate an $x = 0.5$ composition for the as grown state and after an annealing treatment at 600 °C. Hydrogen atoms are depicted as pink balls occupying void centers [57], triggering a localized short range order in the amorphous structure. Carbon and silicon random networks can also be observed in both states. However, for the relaxed annealed structure, owing to the hydrogen depletion taking place upon the heating process, more a-C rich regions are expected to be found. In agreement with the FTIR analysis described earlier, the remained hydrogen atoms would be forming Si-CH_n instead of Si-H bonds, as shown in Fig. 3.6b. Finally, considering a carbon content not higher than 0.5, it is suggested that carbon clusters do not exhibit a graphitic configuration, but C=C bonds conforming an amorphous phase [57]. This amorphous carbon phase turns to be greater after the annealing treatment, contributing to the increment in the structural disorder. This

effect is reflected in an Urbach energy increase from the critical annealing temperature from which disorder related states are enhanced.

3.1.3 Summary of Section 3.1

Bandgap engineering of a-SiC:H thin films based photoelectrodes varying hydrogen concentration and by post-deposition annealing treatments results in a wide range of energy bandgaps suitable for photoelectrochemical water splitting. The bandgap obtained from the band fluctuations model results more reliable compared to the conventional ones (E_{Tauc} , E_{04}), since it considers the disorder-induced tail states that are predominant in amorphous materials. In particular, the increasing behavior of the $E_{B,F}$ upon the whole isochronal annealing treatments is in agreement with the evidence of an amorphous C=C phase formation and a-SiC structural changes taking place during the heating process. This behavior was not detected from the E_{Tauc} nor E_{04} energy bandgaps. However, critical temperatures were detected from both latter models, at which E_{gap} reaches the highest value and from which E_U starts to increase. Although E_{gap} values extracted by the band fluctuations model seem not to significantly differ from those extracted from the previous conventional models. These differences (between 0.1 and 0.3 eV), would have a significant impact in the absorption of AM 1.5 solar radiation, and thus, in the solar-to-hydrogen conversion efficiencies for solar water splitting [34–38].

Even though optimal composition and optical bandgap energy ($E_{B,F}$) for solar water splitting were obtained after performing the annealing step at 200 °C, there

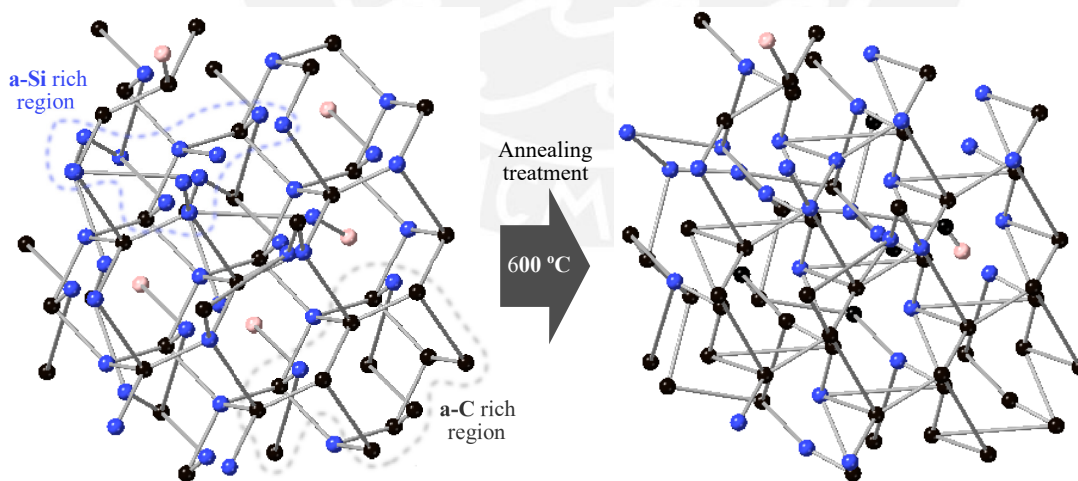


FIGURE 3.10: Example structures proposed for the a-Si_xC_{1-x}:H system in as grown and an annealed state at 600 °C. Si (●), C (●) and H (●) atoms are observed forming a-SiC, a-Si and a-C networks. Rich a-Si and a-C regions are enclosed in blue and black dashed lines, respectively. Disorder increases after thermally-induced hydrogen releasing. Since hydrogen atoms are depleted upon the annealing treatment, more a-C rich regions are expected. Hydrogen remanent atoms in the annealed state are preferably found bonded with carbon atoms instead of silicon atoms.

was no improvement in the electrical performance of the photoelectrode device - a-SiC:H(Al) thin film over c-Si(p) substrate- upon this heating step. It was only after heating at 600 °C that ohmic contacts were obtained, compromising the hydrogen passivation due to the abrupt hydrogen depletion occurring at this temperature.

Finally, the results presented here support the structural rearrangement mechanisms taking place along the whole annealing temperature range. In a first heating temperature range, from the as grown state until being subjected to a critical annealing temperature (at which E_U reaches its minimum value), samples exhibited a disorder-induced structural relaxation. This effect is associated to a hydrogen-release induced structural reordering from the matrix, as it was corroborated by FTIR measurements. While in a second range, from the critical to higher annealing temperatures, a significant structural disorder is mainly attributed to the formation of an additional amorphous carbon phase. This was corroborated by Raman measurements. It is only suggested that the disorder induced by pseudo-hybridization states and amorphous carbon phases, rather than the hydrogen concentration, is the main determining factor in the bandgap ($E_{B,F}$) increasing behavior. More studies need to be performed in order to evaluate how the thermally-induced thickness shrinking would affect the photoelectrochemical a-SiC:H performance, as well as to find a compromise between good hydrogen passivation strategies and good electrical features for c-Si(p)/a-SiC:H(Al) photoelectrodes.

3.2 Substrate influence in the photocurrent response of the a-SiC:H(Al) absorber layer

Research in thin film photoactive materials for water splitting does not typically consider the role of the substrate in the PEC performance. Thus, depending on the depth of the space charge region, charge carriers from the substrate may have an important impact on the PEC performance, affecting the photocurrent response.

The analyses presented in this section correspond to the samples described in Sec. 2.5. Since it was confirmed that ohmic contacts were obtained for the a-SiC:H(Al) layers after an annealing at 600 °C, the same procedure was carried out over the a-SiC:H(Al) films deposited onto p-type and n-type c-Si substrates. Nevertheless, ohmic contacts were not achieved in the latter case. This effect is attributed to the difference in thickness exhibited for both sets of samples, i.e. 320 vs 205 nm, for the samples described in Sec. 2.1 and Sec. 2.5, respectively. Thickness influence in resistivity plays an important role in thin films, which is mainly associated to structural growth factors of the films. Details about thin films grown will be addressed in this section.

Additional annealing treatments were performed for the samples over n-type c-Si substrates, at 700 and 800 °C, during a 10 mins period. Further heating steps, from 900 °C onwards, were avoided since these induce recrystallization from the a-SiC surface [101]. However, despite the temperature increase, ohmic contacts were not obtained until a 700 °C heating step for 18 min, was performed.

This section will only discuss the results concerning the Rapid Thermal Annealing processes, taking place during 10 min period of holding time, without the ohmic contacts. Although the ohmic contacts were not achieved for these samples, it was still possible to detect a substrate influence trend with the annealing.

3.2.1 Isotype and anisotype heterojunctions

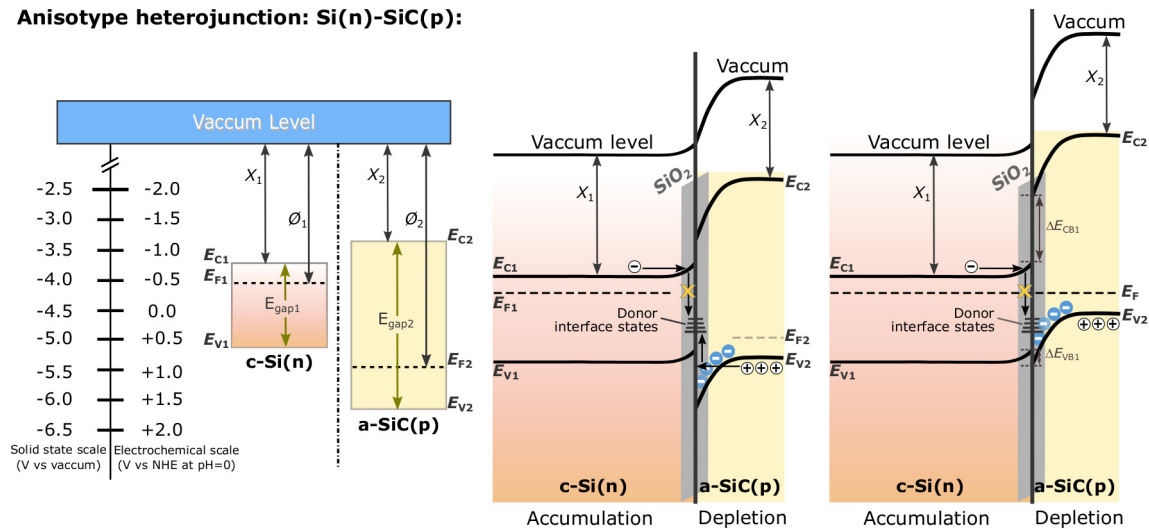
As Si substrate surfaces were not etched prior to the a-SiC:H(Al) grow, the existence of surface states originated from the hydroxyl group termination of the SiO₂ native layer would dominate the electronic behavior of the solid-solid interface. Previous studies have reported that these states are situated at 0.5 V vs. RHE [52] and used to behave as charge carrier donors rather than acceptors [102]. Therefore, the electron-capture efficiency of the c-Si(p)/a-SiC:H(Al) and c-Si(n)/a-SiC:H(Al) interface states is neglected. In the case of the latter system, electrons coming from the high doped n-type Si substrate are accumulated at the c-Si(n)/a-SiC:H(Al) interface, leading into the SiC band edges movement to more negative potentials, yielding the diagram depicted in Fig. 3.11 where a large potential barrier between conduction bands (ΔE_{CB1}) and a negligible barrier between Si(n) and SiC(Al) valence bands (ΔE_{VB1}) is exhibited [103]. The final band structure will have a crucial impact on the charge transfer process at the semiconductor-electrolyte interface, under illumination and dark conditions. Different band diagram results for the case of p-type substrates, where holes coming from the p-type Si and SiC layers are prone to recombine with electrons from the conduction band. This electron charge transfer mechanism might be assisted by the donor-like surface states. The c-Si(p)/a-SiC:H(Al) interface is also depicted in Fig. 3.11.

3.2.2 Isotype and anisotype heterojunctions: role in PEC performance

Fig. 3.12 shows the LSV curves, in dark and illuminated conditions, for the a-SiC:H(Al) samples grown on p-type and n-type c-Si substrates, in as grown conditions. Since both a-SiC layers exhibit the same parameters (see Table. 2.3), the substantial differences observed in J_{ph} might be attributed to the participation of photogenerated carriers coming from the substrates, as will be discussed in the current section.

For the c-Si(n)/a-SiC:H(Al) system under illumination, and when an external negative bias is applied to the working electrode, the electrons from the a-SiC surface reduce protons in solution to produce hydrogen. However, it is less probable for the photogenerated electrons in the Si(n) to jump into SiC by a drift current due to the large barrier between conduction bands (ΔE_{CB1}), as depicted in Fig. 3.11. The unexpected substantial increment in dark current as higher negative potentials are applied, reflects that an accumulation region must be formed in the space charge in the vicinity of Si(n), causing the semiconductor electrode to behave as metal. For an in-detail explanation of this phenomenon see Fig. 1.9 in Sec. 1.2. The effect of dark current increment is depicted in Fig. 3.12. The evidence suggests that the space charge

Anisotype heterojunction: Si(n)-SiC(p):



Isotype heterojunction: p(Si)-p(SiC):

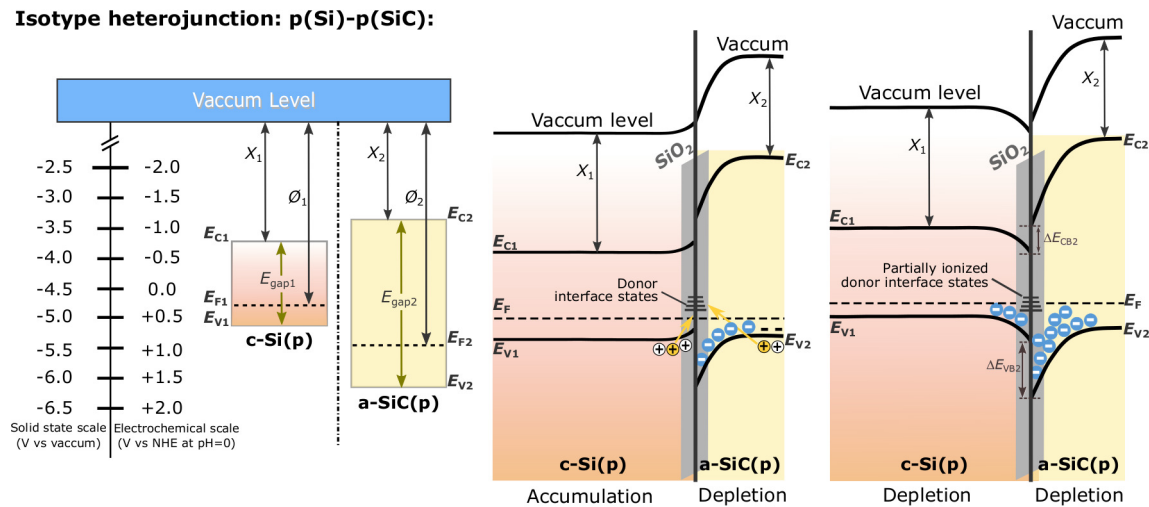


FIGURE 3.11: Anisotype c-Si(n)/a-SiC(Al) vs isotype c-Si(p)/a-SiC(Al) heterojunctions. Band diagrams of the Si and SiC semiconductors are shown with respect to the solid state and standard electrochemical scale. Electronic affinity values (χ) are constant, while work functions (ϕ) change with the level of impurities or dopant atoms. Presence of the native SiO_2 layer on the Si substrate adds donor-like behavior SS at the solid-solid interface. These SS play a crucial role in the formation of the space charge region on both sides of the junction. ΔE_{CB} and ΔE_{VB} represent the energy variation between the semiconductors band edges at the interface.

region of the a-SiC:H(Al) absorber layer must be extended throughout the whole layer reaching the n-type Si substrate. Hence, the applied negative potential may lead into a Fermi level that is moving in the n-type Si quasi-neutral region. Then, a forward bias condition would be determining the dark current behavior, as expected in metal electrodes.

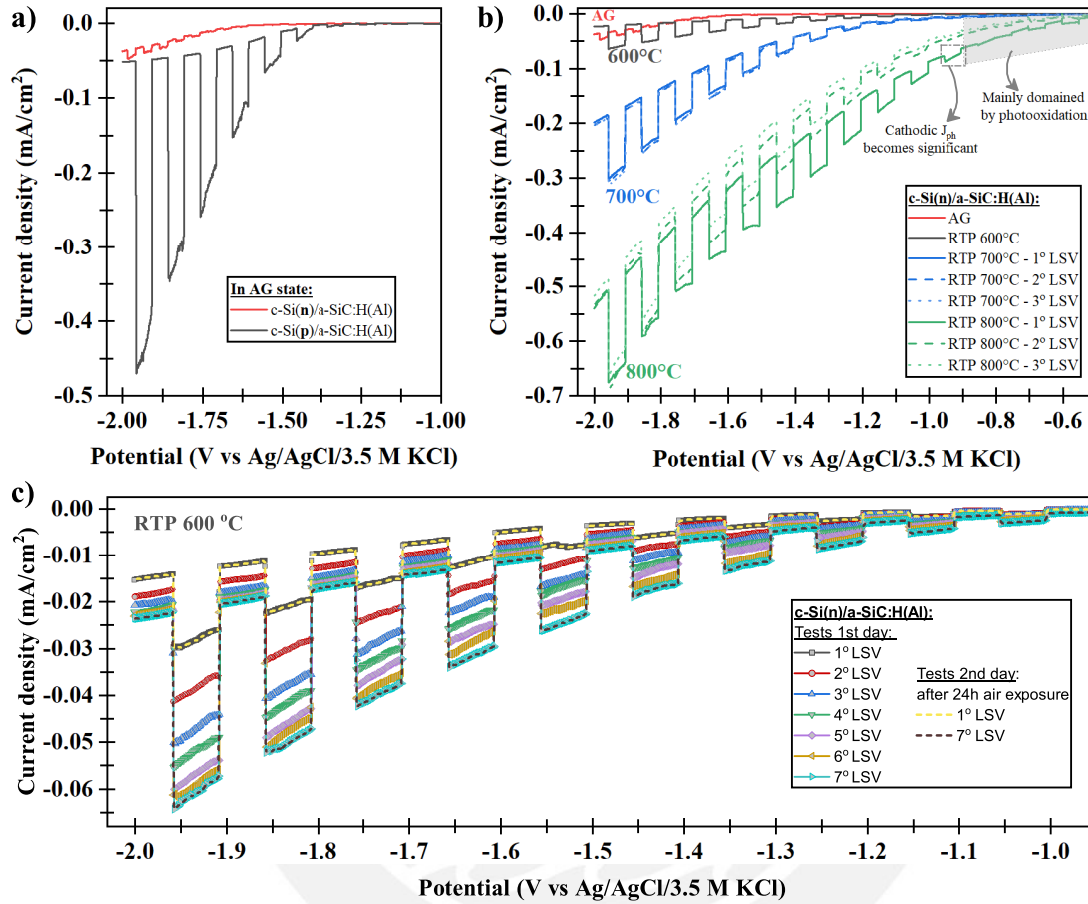


FIGURE 3.12: LSV curves: for the c-Si(n)/a-SiC:H(Al) and c-Si(p)/a-SiC:H(Al) systems in AG state (a). The c-Si(n)/a-SiC:H(Al) system after being subjected to isochronal annealing treatments at different temperatures. An in-sequence LSV tests reveal possible photocorrosion in the a-SiC thin film (b). The c-Si(n)/a-SiC:H(Al) system after annealed at 600 °C, in an in-sequence LSV test and at different times, after exposure to air (c). Tests were performed in H₂SO₄ (1 M)

The presence of high dark current implies that, despite the large barrier between Si and SiC conduction bands (ΔE_{CB1}), electrons might diffuse over the n-type depletion region. The phenomenon occurs due to, as forward bias is applied, the width of the space charge region becomes smaller. This favors the electron diffusion from the Si(n) to the a-SiC:H(Al) quasi-neutral region, and the hole diffusion from the a-SiC:H(Al) semiconductor to the Si(n) quasi-neutral region [104]. Therefore, diffusion current of minority carriers can not be compensated by the opposite drift current triggered from the space charge layer, i.e. diffusion overcomes drift current. Expressions for the electron and hole diffusion currents are shown in Eqs. 3.3 and 3.4, respectively [105]. To obtain these expressions, the analysis was simplified by assuming that a

graded junction, after subjecting the samples to annealing treatments, was reached. By this assumption, ΔE_C and ΔE_V become smooth transitions inside the depletion region, so that, the diffusion currents turn to be similar to a regular p-n junction.

$$j_n = \frac{q D_n n_i^2}{L_n N_D} \left[\exp\left(\frac{qV}{\kappa T}\right) - 1 \right]. \quad (3.3)$$

$$j_p = \frac{q D_p n_i^2}{L_p N_A} \left[\exp\left(\frac{qV}{\kappa T}\right) - 1 \right]. \quad (3.4)$$

Then, the total current is represented by Eq. 3.5. Where D is the diffusion coefficient, n_i , the intrinsic carrier density, L , the diffusion length of minority carriers, and N the doping concentration for the n-type (N_D) and p-type semiconductor (N_A).

$$j = j_n + j_p = \left(\frac{q D_n n_i^2}{L_n N_A} + \frac{q D_p n_i^2}{L_p N_D} \right) \left[\exp\left(\frac{qV}{\kappa T}\right) - 1 \right]. \quad (3.5)$$

Current density-potential curves shown in Fig. 3.12 suggest that the quasi-neutral region in a-SiC:H(Al) becomes narrower as the annealing temperature increases. The last assumption, considering the dark current increment upon each annealing step, along with the progressively a-SiC:H(Al) thickness shrinking, shown in Table. 3.2. Therefore, when a negative bias is applied to the working electrode in the darkness, majority carriers of the n-type Si substrate would take part by diffusion in the charge transfer kinetic mechanism at the a-SiC:H(Al)/electrolyte interface.

TABLE 3.2: a-SiC:H(Al) thickness variation (nm) with annealing treatment for the c-Si(n)/a-SiC:H(Al) system.

| System | Sample condition | | | |
|---------------------|------------------|--------|--------|--------|
| | As grown | 600 °C | 700 °C | 800 °C |
| c-Si(n)/a-SiC:H(Al) | 207 | 185 | 176 | 174 |

Fig. 3.12 shows that as the dark current increases with the annealing, the photocurrent also increases. The increase in the photocurrent is due to the electrons generated in the n-type Si substrate under the illumination condition, which diffuse after each annealing step, more easily towards the a-SiC:H(Al) surface. An energy band diagram for the a-SiC:H(Al)/electrolyte interface is depicted in Fig. 3.13 where the c-Si(n) substrate influence in the charge transfer kinetic mechanism at the surface is depicted under reverse and forward bias conditions. It is also reported that the increment in photocurrent with the dark current can be associated to the SiO₂ native layer reduction in the a-SiC:H(Al) surface, as will be discussed in section 3.3.

Another interesting feature to highlight in Fig. 3.12 is that the photocurrent tends to decrease after each LSV sequent test, reflecting the expected surface photo-oxidation of the a-SiC(Al) layer during measurements. This effect is triggered by the hole charge carrier generation upon illumination and is accentuated in the sample after being subjected to the 800 °C annealing step. Upon the 700 °C annealing step, J_{ph} maintains almost the same value in each LSV test. The J-V curve at the

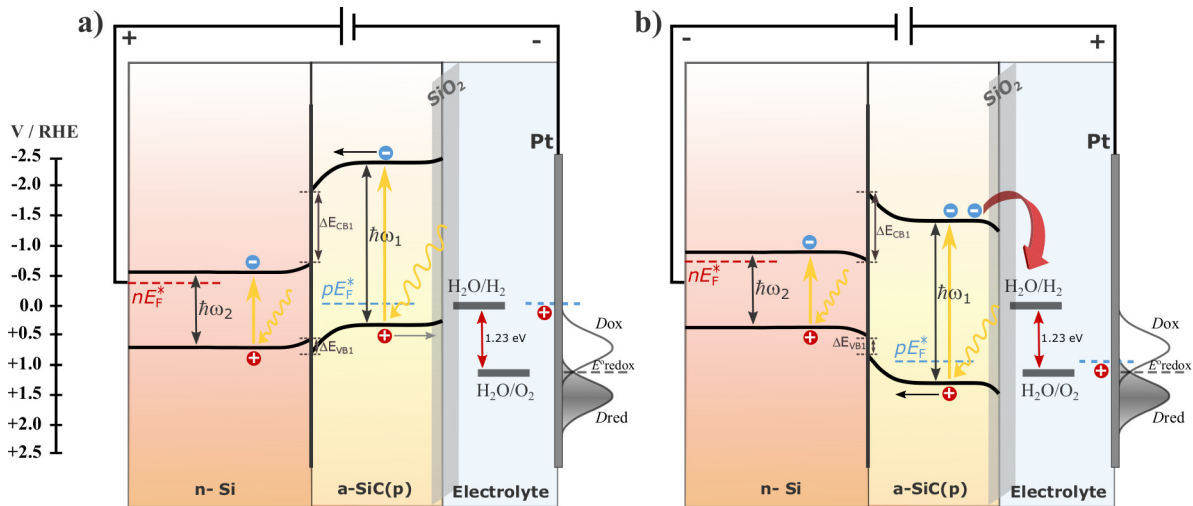


FIGURE 3.13: Energy band diagrams of PEC components: c-Si(n)/a-SiC:H(Al) photocathode, anode (Pt) and light illumination, at reverse (a) and forward (b) bias condition. nE_F^* and pE_F^* are the quasi-Fermi energy levels of electrons and holes, respectively. E_{redox}^0 corresponds to the standard redox potential for oxygen evolution reaction taking place in the Pt counter electrode, whose fluctuation distribution of energy levels are D_{red} and D_{ox} .

800 °C annealed sample shows that photo-oxidation may mainly occur between -0.5 and -0.9 V. Under this range of potential applied, a reverse bias condition, which is depicted in Fig. 3.13a, would take part in the Si(n)-SiC(Al) junction. That means, photogenerated holes from both layers, c-Si(n) and a-SiC:H(Al) would reach the a-SiC:H(Al) surface. In this case, since the barrier between valance bands is too low, photogenerated holes from c-Si(n) can easily jump into the a-SiC:H(p) by a drift current originated from the space charge region, which decreases with the potential sweep from reverse to forward bias. On the other hand, under the same conditions, electrons cannot be neither drifted nor diffused towards the surface to conduct the reduction reaction. The latter phenomenon occurs until the system reaches the forward bias condition depicted in Fig. 3.13b at ~ -0.9 V. In this case, photocurrent reduction is observed, from ~ -0.9 V to more negative potentials.

The sample subjected to 600 °C was also tested with LSV experiments carried out in sequence (Fig. 3.12). The progressive enhancement in current density observed in both conditions, darkness and illumination, is associated to a change in the semiconductor surface. Particularly, the increment in dark current is associated with the native SiO₂ surface layer reduction. Then, after air exposure during a 24 h period, SiO₂ regeneration would cause the current densities adopt their initial values. Although the difference in J_{ph} appears to be negligible between each LSV in-sequence test, an inertia effect is discarded. By the inertia effect, the potential at the WE surface tends to maintain when this is abruptly moved from one equilibrium condition to another one. Evidence of the SiO₂ surface layer reduction phenomenon will be discussed in section 3.3. Unlike the annealing processes at 700 and 800 °C, a forward bias condition during the whole linear sweep would explain the current density increase

behavior after annealing at 600 °C. In this case, the reduction of the SiO₂ layer would be only triggered by photogenerated electrons coming from the a-SiC:H(Al) absorber layer. This, due to the wide quasi-neutral region extension and the large potential barrier ΔE_{CB1} in the c-Si(n)/ a-SiC:H(Al) system, that restricts any electron diffusion from the c-Si(n) substrate towards the a-SiC:H(Al) layer.

3.2.3 Substrate influence by direct contact with the electrolyte

Substrate influence in current density performance was also evaluated in terms of structural growth factors of the thin films. Direct contact between the electrolyte and the Si substrate through cracks that might be originated in the a-SiC:H(Al) layer after annealing was discarded by SEM analysis. Fig. 3.14 shows the SEM cross-section images taken for the sample in as grown state and after being subjected to the 800 °C annealing process. Carbon and platinum layers were deposited over the a-SiC:H(Al) film to protect this for subsequent cross-section milling. A columnar structure of the a-SiC layer is observed for the sample after the annealing. It is also noticed in the same figure that these columnar clusters coincide with the morphology pattern observed in the top of the film. The columnar structure cannot be distinguished for the sample in as grown condition. Judging by this columnar-like features and the previously reported discussion on thermal-induced structural relaxation of the a-SiC:H matrix (see Sec. 3.1), it seems that carbon atomic diffusion towards the limit of the a-SiC:H(Al) columnar clusters might take place upon annealing. This would explain why these columnar structures are more detectable after annealing.

A substrate influence in current density response by shunting with the electrolyte is discarded. It is also noticed in Fig. 3.14, the thickness shrinking that takes place with the annealing treatment. The origin of the latter phenomenon is explained in Sec. 3.1.

3.2.4 Summary of Section 3.2

Substrate influence in the photoelectrochemical performance of a-SiC:H(Al) photocathodes was analyzed in terms of the photocurrent response, annealing treatments, and by varying the substrate conductivity type. It has been demonstrated that the phenomenon of the space charge region width exceeding the a-SiC:H(Al) thickness and reaching the substrate, is prone to take place in very thin a-SiC:H(Al) films, of approximately 170 nm thickness. The last finding considers an Al doping concentration of around 0.40 at %. A more detailed and systematic analysis should be performed to accurately determine the minimum a-SiC:H(Al) layer thickness in order to avoid influence from the substrate. Moreover, an additional chemical characterization technique, like Hall effect, is recommendable to perform to improve SCR width estimations, based on doping concentration values (see Eq. 1.7). As unexpected high dark current densities are observed for the a-SiC(p) layer, it is suggested that the majority charge carriers in the n-type Si substrate are playing a role in the electronic charge transfer at

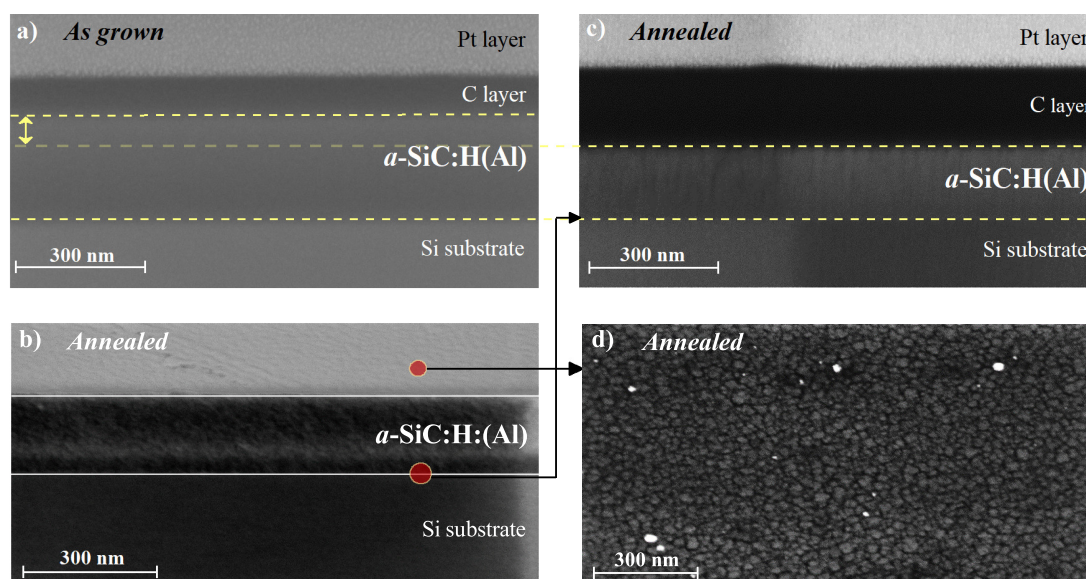


FIGURE 3.14: SEM images of c-Si/a-SiC:H(Al): Cross-section of the sample in As grown state (a) and after annealing at 800 °C (b). Cross-section of the at 800 °C annealed sample after cross-section milling by Focused Ion Beam (FIB). A columnar structure is observed (c). Top-section of the annealed sample at 800 °C (d). Carbon and platinum were deposited as protection layers for subsequent cross-section milling. The a-SiC:H(Al) film shrinking with annealing is highlighted.

the semiconductor-electrolyte interface. The latter effect was observed for the a-SiC sample with 175 nm thickness, after performing rapid thermal annealing processes at 700 and 800 °C. The phenomenon is intensified as the thickness of the a-SiC layer is progressively reduced with the annealing steps. The cathodic dark current is associated to a change in the photoelectrode surface. In general, dark currents indicate that electrons leaked to defects states or surface states in the bandgap [106]. Since it is known that the hydroxyl group terminations of the SiO₂ layer form an electronic state typically located within the semiconductor bandgap [102], the changes in the photoelectrode surface are associated to the native SiO₂ layer reduction. Thus, as the SiO₂ layer is reduced, the photocurrent increases, as noticed in Fig. 3.12 for the sample heated at 600 °C. Then, the small and decreasing photocurrent observed for the at 800 °C annealed sample, upon being subjected to in-sequence LSV tests, would be caused by the increase of the SiO₂ layer. This is in accordance to the charge transfer mechanism explained in Fig. 3.13. Finally, a substrate influence in current density response by shunting with the electrolyte was discarded by means of SEM-cross section analysis.

3.3 a-SiC:H(Al) surface states influence in water splitting reaction

In order to gain a better understanding about the intrinsic SiO₂ influence on the photocurrent response, and the role of surface states in the photoelectrochemical performance, electrochemical impedance spectroscopy measurements were carried out and will be discussed in this section. To perform these tests, ohmic contacts were necessary. Therefore, only a-SiC:H(Al) samples over p-type c-Si substrate were used at 600 °C annealed condition, at which ohmic contacts were achieved, as shown in Fig. 3.5. The parameters of these samples are shown in Table 2.1 (sample (b)). Likewise, steady-state condition tests, like LSV and Open Circuit Potential (OCP) were carried out to validate the data obtained by EIS. Structural, morphological and photoelectrochemical characterization of these samples are addressed in this section. Optical, electrical and vibrational characterization were discussed in Sec. 3.1.

3.3.1 Structural and morphological characterization

XRD diffractograms of the as grown and annealed sample (Fig. 3.15), do not show any sharp diffraction peak related to SiC crystalline phases. Therefore, after annealing at 600 °C, the SiC layer is still amorphous. The peak at $2\theta = 28^\circ$ and its shoulder at around 40° for the annealed sample, might indicate cluster formation of an amorphous carbon phase [57, 107]. The presence of this phase has been corroborated by Raman measurements, as depicted in Fig. 3.15.

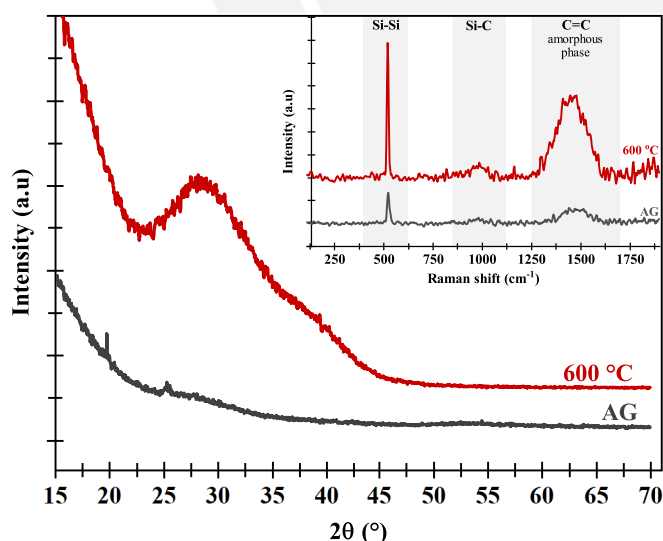


FIGURE 3.15: XRD patterns of Al doped a-SiC:H(Al) in as grown (AG) state and after annealing at 600 °C. Inset depicts the Raman spectra for both cases. An increment in the Si-Si, Si-C and C-C modes is detected after the heating process.

AFM images are shown in Fig. 3.16. There is no observed change in surface roughness for the sample after being photoelectrochemically tested. However, after annealing a roughness reduction from 1.04 to 0.35 nm in root-mean-square roughness R_q is observed.

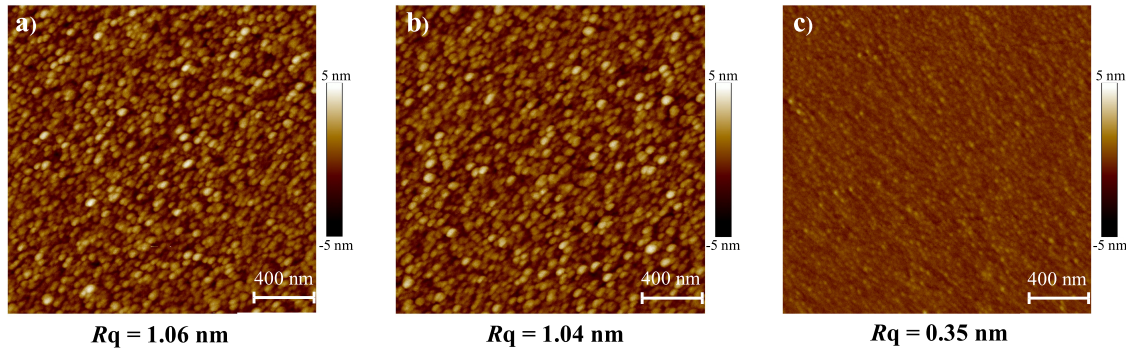


FIGURE 3.16: AFM images taken from c-Si(p)/a-SiC:H(Al) sample in as grown state before being photoelectrochemically tested (a), in as grown state after photoelectrochemical test (b) and after annealing treatment at 600 °C and photoelectrochemical test (c). Root-mean-squared roughness values R_q are shown below each image.

3.3.2 Photoelectrochemical characterization

All potential values in this section are indicated relative to the Ag/AgCl (3.5 M KCl) scale. Fig. 3.17 depicts the recorded J_{ph} for the as grown sample and for the sample after annealing. For the as grown sample, a cathodic photocurrent was not observed at 0 V. However, a starting anodic photocurrent takes place, probably originated from a hole charge carrier accumulation layer at this potential. As light-induced hole charge carriers cannot be efficiently extracted by the rear contact exhibiting Schottky-like behavior, these are accumulated in the vicinity of the space charge region and diffuse towards the surface giving rise to an oxidation reaction which results in the anodic photocurrent. For the annealed sample, a cathodic J_{ph} of -0.05 mA/cm^2 was obtained at -0.30 V . This value remains negligible compared to that observed at -1.75 V , which is around -17 mA/cm^2 .

Catalytic activity of the photocatalyst was measured by Tafel slope at low potentials, from 0 to -0.5 V . For the annealed sample, the abrupt increase of J_{ph} over this potential range reflects a considerable low Tafel slope of 16 mV/dec compared to the ideal one of 60 mV/dec expected for semiconductor photoelectrodes, according with the Shockley-Read recombination model [12]. Even when low Tafel slopes are widely acknowledged as an indicator of efficient electrocatalytic performance, the extremely low J_{ph} in the range of $400 \mu\text{A/cm}^2$ indicates a slow surface reaction kinetics at these potentials.

The electrode kinetics at higher current densities near the saturation point (-17 mA/cm^2 at -1.75 V) reveals a higher Tafel slope of 120 mV/dec (Fig. 3.17). This distinction is of relevant importance considering systems such as water electrolyzers where high current densities at minimum operational potentials are required for economic viability [108]. A parallel recombination in the semiconductor bulk via charge carrier traps and within the space charge region has been found to lead into a Tafel slope between 60 and 120 mV/dec [23, 109]. Therefore, the slope of 67 mV/dec observed in the as grown state, may be due to recombination processes in both regions. Thereby, inefficiently extracted photogenerated holes are accumulated between the

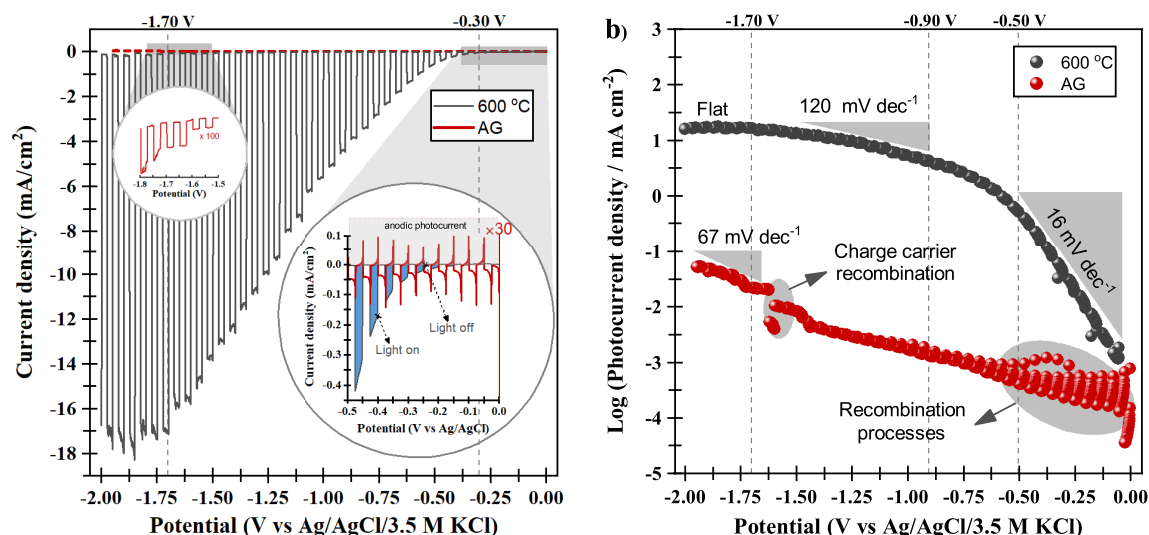


FIGURE 3.17: J-V polarization curves of c-Si(p)/a-SiC:H(Al) for the as grown (AG) and annealed sample. Inset depicts a magnification of current at low reverse bias. -0.3 V is the potential from which appreciable photocurrent is observed, whilst -1.7 V is the potential at which photocurrent saturation is observed (a). Steady-state polarization curves were obtained by taken logarithm of the photocurrents. The Tafel regions identified are indicated by the triangular features (b). Recombination processes are appreciated for the sample AG as an unstable current, at low and high bias. For the annealed sample: -0.5 V is the potential at which photocurrent starts to saturate, -0.9 V sets the potential at which a change in Tafel slope is detected. At -1.7 V, photocurrent reaches saturation (b). Tests were performed in H_2SO_4 (1 M).

bulk and the space charge region until their recombination takes place. This can be explained by the absence of ohmic contacts at the back of the system. Judging by the PEC cell depicted in Fig. 2.3, ohmic contact was only achieved with annealing at the top of the a-SiC:H(Al) absorber layer to isolate the latter from the Si substrate. On the other hand, for the annealed sample, it is interesting to note that the increase of the photocurrent density mainly occurs at low reverse bias potentials, from 0 to -0.5 V, and it starts to saturate at higher potentials, i.e. from -0.5 to -1.7 V. The effect is more clearly noticed in the logarithmic scale graph in Fig. 3.17b.

An increment in dark current for the annealed sample is observed in Fig. 3.17 at high reverse bias potentials. To better perceive this phenomenon, Fig. 3.18 shows a magnification of the J-V curve, in darkness and under illumination, for this sample.

As stated in Sec. 3.2, this variation in dark current is linked to the native SiO_2 surface layer reduction. Evidence of the SiO_2 reduction at the thermodynamic standard potential of -0.857 V vs. NHE (-1 V vs. Ag/AgCl 3.5 M KCl) [110] may explain recombination processes observed in dark conditions, specifically from -1 V to higher potential values. The origin of this recombination might be attributed to a competition between hydrogen reduction, under high reverse bias potentials in the dark, and the SiO_2 surface layer reduction. Furthermore, several studies have reported UV-induced degradation of SiO_2 [111–113], decreasing the overpotential at the interface. Overall, a considerable evolution in the current density recorded under illumination is observed at the same potential at which the dark current density increases as a result of the

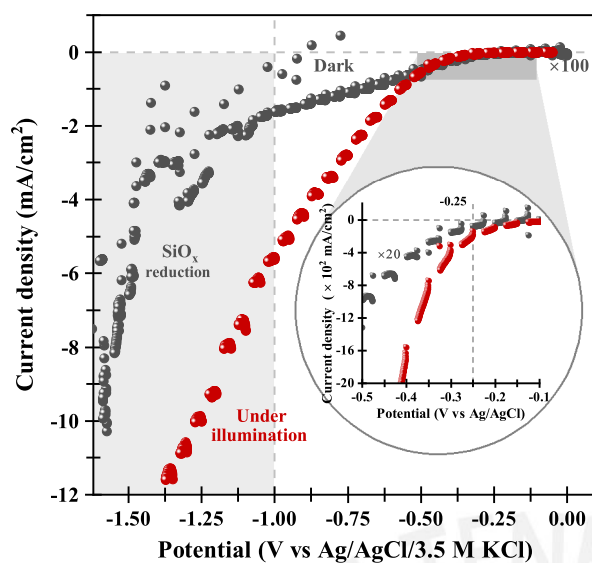


FIGURE 3.18: J-V current density for the 600 °C annealed c-Si(p)/a-SiC:H(Al) photocathode in the darkness (gray curve) and under illumination (red curve). There is a noticeable abrupt increase of the J_{ph} at the potential in which the dark current density starts to raise, at -0.25 V. Tests were performed in H_2SO_4 (1 M)

SiO_2 degradation. This last feature is observed in the inset of Fig. 3.18.

The design of passivation strategies to suppress photogenerated charge carriers recombination includes the use of SiO_2 or wide bandgap semiconductors or insulators, such as Al_2O_3 [114]. Thus, the passivation methods are typically addressed by depositing a few atomic layers of the oxide on photoelectrode surfaces. Moreover, in order to allow pinning of the band edges in an ideal situation, depicted in Fig. 3.19b, passivation layers may be ultrathin (1-2 nm) and dense [114]. Indeed, the compromise between the role of SiO_2 as a passivation layer and its performance as kinetic barrier at the semiconductor-electrolyte interface would be interesting to investigate further.

In Fig. 3.17, from -1.7 V onwards, photocurrent saturation at -17 mA/cm^2 is observed until -2 V. This photocurrent limiting value might be associated to mass transport limitations occurred at high cathodic potentials. Thus, a high kinetics for electron transfer is assumed to take part at the semiconductor-electrolyte interface. Therefore, we propose a charge transfer process taking place via tunneling. This implies the fluctuating energy level maximum point of the electrolyte species (H^+ / H_2) to be equal to the energy of the electron in the semiconductor [20]. This process is depicted in Fig. 3.19. For the system investigated, the ideal band edge pinned situation [18], would be reached upon application of potential values higher than -2.28 V. This applied potential value ($V_{ref} - V_{fb}$) corresponds to the semiconductor potential of -1.7 V.

The high J_{ph} achieved for the 600 °C annealed sample at the potential range from -1.7 to -2 V, suggests a charge transfer mechanism assisted by photogenerated carriers from the p-type Si substrate, as depicted in Fig. 3.19. For more detail of this phenomenon see Sec. 3.2. Thus, the achieved high electron transfer rate would be proportional to a high concentration of the relevant carrier in the semiconductor. In this case, for a p-type semiconductor device, i.e. c-Si(p)/a-SiC:H(Al), and under illumination conditions, photogenerated electrons constitute the relevant carriers. The effect of the semiconductor relevant carriers in the current system is established by Eq. 1.19 [20].

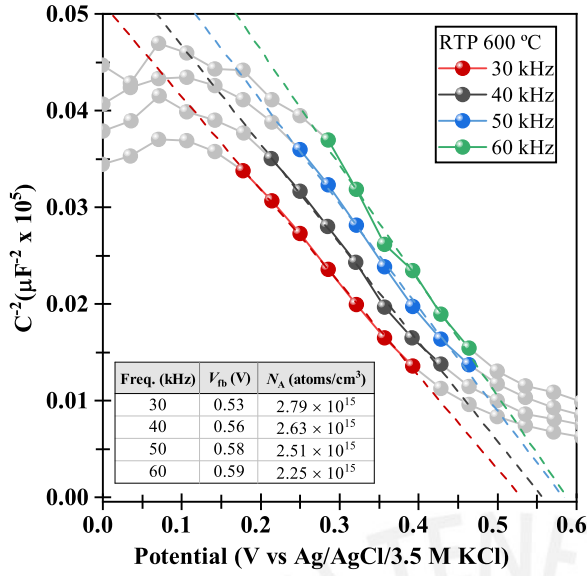


FIGURE 3.20: Mott-Schottky plots for the c-Si(p)/a-SiC:H(Al) heterojunction annealed at 600 °C at frequencies of 30, 40, 50 and 60 kHz. The inset table shows the flat band potential and carrier concentration values obtained from the linear fits performed for each frequency data. Tests were performed in H₂SO₄ (1 M)

literature [100], A is the exposed area of the photocathode, κ is the Boltzmann's constant and T the temperature of the electrolyte.

According to Eq. 3.6, the V_{fb} is ideally not dependent on the frequency applied in Mott-Schottky measurements. However, and particularly for amorphous semiconductors, the presence of surface states is known to cause frequency dispersion in Mott-Schottky plots [115]. This is due to the contributions from surface states capacitance (C_{SS}) and double-layer capacitance (C_{dl}) to the apparent value of the space charge region capacitance (C_{SC}). That is actually the behavior observed for the annealed c-Si(p)/a-SiC:H(Al) sample in Fig. 3.20. Although not well accentuated, two behaviors from this frequency dependent data can be distinguished. For high frequencies, i.e. 50 and 60 kHz, the fit lines seem to converge in a common intercept, and hence, yield what we believe a valid V_{fb} at around 0.58 V. For low frequencies, at 30 and 40 kHz, since slope values are quite similar compared with those observed at 50 and 60 kHz, a more reliable carrier concentration at around 2.7×10^{15} atoms/cm³ was extracted from these lower frequency data.

Slightly doped semiconductors are considered to vary in the range of 10^{16} to 10^{17} atoms/cm³ compared with those heavily doped which exhibit values at around 10^{18} and 10^{19} atoms/cm³ [18]. In the former case, the charge needed for Fermi level equilibration must come from deep inside the solid in contrast to the heavily doped case. Thus, the magnitude of the space charge layer width (W) will be larger. In general, typical W values range between 5-500 nm according to Eq. 1.7. Here, based on minimum and maximum N_A values calculated from Mott-Schottky plots, the space charge width was estimated to be in the range from 390 to 435 nm. This estimation was made taking 2.79×10^{15} and 2.25×10^{15} atoms/cm³ as N_A , with a $\epsilon_r = 13.12$ [116], $T = 304.7$ K and a space charge potential drop $\phi_{SC} = 0.27$ V. The value of ϕ_{SC} was calculated considering a V_{fb} of 0.57 V and an Open Circuit Potential in dark condition (OCP_{dark}) of 0.3 V, according to $V_{SC} = V_{fb} - OCP_{dark}$. Thus, for a low carrier concentration in the bulk of the semiconductor, the depletion of the entire

265 nm a-SiC:H(Al) annealed layer takes place at all applied potential values. This effect supports the charge transfer mechanism assisted by photogenerated carriers from the Si substrate, as depicted in Fig. 3.19.

Fig. 3.21 depicts a potential-independent space charge region capacitance (C_{SC}) for the annealed a-SiC:H(Al), which is a typical feature of insulators. The equivalent circuit model applied to extract these values is shown in the same figure. Nevertheless, the J-V curve obtained under illumination does not reflect such insulating behavior (Fig. 3.17). This evidence supports the theory of indirect charge transfer via SS reported initially by Salvador and Gutierrez and further studied for α -Fe₂O₃ photoanodes by Betoluzzi and Bisquert [53]. In regards to this theory, the density of surface states and its relative position respect to the band edges, determine whether these states are involved in equilibrium contact formation or charge transfer interface reactions [12].

To further understand the influence of SS in the photocurrent response, AC impedance spectroscopy characterization without illumination was performed to detect the frequency response of the c-Si(p)/a-SiC:H(p) heterojunction and identify its equivalent circuit. Nyquist plot fits were performed with a parallel connection in addition to the series connection settled between the SCR and double layer capacitances [117]. This parallel capacitance represents surface states capacitance which in principle appears in parallel with that of the SCR. The Nyquist plots are shown in Fig. 3.21.

In this study, constant phase elements (CPE) were used to represent non-ideal capacitances associated with the non-uniform distribution of current, due to the existence of the heterogeneous SiO₂ layer at the a-SiC:H(Al) surface. After performing circuit simulation by means of Multisim simulator program, values of potential drop (ϕ) were calculated for the SCR, double layer and surface states, treated at first approximation as a dielectric capacitance. By means of Multisim software, values of potential drop could be mathematically predicted, introducing the capacitances and resistances retrieved from the Nyquist plot fits, using the same equivalent circuit. Therefore, when the alternating voltage is applied with respect to the reference electrode, the potential difference is expected to be distributed over the space charge and double layers. However, because $C_{dl} \gg C_{SC}$, any change in applied bias falls linearly across the semiconductor SCR (see Fig. 3.21). For the c-Si(p)/a-SiC:H(Al) system, upon application of negative potentials respect to the V_{fb} (0.58 V), majority carrier density is depleted with respect to the bulk concentration. As a result, ϕ_{SC} increases towards more negative potentials in this region. In contrast, upon subjecting the electrode to anodic potentials, hole charge carrier density at the surface becomes much larger than those in the bulk and an accumulation layer appears.

The apparent potential drop depicted in Fig. 3.21 can be easily attributed to the variation of carrier concentration in SS, since these act as chemical instead of dielectric capacitances. In dielectric capacitances, the charge stored is associated to an electric field produced by spatial charge separation. This is the case for space charge and

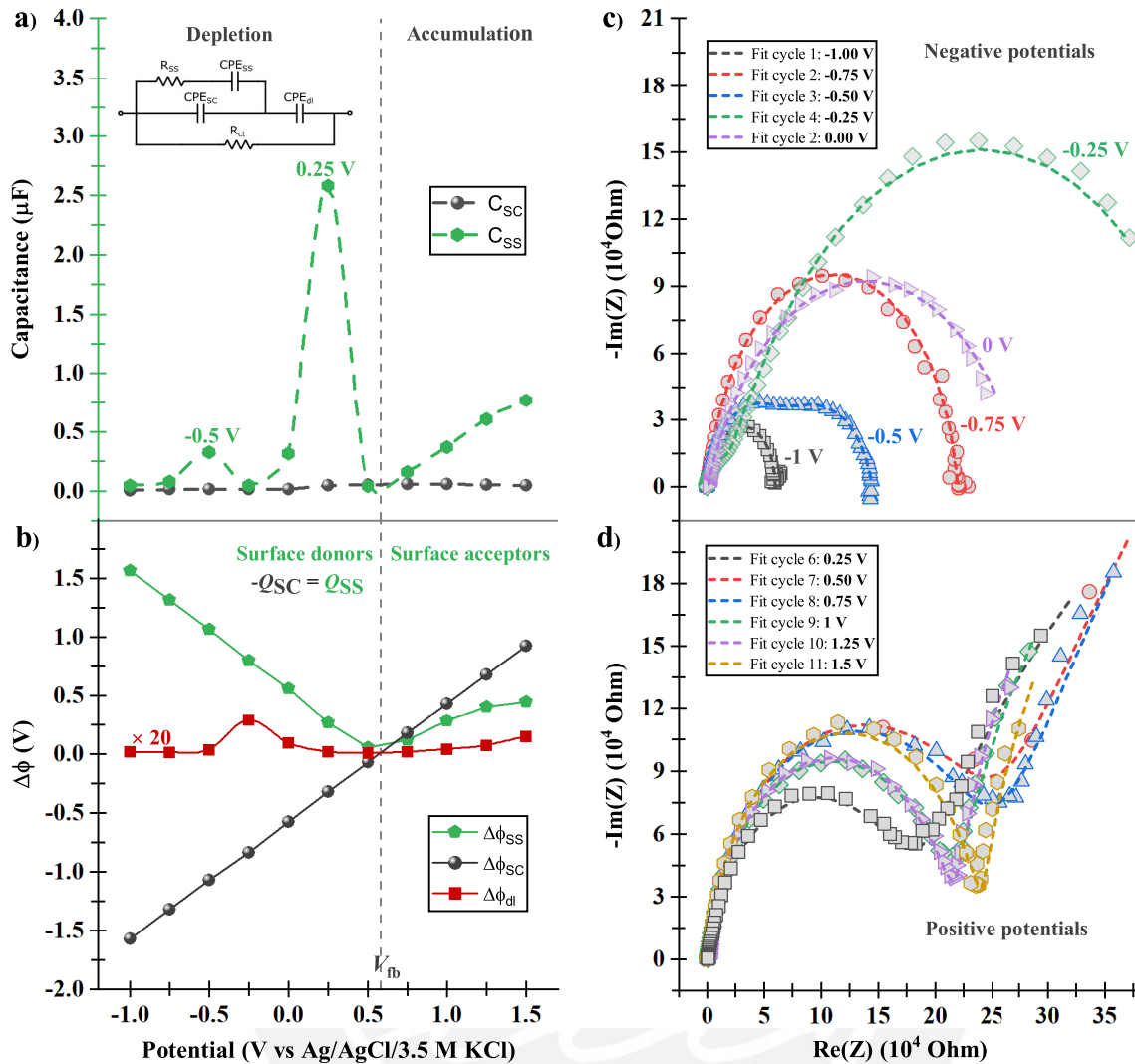


FIGURE 3.21: Simulated capacitance variation of the space charge and surface states upon applied potential for the annealed sample (a). Potential drop across the space charge, the double layer and surface states is shown. Negligible potential changing is observed across the double layer ($C_{dl} \gg C_{SC}$), whose potential values are scaled 20 times up for viewing purposes (b). Nyquist plot curves and fits (dash lines) obtained from EIS measurements at negative (c) and positive (d) potentials. Each cycle represents the impedance response of the c-Si(p)/a-SiC:H(Al)/1 M H_2SO_4 system at a certain applied voltage.

double layer capacitances [96]. On the other hand, in chemical capacitances, the charge storage associated mechanism is due to the variation of carrier concentration or chemical potential, as it is the case of surface states capacitances.

For this analysis, a frequency of 0.2 Hz in the circuit simulation program was chosen to have a time scale slow enough and hence to be able to see any possible effect of surface state capacitance in charge transfer processes. The depletion zone depicted in Fig. 3.21, shows that $\Delta\phi_{SS}$ is compensated in magnitude by a further potential drop inside the semiconductor (gray solid line) rising in the opposite polarization. These results can be interpreted according to the charge neutrality condition, namely that the charge of the surface states Q_{SS} is compensated by an opposite charge inside the

semiconductor layer. This condition is depicted in Figs. 3.22 and 3.23 for depletion and accumulation conditions of the SCR, respectively.

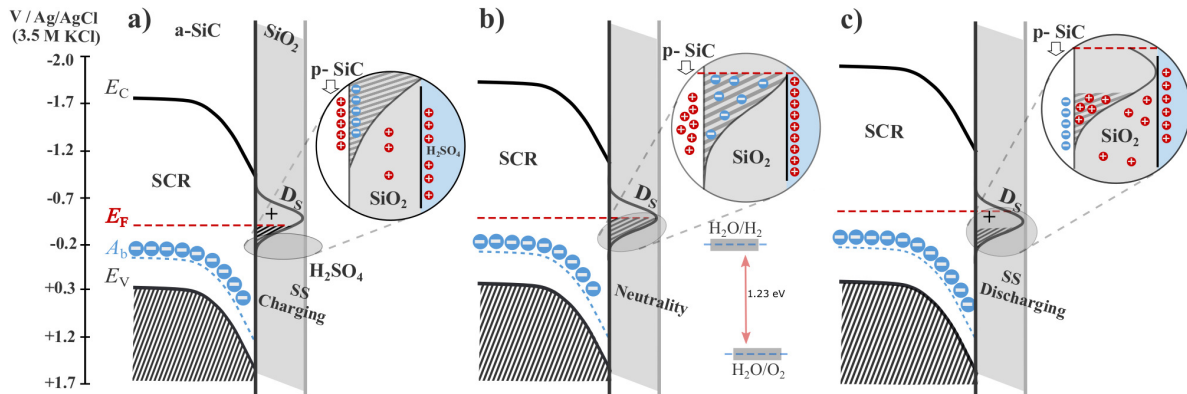


FIGURE 3.22: Energy band diagram and schematic of the c-Si(p)/a-SiC:H(Al)/SS/H₂SO₄ 1 M electrolyte junction in a state of depletion under donor-like surface states (D_S) charging (a), neutrality condition (b) and surface states discharging (c). Where E_C is the conduction band energy, E_V the valence band energy, E_F the Fermi level and A_b the bulk acceptors energy level. Thermodynamic redox potentials for hydrogen and oxygen evolution reactions, HER and OER respectively, are shown following the same energy scale. Note that thermodynamic requirement for HER is achieved as hydrogen redox potential is fixed below D_S .

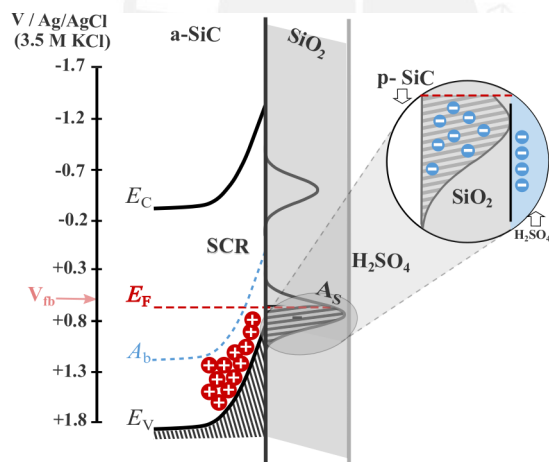


FIGURE 3.23: Energy band diagram and schematic of the c-Si(p)/a-SiC:H(Al)/SS/H₂SO₄ 1 M electrolyte junction in a state of accumulation. The presence of an accumulation layer in p-type semiconductors requires partially filled acceptor-like surface states (A_S).

| Surface states | Occupied | Empty |
|-----------------------------|----------|-------|
| Surface donors (D_S) | 0 | + |
| Surface acceptors (A_S) | - | 0 |

As shown in Fig. 3.22, under depletion condition, overall neutrality requires the presence of surface donors and therefore $Q_{SS} = -Q_{SC}$ [118]. On the contrary, the accumulation condition on p-type semiconductor, shown in Fig. 3.23, requires the presence of acceptor-like surface states, $-Q_{SS} = Q_{SC}$. Differences in the slope values of $\Delta\phi_{SS}$ curve, depicted in Fig. 3.21 are related to filling/unfilling of surface donors (in the depletion zone) and acceptors (in the accumulation zone). These differences would reflect the behavior of surface states preferably as charge donors (higher slope of potential drop vs applied potential) rather than acceptors (lower slope of potential

drop vs applied potential). Fortunately, this donor-like behavior is desirable for water splitting purposes using p-type semiconductors.

Charging/discharging phenomena of surface states and their electronic influence in the vicinity of the SCR are also depicted in Figs. 3.22 and 3.23. In these, the electronic influence of the electrolyte in the interface has been considered. Thus, owing to the equilibrium with the electrolyte, the neutrality condition of $Q_{SC} + Q_{SS} + Q_{dl} = 0$ is fulfilled. Magnifications illustrate the influence of donors (Fig. 3.22) and acceptors (Fig. 3.23) surface states in the SCR electronic behavior. Fig. 3.22 depicts this particular effect when the E_F crosses the SS energy band towards more negative potentials.

Fig. 3.24 shows the potential dependant surface state charge whose corresponding capacitance distributions are shown in Fig. 3.21. Q_{SS} values are obtained according to the relation $C_{SS} = Q_{SS}/\phi_{SC}$. For comparison, the Mott-Schottky curve is plotted in the same figure. Since Mott-Schottky plots are obtained using AC impedance techniques, surface states will have an impact on the observed response. A correlation between the discharging of donor-like surface states with the electron enhancement inside the SCR is clearly observed in the distribution centered at -0.5 V. Therefore, a negative slope in the Mott-Schottky plot appears in the potential range from -0.5 V to ~ -0.9 V where surface states are being discharged. The opposite is true for the SCR populated with holes from -0.5 to 0 V, where movement of majority carriers towards the SCR upon charging of surface states takes place, in such a case a positive slope in the Mott-Schottky plot is observed. These slope variations in the depletion zone are well correlated to the SS charging/discharging mechanisms depicted in Fig. 3.22. All the analyses have been performed considering the C_{SS} C_{dl} -dependence. By the latter, the potential drop across the double layer is altered when the E_F moves through the SS distribution towards more negative potentials, generating the electrons fill the defects states. A more rigorous analysis has been carried out solving the C_{SS} C_{dl} -dependence. This can be found elsewhere [119].

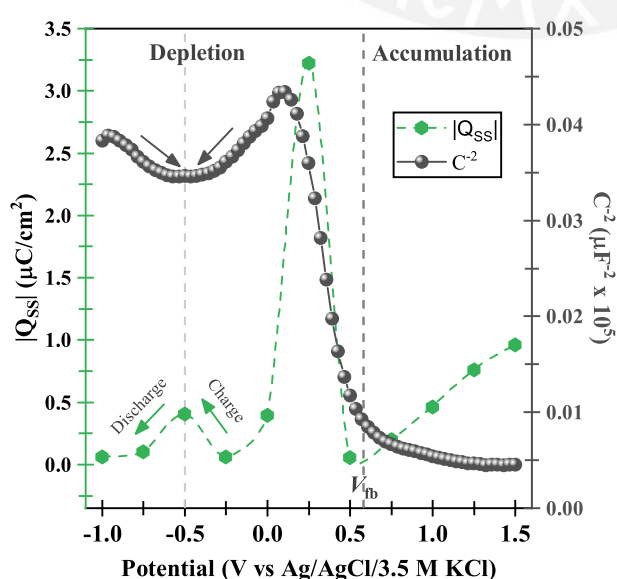


FIGURE 3.24: Mott-Schottky plot at frequency of 50 kHz and potential-dependent charge in surface states. Surface states charge distributions centered at -0.5 V and 0.25 V are correlated to the variation in the SCR electronic capacitance behavior observed in the Mott-Schottky plot.

The fluctuation in the semiconductor capacitance across the depletion region depicted in Fig. 3.24 is attributed to the surface state capacitance whose charge distribution extends around 0.25 V. This evidences a Fermi level alignment between the top a-SiC:H(Al) layer and surface states at its maximum point of energy distribution, which here has been found to be at ~ 0.25 V, as corroborated by Open Circuit Potential (OCP) measurements in the dark, at around 0.3 V (see next section). According to previous studies [52], the maximum energy value for intrinsic a-SiC surface states would be positioned around 0.29 V.

In agreement with Mott-Schottky results and photocurrent potential-dependent response, it is likely that accumulation of electrons at surface states in the a-SiC:H(Al) semiconductor is needed before a steady-state photocurrent for water reduction can be sustained. This first assumption is attributed to the location of surface states capacitance (starting at -0.25 V) that is slightly before the voltage at which appreciable photocurrent density appears (-0.3 V) (see Figs. 3.17 and 3.18).

In Fig. 3.17, note that once the Fermi level has crossed the whole energy band surface states centered at -0.5 V, i.e. at around -0.9 V according to Q_{SS} curve, depicted in Fig. 3.24, charge transfer to the solution becomes slower. This is reflected by a change in the Tafel slope, which rises up to 120 mV/dec. At this point, non-equilibrium or light induced formation and reoccupation of surface states may play a determining role in charge transfer processes and lead to a change in Q_{SS} and $\Delta\phi_{dl}$ as well. This effect is what is called kinetic charging of the semiconductor surface or dynamic Fermi level pinning, which exhibits a characteristic Tafel slope of ~ 120 mV/dec, due to the fact that the applied potential falls across the electrochemical double layer, by means of the SS charging [12, 20]. Here, this feature is observed in the potential range from -0.9 to -1.7 V. More explanation about this Fermi level pinning phenomenon can be found here [119].

Open Circuit Potential

OCP values were recorded in darkness (OCP_{dark}) and illumination (OCP_{light}) conditions for the a-SiC:H(Al) film. These are shown in Fig. 3.25. The measurements were performed at different times over the same sample, since day 1 to day 23, to assess the effect of the electrolyte in the stability of the thin film. The same 1 M H_2SO_4 electrolyte (pH=0) was used for all the OCP tests. Despite the day-to-day variation in the OCP_{dark} at the beginning of the test, almost the same V_{ph} is obtained in the range from 140 to 160 mV. For comparison purposes, OCP measurements were also carried out over the c-Si(p) substrate, exhibiting a lower V_{ph} between 40-70 mV. The variation in OCP_{dark} is attributed to surface changes due to light absorption. This suggests that time may be needed before the surface returns to its original state, in which the Fermi level lies at less positive potential [84]. The unstable signals observed for OCP_{light} might be due to different phenomena, such as electrolyte heating, i.e. according with Nernst equation (see Eq. 1.24), adsorption of electrolyte species at the electrode surface and/or corrosion reactions [84]. The electrolyte heating due to its

exposure to the AM 1.5 illumination is discarded to be the main source of OCP_{light} variation. This is because the liquid and back contact temperature data was recorded along the OCP tests, showing a different trend from the OCP_{light} , as observed in Fig. 3.25. After the last day test, a new solution of same H_2SO_4 concentration (1 M) was used to test the same a-SiC sample. Equal OCP_{dark} that the 1 day test was obtained, indicating that no variation takes place on the a-SiC:H(Al) layer surface after being exposed to the electrolyte. Therefore, corrosion reactions are also discarded to be responsible for the unstable OCP_{light} signal. Then, it seems that semiconductor SCR condition, play a crucial role in the OCP_{light} signal instability, as depicted in graphs I-III of Fig. 3.25.

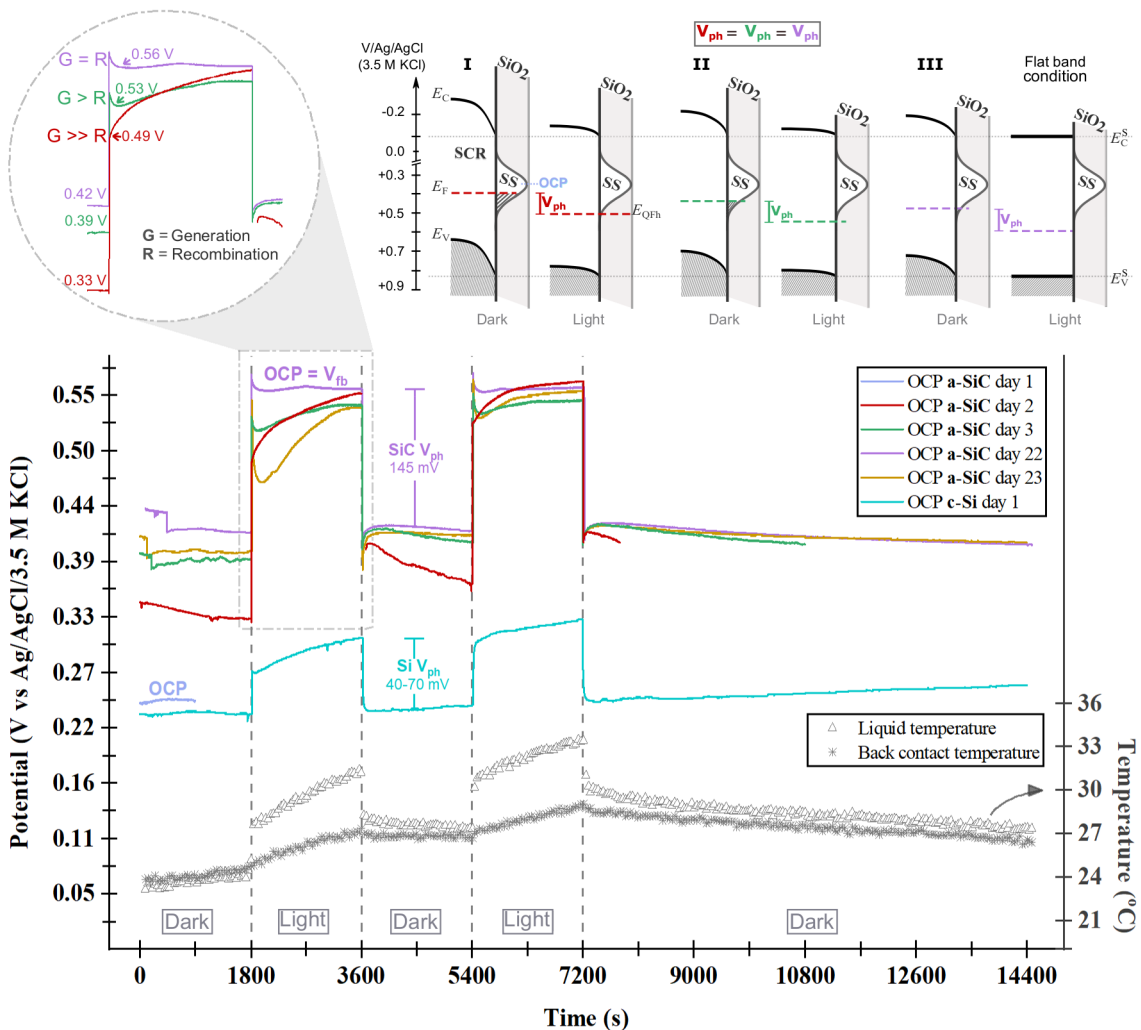


FIGURE 3.25: OCP in-sequence tests for the a-SiC:H(Al) layer. Measurements were performed in different times using the same 1 M H_2SO_4 electrolyte. For comparison purposes, V_{ph} values for a-SiC:H(Al) and the c-Si(p) substrate are shown. Temperature was recorded during the whole test, inside the electrolyte and at the back contact zone. No similar trend is observed between the temperature variation and the OCP signal. Then, instability in the OCP is associated to semiconductor conditions which are depicted in the band diagrams.

The OCP under illumination can be used to estimate the V_{fb} if the light intensity is sufficiently high to completely remove the pre-existing band bending at the surface

and the material does not exhibit very fast carrier recombination rates [84]. Typically, an OCP vs. light intensity plot is recorded to provide the best method for V_{fb} estimation. Here, the same light intensity was used for every OCP test. This intensity resulted to be high enough to fully flatten the band and saturates the OCP_{light} at day 22 of test, as it is observed in Fig. 3.25. The same effect did not occur in the previous days tests. The condition detected in day 22 for the OCP_{light} is termed photostationary condition [12]. Under this situation of steady illumination at open circuit, the excitation of electron and hole pairs (G) is balanced by their recombination (R). Then, $G = R$ under photostationary stay. This case is reached under the flat band condition, since there is no space charge that can efficiently separate photogenerated electrons from holes and thus, reduce recombination rates. At this point, R becomes as high as G and the stationary stay is achieved, giving a zero net current flow across the interface. On the other hand, R adopts lower values under reverse bias conditions, as depicted in cases I and II of Fig. 3.25. In both cases, the pre-existing band bending reduces the probability of recombination and thus, for case I, exhibiting lower recombination rate than case II, $G \gg R$ and the OCP_{light} moves abruptly towards more positive potentials as the photocarrier generation rate substantially overcomes their annihilation rate. Then, for case II, where $G > R$, a softer OCP_{light} variation in time is observed. Finally, the case III in the same figure, depicts the flat band condition where the OCP_{light} is equal to the V_{fb} , which is around 0.56 V. This V_{fb} value coincides with the one retrieved by Mott-Schottky technique (see Fig. 3.20).

Any change in the potential across the Helmholtz layer (more specifically, in the inner Helmholtz layer) due to changes in the semiconductor surface, is directly reflected in the V_{fb} . The phenomenon is known as unpinning of the semiconductor band edges or Fermi level pinning, while no changing in the Schottky barrier height occurs [20]. As the flat band condition was only observed in one of the OCP_{light} tests for the same sample, electrolyte and illumination intensity, the band edge unpinning would not be occurring in this system, as depicted in the band diagrams of Fig. 3.25. Indeed, the flat band condition had been expected to take place in all the OCP_{light} tests, reaching different V_{fb} values under photostationary condition. Consequently, it might be the drop of the Fermi level across the charged surface states distribution, what would be taking place after a sample light exposure, and not a band edge movement. This would occur in the potential range from 0 to 0.5 V, in which the SS distribution spreads, as depicted in Fig. 3.25. When as a result of the Fermi level drop, this ends in an energy outside the SS distribution, i.e. higher than 0.5 V, moving of the semiconductor band edges would take place. A new equilibrium condition, depicted in Fig. 3.26 might be reached. This situation was observed in day 23, where the OCP_{dark} stopped increasing and returned to less positive potential. Here, the V_{ph} generated remains the same. However, this decreases dramatically due to recombination processes taking place with the promotion of electrons in the E_C upon illumination. This occurs due to the E_C now is closer in energy to the SS, which mainly act as electron acceptors when it is empty [118]. The initial V_{ph} value is reached again

after ~ 28 min, when a new photostationary condition is observed, according to Fig. 3.25. In-detail surface spectroscopic studies, like X-Ray photoelectron spectroscopy, need to be performed to corroborate the information gathered so far about the stability of the a-SiC:H(Al) photocathode under darkness and illumination conditions.

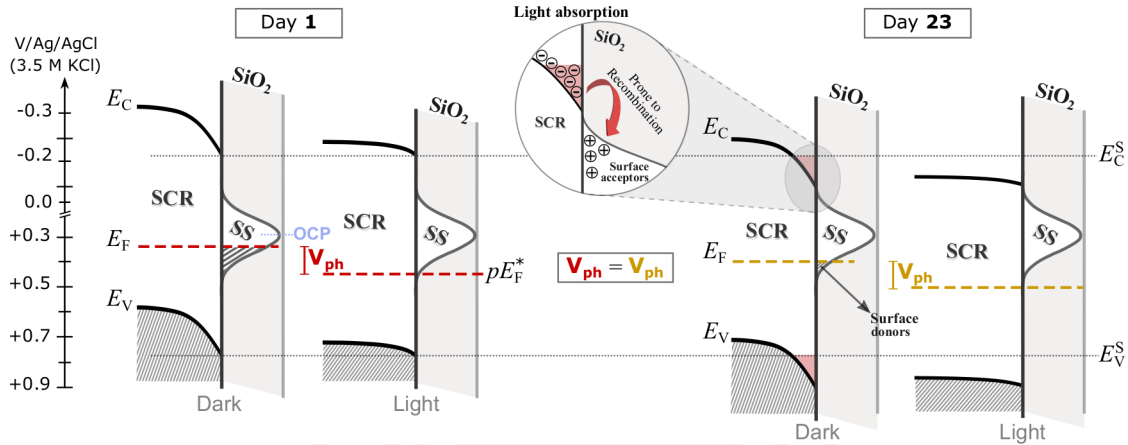


FIGURE 3.26: The band diagrams that illustrate the electrode surface conditions proposed according to the OCP in-sequence tests for the a-SiC:H(Al) layer. OCP measurements were performed in different times using the same 1 M H_2SO_4 electrolyte. The conditions depicted are for day 1 and day 23. Recombination processes prone to take place due to the unpinning of the band edges are highlighted for day 23.

3.3.3 Summary of Section 3.3

A systematic study of the photoelectrochemical behavior of c-Si(p)/a-SiC:H(Al) heterojunction was carried out. The surface smoothing taking place at 600°C could have led into homogeneous currents as well as into a depletion of recombination centers at the surface. Since root-mean-square roughness R_q value for the annealed sample was lower than the as grown one, and the electrolyte did not induce further changes in the surface morphology, then the increase in photocurrent for the annealed sample is not associated to an increment in the effective surface area. Localized surface states would take part in a desirable mechanism of indirect electron charge transfer to the electrolyte, and thus, conduct hydrogen evolution reaction. Concerning the SiO_2 native layer, our findings suggest that the SiO_2 layer reduction triggers a favorable semiconductor-electrolyte interface. This interface exhibits less overpotential barriers which promotes photocurrent generation. Here, the SiO_2 native layer of a-SiC:H(Al) was not actively removed. Thus, we believe that the annealing-induced abrupt enhancement in the PEC performance of the c-Si(p)/a-SiC:H(Al) photocathode is probably associated to the obtained ohmic contacts as well as the passivation effect caused by the native oxide layer [19, 103, 120]. Additional studies, like X-Ray photoelectron spectroscopy (XPS) or Auger electron spectroscopy (AES) are necessary to assess the influence of annealing treatments on the a-SiC:H(p) semiconductor surface.

Chapter 4

Conclusions

By bandgap engineering, it was found that a-SiC samples without hydrogen and with 1.57×10^{21} atoms of H/cm³ exhibit suitable bandgaps to perform water splitting reaction, i.e. between 2.2 and 2.7 eV. The bandgap obtained from the Band fluctuations model $E_{B,F}$ resulted more reliable than the E_{Tauc} and E_{04} conventional models, since it considers the disorder-induced tail states that are predominant in amorphous materials. It was concluded that these states would increase with the formation of the amorphous C=C phase which takes place during the heating processes. This behavior was not detected from the E_{Tauc} nor the E_{04} energy bandgaps (Sec. 3.1).

An improvement in the electrical performance of the c-Si(p)/a-SiC:H(Al) photocathode was achieved with the annealing at 600 °C for 10 minutes holding time, upon which, ohmic contacts were obtained. However, compromising the hydrogen passivation and the thickness of the a-SiC:H(Al) top absorber layer. Here, the thickness was shrinking by ~ 50 nm and the $E_{B,F}$ obtained was 2.76 eV. On the other hand, a more suitable $E_{B,F}$ for PEC water splitting was reached with the annealing at 200 °C, i.e. 2.55 eV. Here, hydrogen passivation and a-SiC:H(Al) thickness remained almost unaltered. Nevertheless, no ohmic behavior of the contacts were achieved at this temperature (Sec. 3.1). More studies need to be performed to evaluate how the thermally-induced thickness shrinking would affect the photoelectrochemical a-SiC:H(Al) performance, as well as to find a compromise between good hydrogen passivation strategies and electrical features.

It has been demonstrated that a space charge region extension beyond the at 600 °C annealed a-SiC:H(Al) layer (230 nm thickness) is achieved with relatively low carrier densities, between $2.2 - 2.8 \times 10^{15}$ atoms/cm³ (~ 0.3 at% Al), and consequently, film thicknesses ≤ 435 nm. For the latter estimation, a relative permittivity value $\epsilon_r = 13.12$ was used. This value was extrapolated from literature (Sec. 3.2). Therefore, a charge transfer mechanism supported by carriers from the substrate would play a role in the hydrogen reduction kinetics at the a-SiC:H(Al)-electrolyte interface.

Higher doping concentrations, of around 0.4 at% Al, would reduce the space charge region width, and thus, limit the a-SiC(Al) layer thickness to lower values in order to not to have influence from the substrate in the photocurrent response. In

this study, for the c-Si(n)/a-SiC:H(Al) system, a 170 nm a-SiC thickness would be low enough to detect participation of the Si(n) substrate photogenerated carriers in the charge transfer kinetics. To further validate this data, different a-SiC:H(Al) thin-film thicknesses should be assessed in c-Si(p)/a-SiC:H(Al) and c-Si(n)/a-SiC:H(Al) systems having the ohmic contact at the back part, i.e. on the substrate side (Sec. 3.2).

Following the substrate charge transfer assistance assumption, photogenerated carriers coming from the c-Si substrate might take part in the reduction and oxidation processes of the native SiO₂ and a-SiC(Al) layers, respectively, and both taking place at the top of the a-SiC film. The SiO₂ reduction is mainly attributed to the dark current variation observed at the potential at which the reaction is thermodynamically feasible, i.e. at -1 V vs Ag/AgCl/3.5 M KCl. Additionally, an abrupt increase in the photocurrent density was observed at the potential at which the dark current density starts to raise. This is attributed to the already reported SiO₂ UV-induced degradation, which would decrease the overpotential at the interface (Sec. 3.3).

Presence of surface states would play a crucial role in the charge transfer mechanism at the semiconductor-electrolyte interface. Two surface states energy distributions were retrieved from EIS experiments. The first one, spreading in the potential range from -0.25 to ~-0.9 V vs Ag/AgCl/3.5 M KCl, would participate in an indirect electron transfer mechanism to conduct the hydrogen evolution reaction. Then, it is likely that an accumulation of electrons at the surface states in the a-SiC:H(Al) semiconductor is needed before a steady state photocurrent for water reduction can be sustained. This assumption is associated to the location of surface states capacitance that is slightly before the voltage at which appreciable photocurrent density appears. On the other hand, the second surface states distribution, covering the potential range from 0.5 to -0.25 V vs Ag/AgCl/3.5 M KCl, would set the OCP value at the dark while limiting the maximum photovoltage achievable, i.e. $V_{fb} - OCP = 0.56 - 0.25 = 0.31$ V vs Ag/AgCl/3.5 M KCl (Sec. 3.3).

Appendix A

Seminars and publications

Seminars:

- 2018- Peruvian Workshop on Solar Energy (JOPES), Poster
- 2019- Peruvian Workshop on Solar Energy (JOPES), Talk
- 2019 Fall Meeting- European Materials Research Society (EMRS), Poster
- 2020 Fall Meeting- European Materials Research Society (EMRS), Talk

Publications:

- MdC. Mejia et al. "Analysis of the physical and photoelectrochemical properties of c-Si(p)/a-SiC:H(p) photocathodes for solar water splitting", J. Phys. D: Appl. Phys. **54**, 195101 (2021). <https://doi.org/10.1088/1361-6463/abdb69>.
- MdC. Mejia et al. "Bandgap engineering of hydrogenated a-SiC:H thin films for photoelectrochemical water splitting applications", J. Phys. D: Appl. Phys. **54**, 085108 (2021). <https://doi.org/10.1088/1361-6463/abc77a>.
- MdC. Mejia et al. "Localized surface states influence in the photoelectrocatalytic performance of Al doped a-SiC:H based photocathodes", Mater. Sci. Semicond. Process. **143**, 106474 (2022). <https://doi.org/10.1016/j.mssp.2022.106474>.

Bibliography

- [1] N. Greenwood and A. Earnshaw. *Chemistry of the Elements (2nd ed.)* ISBN: 978-0-08-037941-8.
- [2] L. Han et al. "Gradient dopant profiling and spectral utilization of monolithic thin-film silicon photoelectrochemical tandem devices for solar water splitting". In: *Journal of Materials Chemistry A* 3.8 (2015), pp. 4155–4162. ISSN: 20507496. DOI: [10.1039/c4ta05523c](https://doi.org/10.1039/c4ta05523c).
- [3] C. Gueymard, D. Myers, and K. Emery. "Proposed reference irradiance spectra for solar energy systems testing". In: *Solar Energy* 73 (2002), 443–467.
- [4] Feng Zhu et al. "Amorphous Silicon Carbide Photoelectrode for Hydrogen Production from Water using Sunlight". In: *Solar Energy*. Ed. by Radu D. InTech, Feb. 1, 2010. ISBN: 978-953-307-052-0. DOI: [10.5772/8074](https://doi.org/10.5772/8074). URL: <http://www.intechopen.com/books/solar-energy/amorphous-silicon-carbide-photoelectrode-for-hydrogen-production-from-water-using-sunlight> (visited on 10/17/2022).
- [5] Brian J. Simonds et al. "Defects in amorphous silicon carbide and their relation to solar cell device performance". In: 7409 (2009), pp. 740912–740912–7. DOI: [10.1117/12.826451](https://doi.org/10.1117/12.826451). URL: <http://proceedings.spiedigitallibrary.org/proceeding.aspx?articleid=1340411>.
- [6] P. A. Ivanov et al. "Deep surface states on the interface between SiC and its native thermal oxide". In: *Technical Physics Letters* 23.10 (1997), pp. 798–800. ISSN: 10637850. DOI: [10.1134/1.1261806](https://doi.org/10.1134/1.1261806).
- [7] Craig A. Grimes, Oomman K. Varghese, and Sudhir Ranjan. *Light, water, hydrogen: The solar generation of hydrogen by water photoelectrolysis*. 2008, pp. 1–546. ISBN: 9780387331980. DOI: [10.1007/978-0-387-68238-9](https://doi.org/10.1007/978-0-387-68238-9).
- [8] W-H. Cheng et al. "Monolithic Photoelectrochemical Device for Direct Water Splitting with 19% Efficiency". In: *ACS Energy Letters* 3.8 (2018), pp. 1795–1800. DOI: [10.1021/acsenerylett.8b00920](https://doi.org/10.1021/acsenerylett.8b00920).
- [9] J. Gao et al. "Solar Water Splitting with Perovskite/Silicon Tandem Cell and TiC-Supported Pt Nanocluster Electrocatalyst". In: *Joule* 3.12 (2019), pp. 2930–2941. ISSN: 25424351. DOI: [10.1016/j.joule.2019.10.002](https://doi.org/10.1016/j.joule.2019.10.002).

- [10] P. Varadhan et al. "An efficient and stable photoelectrochemical system with 9% solar-to-hydrogen conversion efficiency via InGaP/GaAs double junction". In: *Nature Communications* 10.1 (2019), pp. 1–9. ISSN: 20411723. DOI: [10.1038/s41467-019-12977-x](https://doi.org/10.1038/s41467-019-12977-x).
- [11] T. J. Jacobsson et al. "A monolithic device for solar water splitting based on series interconnected thin film absorbers reaching over 10% solar-to-hydrogen efficiency". In: *Energy and Environmental Science* 6.12 (2013), pp. 3676–3683. ISSN: 17545692. DOI: [10.1039/c3ee42519c](https://doi.org/10.1039/c3ee42519c).
- [12] Sixto Gim et al. *Photoelectrochemical Solar Fuel Production*. 2016, p. 574. ISBN: 9783319296395. DOI: [10.1007/978-3-319-29641-8](https://doi.org/10.1007/978-3-319-29641-8).
- [13] Di. Xu, L. Dong, and J. Ren. "Introduction of Hydrogen Routines". In: *Hydrogen Economy: Supply Chain, Life Cycle Analysis and Energy Transition for Sustainability* (2017), pp. 35–54. DOI: [10.1016/B978-0-12-811132-1.00002-X](https://doi.org/10.1016/B978-0-12-811132-1.00002-X).
- [14] *Powering the planet: Chemical challenges in solar energy utilization (Proceedings of the National Academy of Science of the United States of America)*. Vol. 104. 50. National Academy of Sciences, Dec. 2007, p. 20142. DOI: [10.1073/pnas.0710559104](https://doi.org/10.1073/pnas.0710559104).
- [15] C. Cheng et al. "Strategies for improving photoelectrochemical water splitting performance of Si-based electrodes". In: *Energy Science & Engineering* 10.4 (Apr. 2022), pp. 1526–1543. ISSN: 2050-0505, 2050-0505. DOI: [10.1002/ese3.1087](https://doi.org/10.1002/ese3.1087). URL: <https://onlinelibrary.wiley.com/doi/10.1002/ese3.1087> (visited on 10/18/2022).
- [16] T. Lopes et al. "Characterization of photoelectrochemical cells for water splitting by electrochemical impedance spectroscopy". In: *International Journal of Hydrogen Energy* 35.20 (2010), pp. 11601–11608. ISSN: 03603199. DOI: [10.1016/j.ijhydene.2010.04.001](https://doi.org/10.1016/j.ijhydene.2010.04.001).
- [17] Masakazu Sugiyama, Katsushi Fujii, and Shinichiro Nakamura. *Solar to Chemical Energy Conversion: Theory and Application*. Vol. 32. Jan. 2016, pp. IX, 489. ISBN: 978-3-319-25398-5. DOI: [10.1007/978-3-319-25400-5](https://doi.org/10.1007/978-3-319-25400-5).
- [18] *Encyclopedia of Electrochemistry, Vol. 6 (Semiconductor Electrodes and Photoelectrochemistry)*. 2007, pp. 1–51. ISBN: 978-3-527-30398-4. DOI: [10.1002/9783527610426.bard060001](https://doi.org/10.1002/9783527610426.bard060001).
- [19] Intergovernmental Panel on Climate Change. "Summary for Policymakers". In: *Climate Change 2013 – The Physical Science Basis: Working Group I Contribution to the Fifth Assessment Report of the Intergovernmental Panel on Climate Change*. Cambridge University Press, 2014, 1–30. DOI: [10.1017/CB09781107415324.004](https://doi.org/10.1017/CB09781107415324.004).

- [20] Roel Van De Krol and Michael Grätzel. *Photoelectrochemical Hydrogen Production*. Ed. by Roel Van De Krol and Michael Grätzel. Cambridge, Massachusetts: Springer New York Dordrecht Heidelberg London Library, 2012, p. 321. ISBN: 978-1-4614-8297-0. DOI: [10.1007/978-1-4614-1380-6](https://doi.org/10.1007/978-1-4614-1380-6).
- [21] R. M. Navarro Yerga et al. "Chapter 3 - Hydrogen Production from Water Splitting Using Photo-Semiconductor Catalysts". In: *Renewable Hydrogen Technologies*. Ed. by Luis M. Gandía, Gurutze Arzamendi, and Pedro M. Diéguez. Amsterdam: Elsevier, 2013, pp. 43–61. ISBN: 978-0-444-56352-1. DOI: <https://doi.org/10.1016/B978-0-444-56352-1.00003-9>.
- [22] Blaise A. Pinaud et al. "Technical and economic feasibility of centralized facilities for solar hydrogen production via photocatalysis and photoelectrochemistry". In: *Energy and Environmental Science* 6.7 (2013), pp. 1983–2002. ISSN: 17545692. DOI: [10.1039/c3ee40831k](https://doi.org/10.1039/c3ee40831k).
- [23] Rüdiger Memming. *Principles of Semiconductor Physics*. John Wiley & Sons, Ltd, 2015, p. 465. ISBN: 9783527688685. DOI: <https://doi.org/10.1002/9783527688685.ch1>.
- [24] R. A. Marcus. "On the theory of oxidation-reduction reactions involving electron transfer. I". In: *The Journal of Chemical Physics* 24.5 (1956), pp. 966–978. ISSN: 00219606. DOI: [10.1063/1.1742723](https://doi.org/10.1063/1.1742723).
- [25] R. A. Marcus. "Chemical and Electrochemical electron-transfer theory". In: *Annual Review of Physical Chemistry* 15.1 (1964), pp. 155–196. DOI: [10.1146/annurev.pc.15.100164.001103](https://doi.org/10.1146/annurev.pc.15.100164.001103).
- [26] H. Gerischer. "Charge transfer processes at semiconductor-electrolyte interfaces in connection with problems of catalysis". In: *Surface Science* 18.1 (1969), pp. 97–122. ISSN: 00396028. DOI: [10.1016/0039-6028\(69\)90269-6](https://doi.org/10.1016/0039-6028(69)90269-6).
- [27] J. O. M. Bockris. "Kinetics of activation controlled consecutive electrochemical reactions: Anodic evolution of oxygen". In: *The Journal of Chemical Physics* 24.4 (1956), pp. 817–827. ISSN: 00219606. DOI: [10.1063/1.1742616](https://doi.org/10.1063/1.1742616).
- [28] B. Klahr et al. "Electrochemical and photoelectrochemical investigation of water oxidation with hematite electrodes". In: *Energy and Environmental Science* 5.6 (2012), pp. 7626–7636. ISSN: 17545706. DOI: [10.1039/c2ee21414h](https://doi.org/10.1039/c2ee21414h).
- [29] F. Zhu et al. "Amorphous Silicon Carbide Photoelectrode for Hydrogen Production from Water using Sunlight". In: *Solar Energy* 89 (2010), pp. 2723–2739. DOI: [10.5772/8074](https://doi.org/10.5772/8074).
- [30] National Renewable Energy Laboratory (NREL). *Calculated from data in "Reference Solar Spectral Irradiance: Air Mass 1.5"*. 2013. URL: <https://www.nrel.gov/grid/solar-resource/spectra-am1.5.html>.

- [31] Marc T. M. Koper. "Thermodynamic theory of multi-electron transfer reactions: Implications for electrocatalysis". In: *Journal of Electroanalytical Chemistry* 660.2 (2011), pp. 254–260. ISSN: 15726657. DOI: [10.1016/j.jelechem.2010.10.004](https://doi.org/10.1016/j.jelechem.2010.10.004). URL: <http://dx.doi.org/10.1016/j.jelechem.2010.10.004>.
- [32] Chairman John S. Connolly, U. S. A. and Mary. *Photochemical conversion and storage of solar energy*. Ed. by John S. Connolly. United Kin. New York: Academic Press, 1981, p. 457. ISBN: 0121858804. URL: <https://www.elsevier.com/books/photochemical-conversion-and-storage-of-solar-energy/connolly/978-0-12-185880-3>.
- [33] M. F. Weber and M. J. Dignam. "Splitting Water With Semiconducting Photoelectrodes: Efficiency Considerations." In: *Advances in Hydrogen Energy* 3.June (1984), pp. 957–968. ISSN: 02762412. DOI: [https://doi.org/10.1016/0360-3199\(86\)90183-7](https://doi.org/10.1016/0360-3199(86)90183-7).
- [34] J. R. Bolton, S. J. Strickler, and J. S. Connolly. "Limiting and realizable efficiencies of solar photolysis of water". In: *Nature* 316.6028 (1985), pp. 495–500. ISSN: 00280836. DOI: [10.1038/316495a0](https://doi.org/10.1038/316495a0).
- [35] S. Hu et al. "An analysis of the optimal band gaps of light absorbers in integrated tandem photoelectrochemical water-splitting systems". In: *Energy and Environmental Science* 6.10 (2013), pp. 2984–2993. ISSN: 17545706. DOI: [10.1039/c3ee40453f](https://doi.org/10.1039/c3ee40453f).
- [36] H. Döscher et al. "Sunlight absorption in water-efficiency and design implications for photoelectrochemical devices". In: *Energy and Environmental Science* 7.9 (2014), pp. 2951–2956. ISSN: 17545706. DOI: [10.1039/c4ee01753f](https://doi.org/10.1039/c4ee01753f).
- [37] J. Brillet et al. "Highly efficient water splitting by a dual-absorber tandem cell". In: *Nature Photonics* 6.12 (2012), pp. 824–828. ISSN: 17494885. DOI: [10.1038/nphoton.2012.265](https://doi.org/10.1038/nphoton.2012.265).
- [38] M. H. Kao et al. "Low-Temperature Growth of Hydrogenated Amorphous Silicon Carbide Solar Cell by Inductively Coupled Plasma Deposition Toward High Conversion Efficiency in Indoor Lighting". In: *Scientific Reports* 7.1 (2017), pp. 1–8. ISSN: 20452322. DOI: [10.1038/s41598-017-10661-y](https://doi.org/10.1038/s41598-017-10661-y).
- [39] Jian Hu et al. "Solar-to-hydrogen photovoltaic/photoelectrochemical devices using amorphous silicon carbide as the photoelectrode". In: *23rd European Photovoltaic Solar Energy Conference and Exhibition*. Vol. 20. September. 2008, pp. 69–72. ISBN: 4976145889250. DOI: [10.4229/23rdEUPVSEC2008-1A0.5.6](https://doi.org/10.4229/23rdEUPVSEC2008-1A0.5.6).
- [40] B. Turan et al. "Upscaling of integrated photoelectrochemical water-splitting devices to large areas". In: *Nature Communications* 7 (2016), pp. 1–9. ISSN: 20411723. DOI: [10.1038/ncomms12681](https://doi.org/10.1038/ncomms12681).
- [41] L. R. Tessler and I. Solomon. "Photoluminescence of tetrahedrally coordinated a-Si_{1-x}C_x:H". In: *Physical Review B* 52.15 (1995), pp. 10962–10971. ISSN: 01631829. DOI: [10.1103/PhysRevB.52.10962](https://doi.org/10.1103/PhysRevB.52.10962).

- [42] J. A. Kalomiros et al. "Optical properties of -SiC:H thin films grown by rf sputtering". In: *Physical Review B* 49.12 (1994), pp. 8191–8197. ISSN: 01631829. DOI: [10.1103/PhysRevB.49.8191](https://doi.org/10.1103/PhysRevB.49.8191).
- [43] D. Kuhman, S. Grammatica, and F. Jansen. "Properties of hydrogenated amorphous silicon carbide films prepared by plasma-enhanced chemical vapor deposition". In: *Thin Solid Films* 177.1-2 (1989), pp. 253–262. ISSN: 00406090. DOI: [10.1016/0040-6090\(89\)90573-7](https://doi.org/10.1016/0040-6090(89)90573-7).
- [44] J. R. McKone et al. "Evaluation of Pt, Ni, and Ni-Mo electrocatalysts for hydrogen evolution on crystalline Si electrodes". In: *Energy and Environmental Science* 4.9 (2011), pp. 3573–3583. ISSN: 17545692. DOI: [10.1039/c1ee01488a](https://doi.org/10.1039/c1ee01488a).
- [45] Emily L. Warren et al. "Hydrogen-evolution characteristics of Ni-Mo-coated, radial junction, n +p-silicon microwire array photocathodes". In: *Energy and Environmental Science* 5.11 (2012), pp. 9653–9661. ISSN: 17545692. DOI: [10.1039/c2ee23192a](https://doi.org/10.1039/c2ee23192a).
- [46] S. Uk, Y. Tae-Youl, and M. Joonhee. "N-doped Monolayer Graphene Catalyst on Silicon Photocathode for Hydrogen Production". In: *Energy Environ. Sci.* 6 (2013), pp. 3658–3664. DOI: [10.1039/b000000x](https://doi.org/10.1039/b000000x).
- [47] S. Uk et al. "Nanostructural dependence of hydrogen production in silicon photocathodes". In: *Journal of Materials Chemistry A* 1.17 (2013), pp. 5414–5422. ISSN: 20507488. DOI: [10.1039/c3ta00048f](https://doi.org/10.1039/c3ta00048f).
- [48] D. V. Esposito et al. " H_2 evolution at Si-based metal-insulator-semiconductor photoelectrodes enhanced by inversion channel charge collection and H spillover". In: *Nature Materials* 12.6 (2013), pp. 562–568. ISSN: 14761122. DOI: [10.1038/nmat3626](https://doi.org/10.1038/nmat3626).
- [49] J. A. Guerra et al. "The Urbach focus and optical properties of amorphous hydrogenated SiC thin films". In: *Journal of Physics D: Applied Physics* 49.19 (2016). ISSN: 13616463. DOI: [10.1088/0022-3727/49/19/195102](https://doi.org/10.1088/0022-3727/49/19/195102).
- [50] L. Han et al. "Gradient dopant profiling and spectral utilization of monolithic thin-film silicon photoelectrochemical tandem devices for solar water splitting". In: *Journal of Materials Chemistry A* 3.8 (2015), pp. 4155–4162. ISSN: 2050-7488. DOI: [10.1039/C4TA05523C](https://doi.org/10.1039/C4TA05523C). arXiv: [1612.08814](https://arxiv.org/abs/1612.08814).
- [51] Q. B. Ma, B. Kaiser, and W. Jaegermann. "Novel photoelectrochemical behaviors of p-SiC films on Si for solar water splitting". In: *Journal of Power Sources* 253 (2014), pp. 41–47. ISSN: 03787753. DOI: [10.1016/j.jpowsour.2013.12.042](https://doi.org/10.1016/j.jpowsour.2013.12.042).
- [52] I. A. Digdaya et al. "Extracting large photovoltages from a-SiC photocathodes with an amorphous TiO_2 front surface field layer for solar hydrogen evolution". In: *Energy Environ. Sci.* 8.5 (2015), pp. 1585–1593. ISSN: 1754-5692. DOI: [10.1039/C5EE00769K](https://doi.org/10.1039/C5EE00769K).

- [53] L. Bertoluzzi and J. Bisquert. "Equivalent circuit of electrons and holes in thin semiconductor films for photoelectrochemical water splitting applications". In: *Journal of Physical Chemistry Letters* 3.17 (2012), pp. 2517–2522. ISSN: 19487185. DOI: [10.1021/jz3010909](https://doi.org/10.1021/jz3010909).
- [54] L. Bertoluzzi et al. "Charge transfer processes at the semiconductor/electrolyte interface for solar fuel production: Insight from impedance spectroscopy". In: *Journal of Materials Chemistry A* 4.8 (2016), pp. 2873–2879. ISSN: 20507496. DOI: [10.1039/c5ta03210e](https://doi.org/10.1039/c5ta03210e).
- [55] G. D'Amico. "Si-SiC based materials obtained by infiltration of silicon: study and applications". PhD thesis. Feb. 2015, p. 224. DOI: [10.13140/RG.2.1.1617.1920](https://doi.org/10.13140/RG.2.1.1617.1920).
- [56] W. E. Spear and P. G. Le Comber. "Substitutional doping of amorphous silicon". In: *Solid State Communications* 88.11-12 (1993), pp. 1015–1018. ISSN: 00381098. DOI: [10.1016/0038-1098\(93\)90286-V](https://doi.org/10.1016/0038-1098(93)90286-V).
- [57] J. Bulloot and M. P. Schmidt. "Physics of Amorphous Silicon-Carbon Alloys". In: *Physica Status Solidi (b)* 345.143 (1987). DOI: <https://doi.org/10.1002/pssb.2221430202>.
- [58] Y. Tawada. "Introduction of the a-SiC:H/a-Si:H heterojunction solar cell and update on thin film Si:H solar modules". In: *Philosophical Magazine* 89.28-30 (2009), pp. 2677–2685. ISSN: 14786435. DOI: [10.1080/14786430902758663](https://doi.org/10.1080/14786430902758663).
- [59] A. H. Mahan et al. "Evidence for microstructure in glow discharge hydrogenated amorphous Si-C alloys". In: *Solar Cells* 21.1-4 (1987), pp. 117–126. ISSN: 03796787. DOI: [10.1016/0379-6787\(87\)90110-4](https://doi.org/10.1016/0379-6787(87)90110-4).
- [60] I. Solomon et al. "Band structure of carbonated amorphous silicon studied by optical, photoelectron, and x-ray spectroscopy". In: *Physical Review B* 38.18 (1988), pp. 13263–13270. ISSN: 01631829. DOI: [10.1103/PhysRevB.38.13263](https://doi.org/10.1103/PhysRevB.38.13263).
- [61] S. Janz et al. "Phosphorus-doped SiC as an excellent p-type Si surface passivation layer". In: *Applied Physics Letters* 88.13 (2006), pp. 2001–2003. ISSN: 00036951. DOI: [10.1063/1.2191954](https://doi.org/10.1063/1.2191954).
- [62] M. A. El Khakani et al. "Hardness and Young's Modulus of Amorphous a-SiC thin Films Determined by Nanoindentation and Bulge Tests". In: *Journal of Materials Research* 9.1 (1994), pp. 96–103. ISSN: 20445326. DOI: [10.1557/JMR.1994.0096](https://doi.org/10.1557/JMR.1994.0096).
- [63] Pasqualina M. Sarro. "Silicon carbide as a new MEMS technology". In: *Sensors and Actuators, A: Physical* 82.1 (2000), pp. 210–218. ISSN: 09244247. DOI: [10.1016/S0924-4247\(99\)00335-0](https://doi.org/10.1016/S0924-4247(99)00335-0).
- [64] P. Misaelides et al. "Surface characterisation and corrosion behaviour of SiC-coated AISI 321 stainless steel". In: *Nuclear Instruments and Methods in Physics Research B* 129.97 (1997), pp. 221–227. DOI: [https://doi.org/10.1016/S0168-583X\(97\)00214-0](https://doi.org/10.1016/S0168-583X(97)00214-0).

- [65] R. G. Munro and S. J. Dapkunas. "Corrosion characteristics of silicon carbide and silicon nitride". In: *Journal of Research - National Institute of Standards & Technology* 98.5 (1993), pp. 607–631. ISSN: 1044-677X. DOI: [10.6028/jres.098.040](https://doi.org/10.6028/jres.098.040).
- [66] L. Jiang et al. "a-SiC_x:H films deposited by plasma-enhanced chemical vapor deposition at low temperature used for moisture and corrosion resistant applications". In: *Thin Solid Films* 352.1-2 (1999), pp. 97–101. ISSN: 00406090. DOI: [10.1016/S0040-6090\(99\)00363-6](https://doi.org/10.1016/S0040-6090(99)00363-6).
- [67] *Effect of Moisture on Properties of Silicon Carbide Ceramics*. 2017 International Conference on Electronic, Control, Automation and Mechanical Engineering (ECAME 2017). ecame. 2018, pp. 310–312. ISBN: 9781605955230. DOI: [10.12783/dtetr/ecame2017/18409](https://doi.org/10.12783/dtetr/ecame2017/18409).
- [68] T. Blum et al. "Wear-resistant amorphous SiC coatings produced by plasma-enhanced CVD". In: *Surface and Coatings Technology* 116-119 (1999), pp. 1024–1028. ISSN: 02578972. DOI: [10.1016/S0257-8972\(99\)00319-9](https://doi.org/10.1016/S0257-8972(99)00319-9).
- [69] X. F. Zhang et al. "Abrasive wear behavior of heat-treated ABC-silicon carbide". In: *Journal of the American Ceramic Society* 86.8 (2003), pp. 1370–1378. ISSN: 00027820. DOI: [10.1111/j.1151-2916.2003.tb03478.x](https://doi.org/10.1111/j.1151-2916.2003.tb03478.x).
- [70] A. F. Flannery et al. "PECVD silicon carbide as a chemically resistant material for micromachined transducers". In: *Sensors and Actuators, A: Physical* 70.1-2 (1998), pp. 48–55. ISSN: 09244247. DOI: [10.1016/S0924-4247\(98\)00111-3](https://doi.org/10.1016/S0924-4247(98)00111-3).
- [71] F. A. Khan et al. "Etching of silicon carbide for device fabrication and through via-hole formation". In: *Journal of Electronic Materials* 30.3 (2001), pp. 212–219. ISSN: 03615235. DOI: [10.1007/s11664-001-0018-y](https://doi.org/10.1007/s11664-001-0018-y).
- [72] A. Auditore et al. "Human serum albumin adsorption onto a-SiC:H and a-C:H thin films deposited by plasma enhanced chemical vapor deposition". In: *Biomolecular Engineering* 19.2-6 (2002), pp. 85–90. ISSN: 13890344. DOI: [10.1016/S1389-0344\(02\)00042-4](https://doi.org/10.1016/S1389-0344(02)00042-4).
- [73] *Coating of cardiovascular stents with amorphous silicon carbide to reduce thrombogenicity*. Annual International Conference of the IEEE Engineering in Medicine and Biology - Proceedings. Vol. 16. pt 2. 1994, pp. 838–839. ISBN: 0780320506. DOI: [10.1109/iembs.1994.415171](https://doi.org/10.1109/iembs.1994.415171).
- [74] M. M. J. Treacy and K. B. Borisenko. "The local structure of amorphous silicon". In: *Science* 335.6071 (2012), pp. 950–953. ISSN: 10959203. DOI: [10.1126/science.1214780](https://doi.org/10.1126/science.1214780).
- [75] S. Janz. "Amorphous Silicon Carbide for Photovoltaic Applications". PhD thesis. Konstanz: Universität Konstanz, 2006, pp. 1–227. URL: <http://nbn-resolving.de/urn:nbn:de:bsz:352-opus-32019>.

- [76] V. I. Ivashchenko et al. "Tight-binding-molecular-dynamics investigation of the atomic and electronic structure properties of a-C, a-Si and a-SiC". In: *Diamond and Related Materials* 12.3-7 (2003), pp. 993–997. ISSN: 09259635. DOI: [10.1016/S0925-9635\(02\)00271-6](https://doi.org/10.1016/S0925-9635(02)00271-6).
- [77] C. E. Nebel et al. "Structure and properties of high-temperature annealed CVD diamond". In: *Diamond and Related Materials* 12 (2003), pp. 1873–1876. ISSN: 09259635. DOI: [10.1016/S0925-9635](https://doi.org/10.1016/S0925-9635). URL: <http://www.sciencedirect.com/science/article/pii/S0925963503001924>.
- [78] W. M. Sears and M. A. Gee. "Mechanics of film formation during the spray pyrolysis of tin oxide". In: *Thin Solid Films* 165.1 (1988), pp. 265–277. ISSN: 00406090. DOI: [10.1016/0040-6090\(88\)90698-0](https://doi.org/10.1016/0040-6090(88)90698-0).
- [79] Y. Inoue et al. "Raman spectra of amorphous SiC". In: *Solid State Communications* 48.12 (1983), pp. 1071–1075. ISSN: 00381098. DOI: [10.1016/0038-1098\(83\)90834-7](https://doi.org/10.1016/0038-1098(83)90834-7).
- [80] A. Yamada et al. "Wide band-gap, fairly conductive p-type hydrogenated amorphous silicon carbide films prepared by direct photolysis; Solar cell application". In: *Applied Physics Letters* 46.3 (1985), pp. 272–274. ISSN: 00036951. DOI: [10.1063/1.95655](https://doi.org/10.1063/1.95655).
- [81] T. Kunz et al. "Silicon carbide barrier layer on ceramic substrates for crystalline silicon thin-film modules with an integrated series connection". In: *3rd World Conference on Photovoltaic Energy Conversion, 2003. Proceedings of*. Vol. 2. 2003, pp. 1255–1258. DOI: [10.1109/WCPEC.2003.1306146](https://doi.org/10.1109/WCPEC.2003.1306146).
- [82] Michael A. Lieberman and Allan J. Lichtenberg. *Principles of Plasma Discharges and Materials Processing: Second Edition*. Ed. by Inc Publication A John Wiley & Sons. Second. New Jersey: Wiley Interscience, 2005, pp. 1–757. ISBN: 0471720011. DOI: [10.1002/0471724254](https://doi.org/10.1002/0471724254).
- [83] T. Tsuyuki et al. "Preparation of very stable and low hydrogen content amorphous silicon films by hydrogen-radical CVD method". In: *Solar Energy Materials and Solar Cells* 49.1-4 (1997), pp. 95–100. ISSN: 09270248. DOI: [10.1016/S0927-0248\(97\)00181-5](https://doi.org/10.1016/S0927-0248(97)00181-5).
- [84] Zhebo Chen, Huyen N. Dinh, and Eric Miller. *Photoelectrochemical Water Splitting*. 2013, p. 130. ISBN: 978-1-4614-8297-0. DOI: [10.1007/978-1-4614-8298-7](https://doi.org/10.1007/978-1-4614-8298-7).
- [85] J. Tauc. "Optical properties and electronic structure of amorphous Ge and Si". In: *Materials Research Bulletin* 3 (1968), pp. 37–46. ISSN: 10003290. DOI: [10.7498/aps.58.1166](https://doi.org/10.7498/aps.58.1166).
- [86] F. Urbach. "The long-wavelength edge of photographic sensitivity and of the electronic Absorption of Solids [8]". In: *Physical Review* 92.5 (1953), p. 1324. ISSN: 0031899X. DOI: [10.1103/PhysRev.92.1324](https://doi.org/10.1103/PhysRev.92.1324).

- [87] A. R. Zanatta. "Revisiting the optical bandgap of semiconductors and the proposal of a unified methodology to its determination". In: *Scientific reports* 9.1 (2019), p. 11225. ISSN: 20452322. DOI: [10.1038/s41598-019-47670-y](https://doi.org/10.1038/s41598-019-47670-y). URL: <http://dx.doi.org/10.1038/s41598-019-47670-y>.
- [88] K. O'Leary Stepehn and S. Zukotynski. "Optical absorption in amorphous semiconductors". In: *Physical Review B* 52.11 (1995), pp. 7795–7797. ISSN: 00157120. DOI: <https://doi.org/10.1103/PhysRevB.52.7795>. eprint: [arXiv:1011.1669v3](https://arxiv.org/abs/1011.1669v3).
- [89] J. A. Guerra et al. "Band-fluctuations model for the fundamental absorption of crystalline and amorphous semiconductors: A dimensionless joint density of states analysis". In: *Journal of Physics D: Applied Physics* 52.10 (2019). ISSN: 13616463. DOI: [10.1088/1361-6463/aaf963](https://doi.org/10.1088/1361-6463/aaf963).
- [90] A. Tejada et al. "Determination of the fundamental absorption and optical bandgap of dielectric thin films from single optical transmittance measurements". In: *Applied Optics* 58 (Dec. 2019), p. 9585. DOI: [10.1364/AO.58.009585](https://doi.org/10.1364/AO.58.009585).
- [91] R. Arce et al. "Direct evidence of porosity in carbon-rich hydrogenated amorphous silicon carbide films". In: *Journal of Applied Physics* 66.9 (1989), pp. 4544–4546. ISSN: 00218979. DOI: [10.1063/1.343926](https://doi.org/10.1063/1.343926).
- [92] E. Lotter and G. H. Bauer. "The vibrational spectrum of a-SiC:H films in the 500 cm⁻¹ to 9000cm⁻¹ range by FTIR transmission and photothermal deflection spectroscopy". In: *Materials Research Society Symposium Proceedings* 258.27 (1992), pp. 517–522. DOI: [10.1557/PROC-258-517](https://doi.org/10.1557/PROC-258-517).
- [93] S. Gallis et al. "Comparative study of the effects of thermal treatment on the optical properties of hydrogenated amorphous silicon-oxycarbide". In: *Journal of Applied Physics* 102.2 (2007). ISSN: 00218979. DOI: [10.1063/1.2753572](https://doi.org/10.1063/1.2753572).
- [94] P. Salvador and C. Gutierrez. "On the nature of surface states involved in the photo- and electroluminescence spectra of n-TiO₂ electrodes". In: *Journal of Physical Chemistry* 88.16 (1984), pp. 3696–3698. ISSN: 00223654. DOI: [10.1021/j150660a064](https://doi.org/10.1021/j150660a064).
- [95] P. Salvador. "Mechanisms of Charge Transfer at the Semiconductor-Electrolyte Interface". In: *Journal of The Electrochemical Society* 131.2 (1984), p. 326. ISSN: 00134651. DOI: [10.1149/1.2115569](https://doi.org/10.1149/1.2115569).
- [96] Juan Bisquert. *Nanostructured energy devices : equilibrium concepts and kinetics*. 2015, p. 352. ISBN: 1439836027. URL: https://books.google.com/books?id=5YvaBAAAQBAJ&lr=&source=gbs_navlinks_s.
- [97] T. Friessnegg et al. "Effect of annealing on the defect structure in a-SiC:H films". In: *Journal of Applied Physics* 80.4 (1996), pp. 2216–2223. ISSN: 00218979. DOI: [10.1063/1.363049](https://doi.org/10.1063/1.363049).

- [98] R. R. Koropecski, F. Alvarez, and R. Arce. "Erratum: "Infrared study of the Si - H stretching band in a-SiC:H" (Journal of Applied Physics (1991) 69 (7805))". In: *Journal of Applied Physics* 71.1 (1992), p. 545. ISSN: 00218979. DOI: [10.1063/1.351409](https://doi.org/10.1063/1.351409).
- [99] A. V. Vasin et al. "Comparative study of annealing and oxidation effects in a-SiC:H and a-SiC thin films deposited by radio-frequency magnetron sputtering". In: *Thin Solid Films* 519.7 (2011), pp. 2218–2224. ISSN: 00406090. DOI: [10.1016/j.tsf.2010.11.005](https://doi.org/10.1016/j.tsf.2010.11.005). URL: <http://dx.doi.org/10.1016/j.tsf.2010.11.005>.
- [100] J. Han. "Structural and Electrical Characterisations of Amorphous Silicon Carbide Films". 2000, p. 277. URL: <https://scholarbank.nus.edu.sg/handle/10635/14329>.
- [101] M. Ishimaru et al. "Direct observations of thermally induced structural changes in amorphous silicon carbide". In: *Journal of Applied Physics* 104.3 (2008). ISSN: 00218979. DOI: [10.1063/1.2960342](https://doi.org/10.1063/1.2960342).
- [102] MdC. Mejia et al. "Analysis of the physical and photoelectrochemical properties of c-Si(p)/a-SiC:H(p) photocathodes for solar water splitting". In: *Journal of Physics D: Applied Physics* (2021). URL: <http://iopscience.iop.org/article/10.1088/1361-6463/abdb69>.
- [103] Q. B. Ma et al. "XPS characterization and photoelectrochemical behaviour of p-type 3C-SiC films on p-Si substrates for solar water splitting". In: *Journal of Physics D: Applied Physics* 45.32 (2012). ISSN: 00223727. DOI: [10.1088/0022-3727/45/32/325101](https://doi.org/10.1088/0022-3727/45/32/325101).
- [104] G. Vincent, A. Chantre, and D. Bois. "Electric field effect on the thermal emission of traps in semiconductor junctions". In: *Journal of Applied Physics* 50.8 (1979), pp. 5484–5487. ISSN: 00218979. DOI: [10.1063/1.326601](https://doi.org/10.1063/1.326601).
- [105] S.M. Sze and Kwok K. Ng. *Physics of semiconductor devices*. California, pp. i–x. ISBN: 1-4020-7018-7. DOI: [10.1002/9780470068328.fmatter](https://doi.org/10.1002/9780470068328.fmatter).
- [106] K. Sekizawa, K. Oh-Ishi, and T. Morikawa. "Photoelectrochemical water-splitting over a surface modified p-type Cr₂O₃ photocathode". In: *Dalton Transactions* 49.3 (2020), pp. 659–666. ISSN: 14779234. DOI: [10.1039/c9dt04296b](https://doi.org/10.1039/c9dt04296b).
- [107] M. Kitano et al. "Hydrolysis of Cellulose by Amorphous Carbon Bearing SO₃H, COOH, and OH Groups". In: *Journal of the American Chemical Society* 130 (2008), pp. 12787–12793. ISSN: 07437463. DOI: [10.1021/la8040506](https://doi.org/10.1021/la8040506).
- [108] B. E. Conway, L. Bai, and M. A. Sattar. "Role of the transfer coefficient in electrocatalysis: Applications to the H₂ and O₂ evolution reactions and the characterization of participating adsorbed intermediates". In: *International Journal of Hydrogen Energy* 12.9 (1987), pp. 607–621. ISSN: 03603199. DOI: [10.1016/0360-3199\(87\)90002-4](https://doi.org/10.1016/0360-3199(87)90002-4).

- [109] Y. Tachibana et al. "Subpicosecond interfacial charge separation in dye-sensitized nanocrystalline titanium dioxide films". In: *Journal of Physical Chemistry* 100.51 (1996), pp. 20056–20062. ISSN: 00223654. DOI: [10.1021/jp962227f](https://doi.org/10.1021/jp962227f).
- [110] P. A. Nikolaychuk. "The Revised Pourbaix Diagram for Silicon". In: *Silicon* 6.2 (2014), pp. 109–116. ISSN: 18769918. DOI: [10.1007/s12633-013-9172-0](https://doi.org/10.1007/s12633-013-9172-0).
- [111] C. F. O. Graeff, R. Buhleier, and M. Stutzmann. "Light-induced annealing of metastable defects in hydrogenated amorphous silicon". In: *Applied Physics Letters* 62.23 (1993), pp. 3001–3003. ISSN: 00036951. DOI: [10.1063/1.109170](https://doi.org/10.1063/1.109170).
- [112] B. Pivac et al. "UV light induced defects in amorphous silicon thin films". In: *User Modeling and User-Adapted Interaction* 71.1-2 SPEC. (2003), pp. 135–139. ISSN: 0042207X. DOI: [10.1016/S0042-207X\(02\)00727-3](https://doi.org/10.1016/S0042-207X(02)00727-3).
- [113] O. X. Esebamen. "Effect of UV radiation surface damage on silicon position sensitive photodetector". In: *Optik* 127.2 (2016), pp. 599–602. ISSN: 00304026. DOI: [10.1016/j.ijleo.2015.09.074](https://doi.org/10.1016/j.ijleo.2015.09.074). URL: <http://dx.doi.org/10.1016/j.ijleo.2015.09.074>.
- [114] A. M. Cowley and S. M. Sze. "Surface states and barrier height of metal-semiconductor systems". In: *Journal of Applied Physics* 36.10 (1965), pp. 3212–3220. ISSN: 00218979. DOI: [10.1063/1.1702952](https://doi.org/10.1063/1.1702952).
- [115] N. C. Deb Nath et al. "Electrochemical approach to enhance the open-circuit voltage (Voc) of dye-sensitized solar cells (DSSCs)". In: *Electrochimica Acta* 109 (2013), pp. 39–45. ISSN: 0013-4686. DOI: <https://doi.org/10.1016/j.electacta.2013.07.057>.
- [116] K. Yoshinaga et al. "Fabrication of silicon and carbon based wide-gap semiconductor thin films for high conversion efficiency". In: *Journal of Physics: Conference Series* 441.1 (2013). ISSN: 17426596. DOI: [10.1088/1742-6596/441/1/012040](https://doi.org/10.1088/1742-6596/441/1/012040).
- [117] M. Perný et al. "AC impedance spectroscopy of Al/a-SiC/c-Si(p)/Al heterostructure under illumination". In: *Journal of Electrical Engineering* 65.3 (2014), pp. 174–178. ISSN: 13353632. DOI: [10.2478/jee-2014-0027](https://doi.org/10.2478/jee-2014-0027).
- [118] Hans Lüth. *Solid Surfaces, Interfaces and Thin Films*. 2010. ISBN: 978-3-642-13591-0. DOI: [10.1007/978-3-642-13592-7](https://doi.org/10.1007/978-3-642-13592-7).
- [119] MdC. Mejia et al. "Localized surface states influence in the photoelectrocatalytic performance of Al doped a-SiC:H based photocathodes". In: *Materials Science in Semiconductor Processing* 143 (2022), p. 106474. ISSN: 1369-8001. DOI: <https://doi.org/10.1016/j.mssp.2022.106474>. URL: <https://www.sciencedirect.com/science/article/pii/S1369800122000257>.
- [120] T. L. Biggerstaff et al. "Relationship between 4H-SiC/SiO₂ transition layer thickness and mobility". In: *Applied Physics Letters* 95.3 (2009), pp. 23–26. ISSN: 00036951. DOI: [10.1063/1.3144272](https://doi.org/10.1063/1.3144272).